Laser Assisted Mechanical Micromachining of Hard-to-Machine Materials

A Thesis
Presented to
The Academic Faculty

by

Ramesh K. Singh

In Partial Fulfillment
of the Requirements for the Degree
Doctor of Philosophy

George W. Woodruff School of Mechanical Engineering
Georgia Institute of Technology
December 2007

Laser Assisted Mechanical Micromachining of Hard-to-Machine Materials

Approved by:

Professor Shreyes N. Melkote (ME, Georgia Tech), Committee Chair

Professor Steven Liang (ME/MSE, Georgia Tech)

Professor Samuel Graham (ME, Georgia Tech)

Professor Roshan Vengazhiyil (ISyE, Georgia Tech)

Professor Steven W. Johnson (MSE, Georgia Tech)

Date Approved: 09 November 2007

ACKNOWLEDGEMENTS

A PhD thesis can never be completed by the student alone. Acknowledging the support and cooperation of the people who have helped me in many ways is the least I can do to thank them.

Thanks to Prof. Anil Saigal, Prof. Greif of Tufts University, for providing me references for graduate school applications and Dr. Bill Wepfer for helping me through the admission process. My advisor, Prof. Shreyes N. Melkote, for his mentorship and financial support during the course of my study here at Georgia Tech. Special thanks for being available for guidance and discussions whenever I needed him. My committee members, Prof. Vengazhiyil, Prof. Graham, Prof. Johnson and Prof. Liang for overlooking my thesis work. Thanks to Dr. Hashimoto of the Timken Company and National Science Foundation grants (DMI-0300457 and CMMI-0654369) for funding my research study. Mr. Steven Sheffield, for training me on the machines and assisting me to build my experimental setup and always coming up with solutions for any practical glitch. Mr. John Graham, for running a great machine shop without which I would have struggled. Prof. Vengazhiyil for exposing me to the beautiful world of Statistics and helping with optimization. Cosetta Williams, Trudy Allen, and Glenda Johnson at the ME office, and, Siri Melkote, Pam Rountree and Wanda Joefield, in the MaRC building, for several administrative assistances without which my Ph.D. ride would have been challenging. Thanks to Georgia Tech for providing the opportunity for teaching ME 4210.

My group colleagues, Kai Liu, Sangil Han, Sathyan Subbiah, Chee Keong Ng, Haiyan Deng, Xavier Brun, Rick Kalil, Anand Raghu, Jeff Smith, Supat Ieamsupapong, Mike Lazarakis, Vincent Dessoly, Tommy Newton, Chris Golden, Matt Breland,

Siva Venkatachalam, Hyung-wook Park, Qiulin and Adam Cardy for their general assistance and making a grad student's work life more easier to swallow. Special thanks to Mukund Kumar for providing assistance with my thesis work and being a good running buddy. Special thanks to my PhD qualifier study group - Srinidhi, Sashi, Quan-Ming Li, Chris Green, Kwako Eason and Laine Myers - for the valuable discussions. Thanks to Satish for bearing with me for two years. The time I spent with Srinidhi Nagaraja was the most wonderful time of my life and he was there for dinner every evening encouraging me in my cullinary adventures and patiently listening my post dinner spiritual discourses.

Thanks to Sathyan, for providing me the LaTeX thesis template and Sriram for painfully debugging my LaTeX code and teaching me some tricks of the trade. My sincere thanks to Krishna Tunga who helped me immensely with thermal modeling and has provided me his insight on a wide range of topics from science to spirituality and Goutham for being a good friend and an excellent cook. Thanks to Amin for all his help and support over last few months and Dinesh Bansal for his eye-opening technical arguments in our debates. Special mention of Yash, Ayona and Mamtaben for their kindness and potlucks.

Special thanks to my friend Anuj who helped me initially settle down in the Atlanta area. Thanks to many other friends such as Ashok, Amar, Lavanya, Udai, Sailaja, Anup, Pat, Loveen, Sriram, Rahul, Shivane, Mamta, Pritty, Ruta, Amrish, Anil, Nandita, Kartik B., Smitha, Kartik S., Murali, Vrishali and many others whose association made life in Atlanta much more fun.

And finally, I am indebted to my family - father J. N. Singh, mother Savirti Devi, sister Ashwini, brother Satyendra, brother-in-law Om Prakash , baby niece Jenna, my Uncle Ramji, Aunty Sharmila and Aunty Ishani. Thanks also to my cousins Tushar and Tanay.

TABLE OF CONTENTS

LIST OF TABLES

LIST OF FIGURES

SUMMARY

There is growing demand for micro and meso scale devices with applications in the field of optics, semiconductor and bio-medical fields. In response to this demand, mechanical micro-cutting (e.g. micro-milling) is emerging as a viable alternative to lithography based micromachining techniques. Mechanical micromachining methods are capable of generating three-dimensional free-form surfaces to sub-micron level precision and micron level accuracies in a wide range of materials including common engineering alloys. However, certain factors limit the types of workpiece materials that can be processed using mechanical micromachining methods. For difficult-to-machine materials such as tool and die steels, limited machine-tool system stiffness and low tool flexural strength are major impediments to the use of mechanical micromachining methods.

This thesis presents the design, fabrication and analysis of a novel *Laser-assisted Mechanical Micromachining* (LAMM) process that has the potential to overcome these limitations. The basic concept involves creating localized thermal softening of the hard material by focusing a solid-state continuous wave laser beam of diameter ranging from 70-120 μm directly in front of a miniature (300 μm-1 mm wide) cutting tool. By suitably controlling the laser power, spot size and speed, it is possible to produce a sufficiently large decrease in flow stress of the work material and, consequently, the cutting forces. This in turn will reduce machine/tool deflection and chances of catastrophic tool failure. The reduced machine/tool deflection yields improved accuracy in the machined feature. In order to use this process effectively, adequate thermal softening needs to be produced while keeping the heat affected zone in the machined surface to a minimum. This requires experimental characterization and

process modeling, which has been accomplished in thesis via the following tasks:

- Design and fabrication of a laser assisted mechanical micromachining (LAMM) setup with a 35 W fiber laser
- Experimental characterization of the LAMM process for cutting forces, surface integrity (hardness, microstructure, surface finish) and dimensional accuracy as a function of cutting parameters and/or laser variables
- Modeling the process mechanics (temperatures and forces)
- Optimization of the process variables using engineering-statistical models

This study provides the underlying scientific and empirical basis needed for future development of production-grade laser-assisted mechanical micro machine tools for milling/turning etc. Potential applications of these machine tools include manufacture of micro and meso scale features in molds and dies for plastic injection molding of meso-scale biomedical parts as well as creation of three dimensional micro geometric patterns on metal and ceramic bearing surfaces.

CHAPTER I

INTRODUCTION

1.1 The Machining Process

Machining is a versatile material removal process to obtain complex geometries and desired surface finish in a wide range of materials. The material is removed from the workpiece in the form of chips through direct mechanical contact with a cutting tool. Since the material removal takes place only in the form of small chips, in order to machine a desired area the material is constantly fed at a suitable rate. There are a number of machining processes that are used to generate desired features. The common machining processes such as turning and milling are fairly complex oblique cutting processes where the cutting edge of the tool is oblique (non-orthogonal) to the direction of the cutting velocity. This causes the chips to flow side-ways, often results in non-uniform uncut chip thickness, and yields a three dimensional cutting force system. Although some of the machining processes can be very complex, a simplified machining operation can be represented by Fig. 1.1. This schematic presents an orthogonal model that can be adequately represented by a two-dimensional geometry. Cutting edge of the tool is perpendicular to cutting direction. Consequently, the chip does not flow to the side and all the work and chip material particles move in the plane of paper. Any component of velocity or motion in the lateral direction is absent. Fig. 1.1 shows the cutting tool, workpiece, chip and the shear zone. The material removal is assumed to be the outcome of shear in the shear zone which results in the formation of the chip.

Traditionally, the feature sizes produced in machining were well above the millimeter range but due to recent push towards miniaturization, the feature size is shrinking

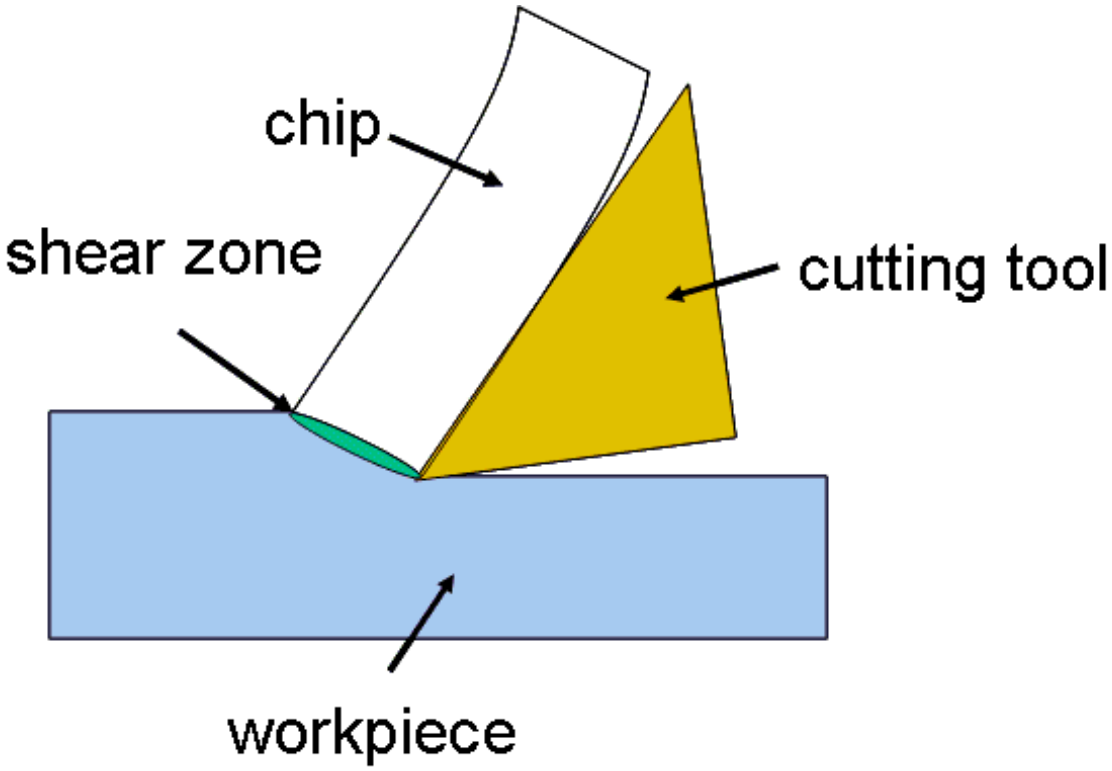

Figure 1.1: Orthogonal cutting

down to meso/micro scales, which presents new challenges. These issues are discussed in the following sections.

1.2 Machining at the Microscale

The machining process can be broadly classified as macro- and micro-cutting based on the interference between the tool and workpiece, i.e., the uncut chip thickness. If the uncut chip thickness is large ($> 200\mu$m), then it is commonly regarded as macro-cutting and if the uncut chip thickness is small (< 200 μm), it is called micro-cutting. Masuzawa et al. [1] have defined the range of uncut chip thickness for micro-cutting as 0.1 to 200 μm. Larger interference values are normally used in "rough" machining operations to increase the material removal rate under mass-production environments. Smaller interference values are normally used in finishing operations after roughing operations have removed most of the unwanted material from the bulk workpiece. The need for miniaturized products with three-dimensional micro ($1 \sim$ few hundred μm) and/or meso ($1 \sim$ few millimeters) scale features continues to grow rapidly. Much of this need is driven today by developments in the medical device, optical, and semiconductor fields. Fig. 1.2 and Fig. 1.3 show typical examples of micro/meso scale parts [2, 3]. Fig. 1.4 shows a mechanical micro-milling machine developed in the Precision Machining Laboratory at Georgia Tech.

In particular, there is a growing demand for miniaturized mechanical components and surgical tools used in modern diagnostic and therapeutic procedures. Since cleaning and sterilization of miniaturized devices is difficult, they must be disposable and inexpensive. Examples of such devices include fluidic actuators and steering oscillators that find application in cutting and filing interventions during surgery, micro-turbines for milling and drilling interventions such as in the removal of arterial plaque, micro-pumps for dosing of drugs and microstructures for support of 3-D tissue culture growth [4]. The current method used for manufacture of these components

Figure 1.2: Microgear for MEMS application [2]

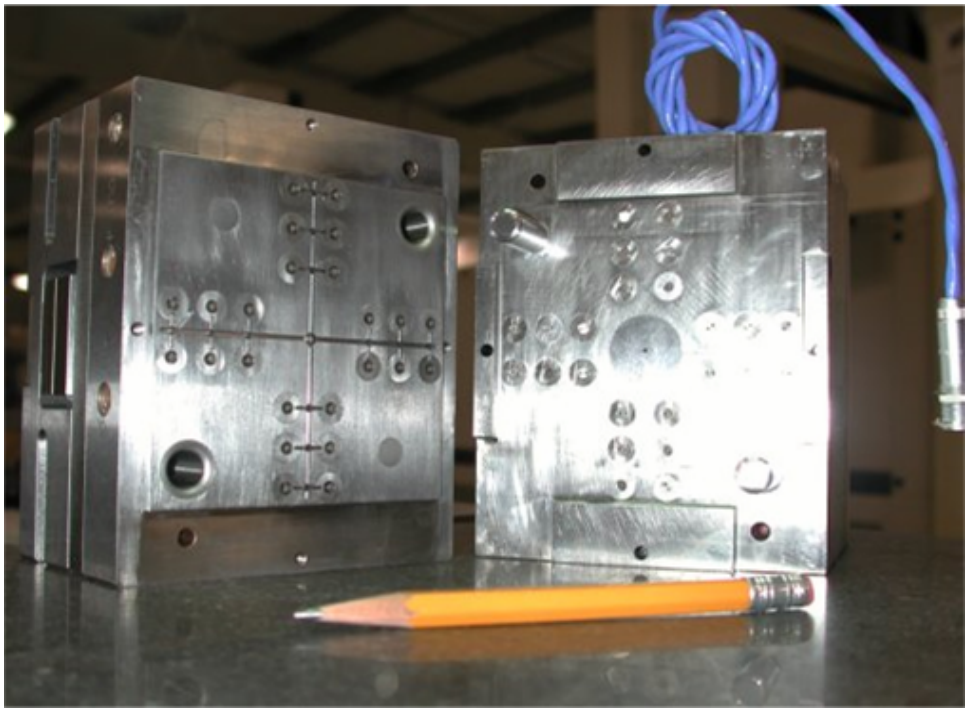

Figure 1.3: Micromold for injection molding [3]

Figure 1.4: Micromilling machine

often involves the combined processes of Lithography, Electroforming and Molding or LIGA (LIthographie Galvanoformung Abformung), which can produce high aspect ratio silicon, metallic (copper, Ni alloys and Fe-Ni alloys) and polymeric shapes. In contrast, mechanical micromachining processes such as micro-milling or micro-turning have several advantages over LIGA-type processes. Unlike most silicon-based micro machining processes (including lithography, laser ablation and chemical etching), mechanical micro-cutting methods can process a wide variety of materials including metals, ceramics and polymers. They can also produce complex three-dimensional

free-form shapes that are difficult to create using lithography-based methods, which are limited to relatively simple shapes. Mechanical micromachining can be less expensive than other methods because no specialized equipment/environment such as a clean room or X-ray synchrotron is typically required. In addition, recent developments in mechanical micromachining have shown that nanometer precision and submicron accuracies can be achieved [1]. As a result, mechanical micro machining is gaining importance for its ability to produce parts with three-dimensional features ranging in size from a few microns to a few hundred microns in a wide range of materials.

1.3 Limitations of Micromachining

Despite the potential advantages, practical use of mechanical micromachining is limited by the workpiece and tool material properties. In particular, very low machine-tool system stiffness and inadequate tool strength limit the utility of mechanical micromachining, especially for hard-to-machine materials such as hardened steels, titanium alloys and ceramics. Although diamond tools can be used for ceramics, they cannot be used for hardened steels and titanium alloys due to rapid wear of the diamond tool when machining these materials [5]. At micro/meso length scales of cutting, the effect of tool and machine (e.g. motion stage) deflections arising from the increased cutting forces on the dimensional accuracy can be significant. Also, mechanical micromachining is a slow process when cutting hard materials. One approach to address these drawbacks is to employ the thermal softening ability of a laser source to heat the material during micro-cutting and thereby lower the forces and tool/workpiece deflections.

1.4 Research Approach and Outline

In light of the aforementioned limitations, this research is focused on the development, modeling and optimization of a hybrid Laser-Assisted Mechanical Micromachining (LAMM) process that combines the thermal softening ability of a laser source with the three-dimensional feature generation capability of mechanical micro-cutting processes such as micro-grooving. The approach involves using a relatively low-power (2∼35W) continuous solid state fiber laser in conjunction with a mechanical micro-grooving process. The laser beam (70-120 μm diameter with suitable optics) is focused at a fixed distance in front of a miniature cutting tool (i.e. grooving tool of 300-1000 μm cutting width) to soften the workpiece material ahead of the tool thereby lowering the forces and machine/tool deflections produced in the operation. The decrease in cutting force due to thermal softening of the work material can be designed to overcome the limitations of machine-tool system stiffness, tool flexural strength and catastrophic tool failure usually encountered in micro and meso scale machining of hard materials. In addition, with proper design, the LAMM process can also process ceramics such as zirconia. Although notable work on pure laser micromachining using ultra-short pulsing lasers (e.g. nanosecond/picosecond/femtosecond lasers) [6, 7] and work on laser-assisted mechanical machining of ceramics at the macro-scale has been reported [8, 9], there has been little or no work reported on laser assisted mechanical machining at the micron scale [10, 11]. Scaling down the process introduces significant technical challenges in terms of process design because the heat dissipation volume is small and the laser fluence is high when compared to macroscale laser assisted machining. Consequently, considerable care needs to be exercised in order to minimize thermal damage in the heat affected zone (HAZ). Also, unlike its macroscale counterpart, the uncut chip thickness in LAMM can be of the same order of magnitude as the tool edge radius (1 $\sim$ few tens of microns). In addition, at these length scales

of cutting, the role of elastic deformations of the tool, workpiece and precision motion stages on the resulting forces and dimensional accuracy can be significant. For these reasons, developing a fundamental understanding of the aforementioned effects and scientific solutions for the resulting problems is crucial. In particular, controlling and/or minimizing the thermal damage in the heat affected zone and dimensional errors are significant technical challenges associated with the LAMM process. Therefore, the primary objectives of this thesis are:

1. Design and fabrication of a hybrid laser assisted mechanical micromachining (LAMM) test bed for micro/meso scale grooving of difficult-to-machine materials.

2. Experimental characterization of the LAMM process for cutting forces, temperature distribution, surface integrity (hardness, microstructure, surface finish) and dimensional accuracy as a function of cutting parameters and laser variables.

3. Modeling the process mechanics (temperatures and forces)

4. Optimization of the process variables using engineering-statistical models to create a desired feature size without a residual HAZ in the machined surface.

These goals have been achieved through carefully planned experiments, modeling and optimization efforts described in subsequent chapters of the thesis. Fig. 1.5 shows the overall research plan with each block representing a task.

Chapter 3 deals with design, fabrication and preliminary experiments with AISI 1018 steel. Chapter 4 presents a detailed experimental characterization of the LAMM process, micro scale grooving experiments are conducted on H-13 mold steel (42 HRC) in order to understand the influence of laser variables and cutting parameters on the cutting forces, groove depth and surface finish. Chapter 5 is focused on characterization and prediction of the HAZ produced in a LAMM based micro-grooving process.

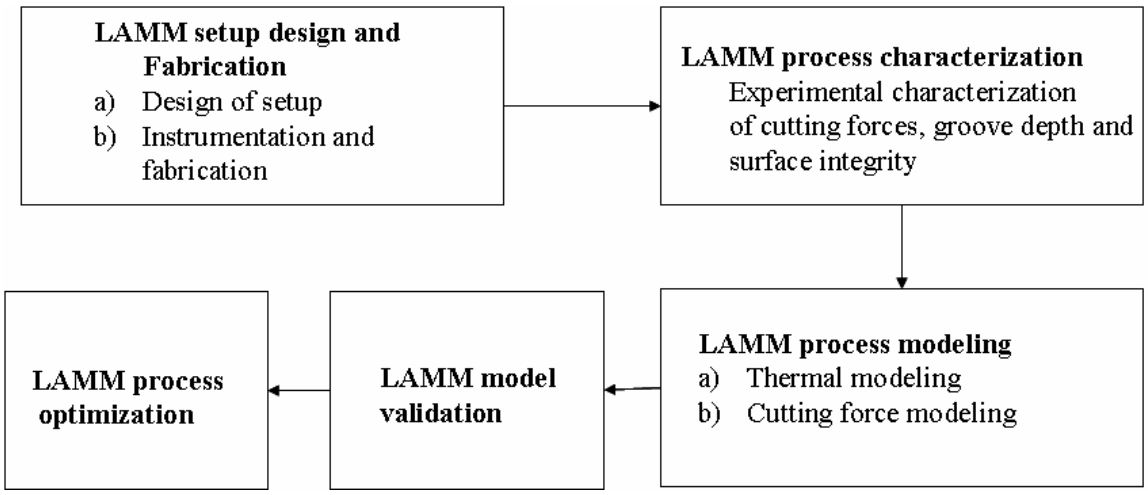

Figure 1.5: Overall research plan

The heat affected zone caused by pure laser heating of H-13 mold steel (42 HRC) at different laser scanning speeds is examined for changes in microstructure and micro-hardness and a 3-D transient finite element thermal model for laser heating is developed to verify the observations. Chapter 6 describes a cutting force model for the laser-assisted micro grooving process. This model combines a slip-line field based force model with a finite element based thermal model, developed in the previous chapter, and a constitutive model for the material flow stress to predict the cutting forces. In addition to including thermal softening due to laser heating, the model also accounts for the tool edge radius and elastic deflection of the tool-machine system. Chapter 7 presents an optimization technique based on minimizing the engineering-statistical force model subject to temperature constraints to avoid residual heat affected zone for a desired feature size. The main conclusions of this thesis are drawn in Chapter 8 and suggestions for future work are given.

CHAPTER II

LITERATURE REVIEW

Lasers have long been used for cutting, welding and surface treatment of materials at the macro scale [12, 13]. Pure laser machining at the macro scale has been studied extensively. Laser machines have been developed for 1-D operation such as drilling (shown in Fig. 2.1) and plate cutting shown in Fig. 2.2, which is a 2-D operation. A machine consisting of two laser beams inclined at different angles can imitate 3-D mechanical machining operations such as turning and milling (3-D machining) as shown in Fig. 2.3 [14, 15, 16].

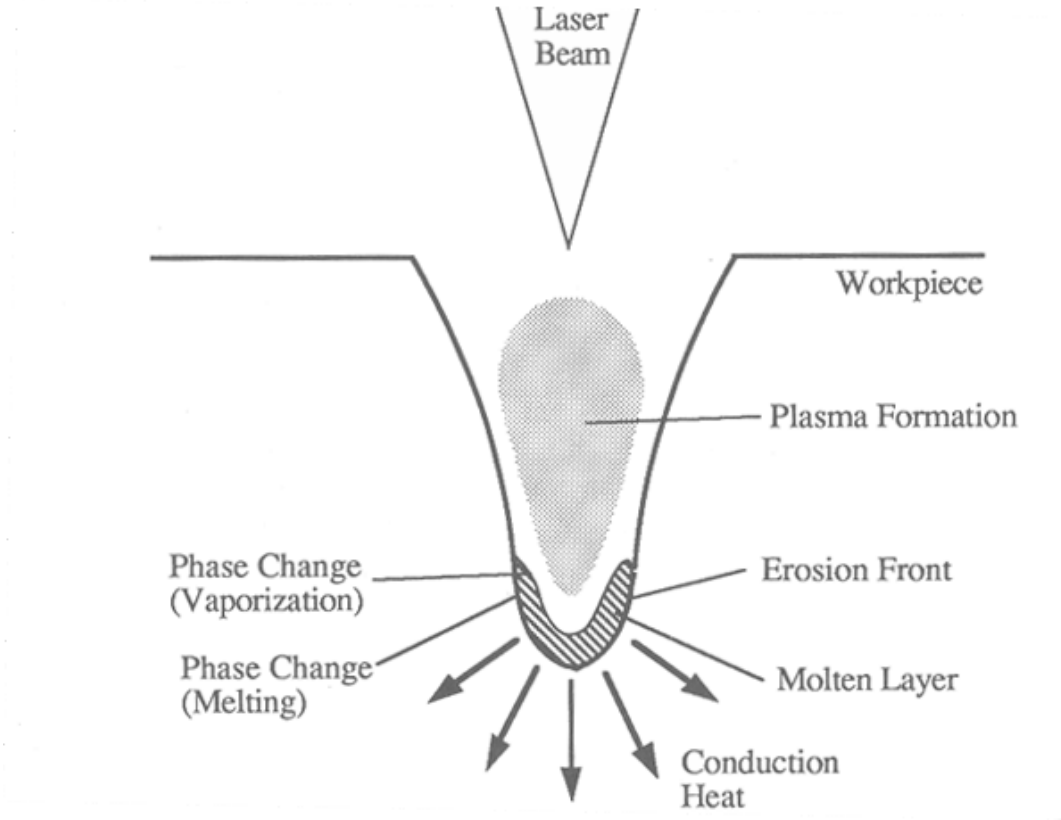

Figure 2.1: Laser drilling [13]

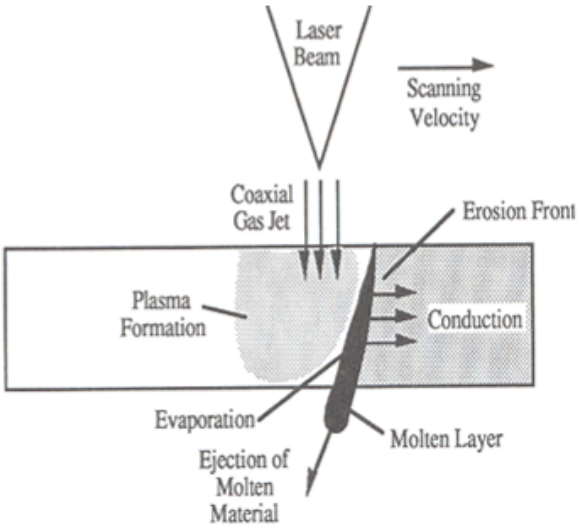

Figure 2.2: Laser plate cutting [13]

Laser cutting, drilling, grooving and 3-D machining processes have been analyzed and modeled [17, 18, 19, 20, 21, 22, 23, 24, 25, 26, 27, 28]. More recently, lasers have also been used for micro scale shot peening of thin films. Zhang et al. [29] modeled the laser shock peening of thin film copper on a silicon substrate. Cheng et al. [30] analyzed laser-based sheet metal forming process for thin plates. Laser ablation techniques for micromachining have also evolved, especially for quartz and glass [31, 32, 33, 34]. Other than techniques mentioned before that use only lasers for material processing, laser assisted machining for ceramics at the macroscale have also been developed and studied. With the exception of very recent work, hybrid processes, such as laser assisted mechanical micromachining, have not been studied and modeled in detail. This section reviews prior work in the relevant areas of hybrid laser assisted mechanical machining at the macro scale, pure laser micromachining using continuous wave (CW)/ultra-short pulse lasers, pure mechanical micromachining, thermal modeling of a moving heat source and laser assisted mechanical micromachining.

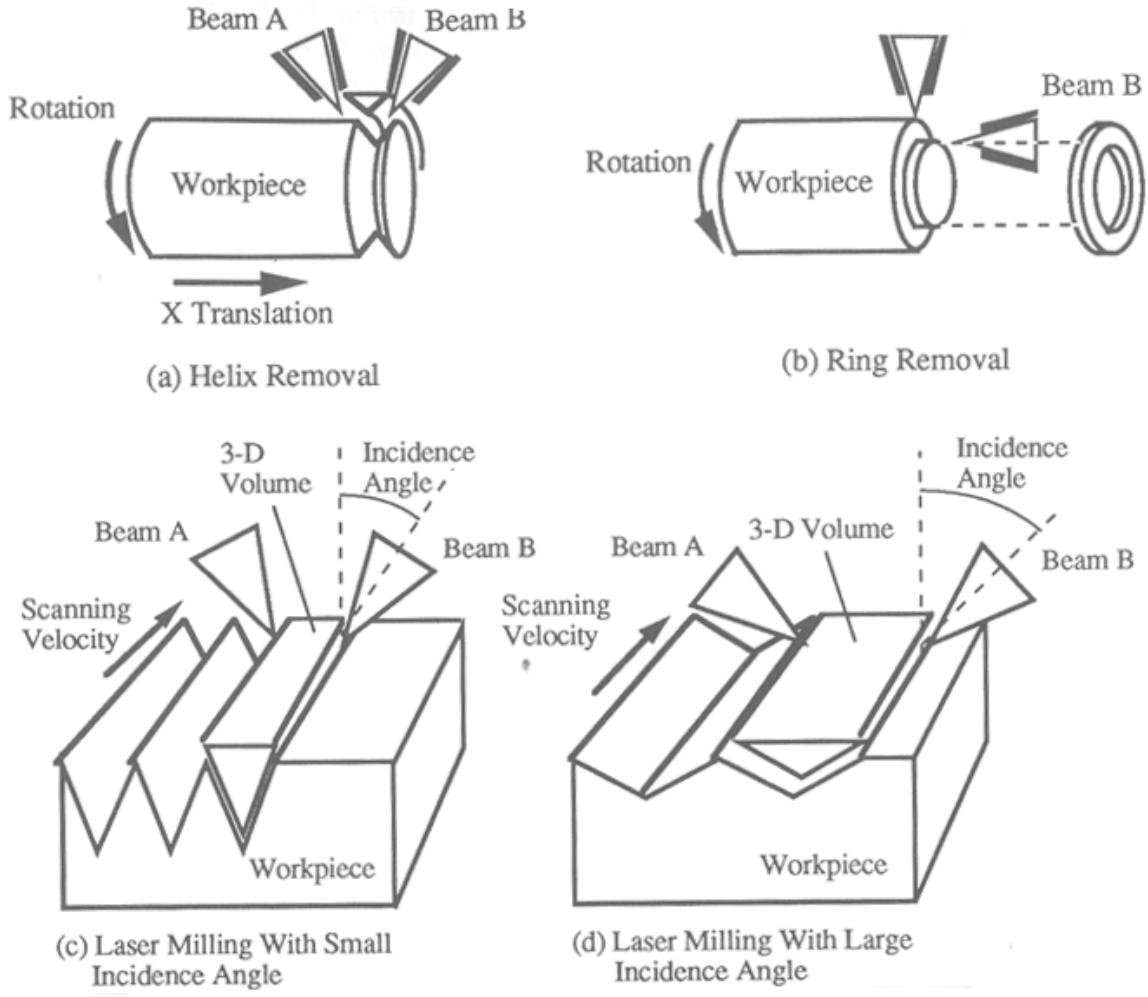

Figure 2.3: 3-D laser machining [13]

2.1 *Laser Assisted Mechanical Machining at the Macroscale*

Laser assisted mechanical machining at the macroscale has been investigated for processing hard-to-machine ceramics. This process was originally suggested by K̈onig et al. [8]. Klocke and Zaboklicki [35] studied laser-assisted turning of silicon nitride (Si_3N_4). The basic principle and the physical realization of the laser-assisted turning setup is shown in Fig. 2.4.

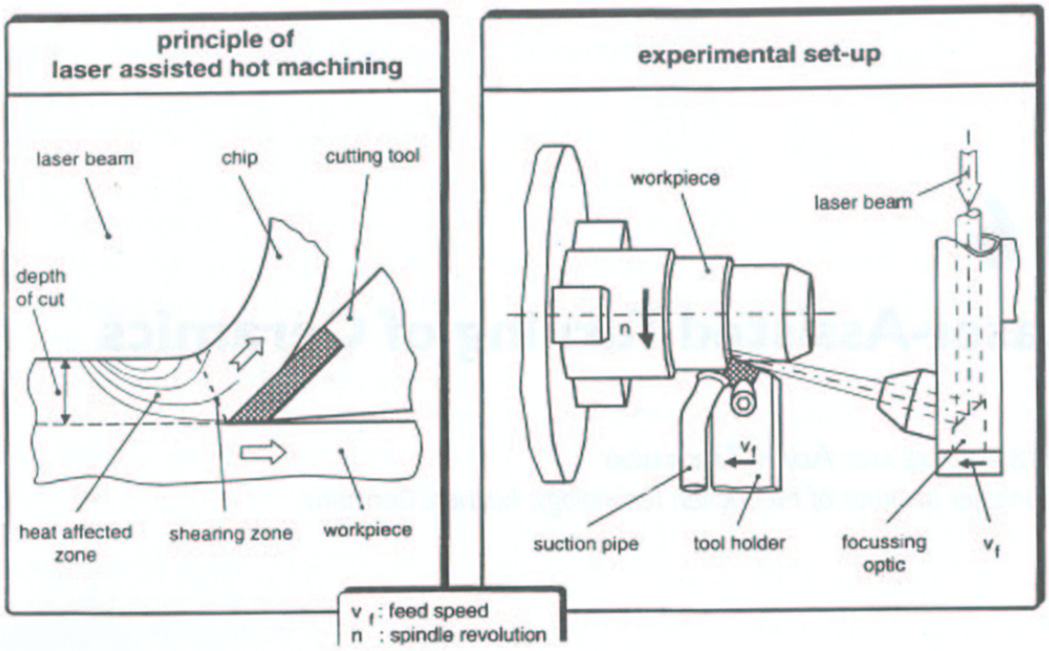

Figure 2.4: Laser-assisted turning and realization [35]

Recently, laser assisted mechanical machining (turning) of silicon nitride has been studied extensively by other investigators [36, 37]. This process makes use of a high power gas laser source (1.5 KW CO_2) that heats a sizable portion of the ceramic ahead of the cutting tool, which removes material. Study of material removal mechanisms and constitutive modeling of the shear zone stresses in this process has been reported [38]. Tian et al. [39] have developed a multiscale finite element model to simulate

the chip formation in laser-assisted machining of Si_3N_4. The model considers the workpiece heterogeneous microstructure via interfacial cohesive elements to simulate the intergranular glass phase and crack propagation in Si_3N_4. Fig. 2.5 shows the simulated chip formation.

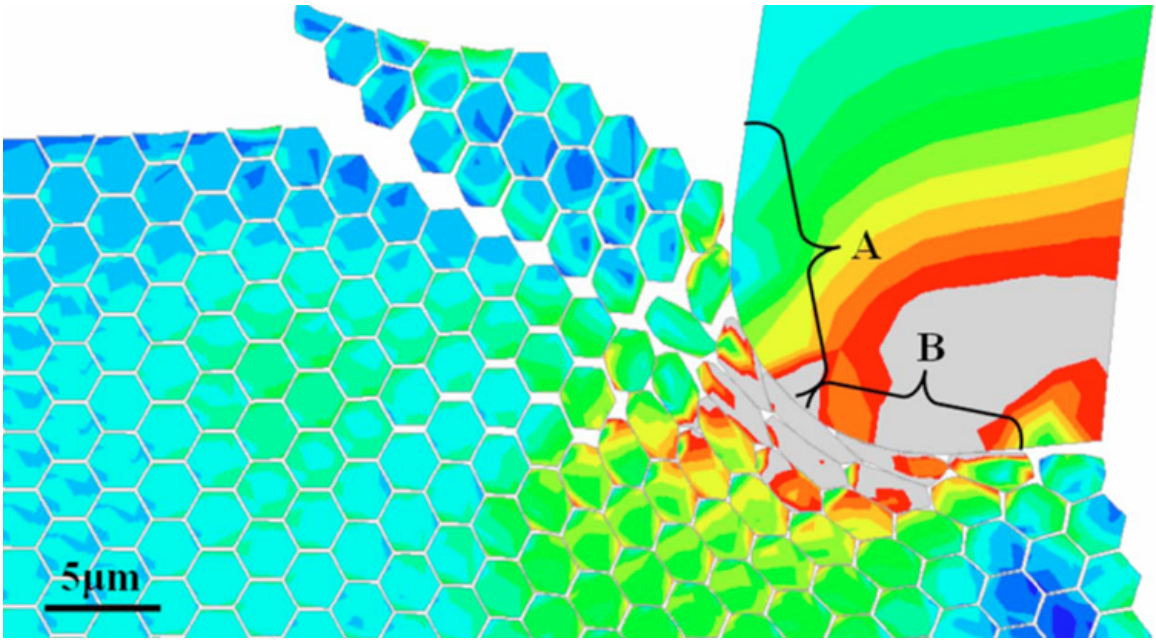

Figure 2.5: Chip formation simulation [39]

In addition, laser assisted mechanical machining of other ceramics such as sintered mullite and magnesia-partially-stabilized-zirconia have also been reported [9, 40]. These studies focus on material removal mechanisms, prediction of the temperature field, wear modeling and evaluation of surface integrity. Transient thermal analysis using numerical models [9, 41, 42] have been carried out for macroscale laser assisted turning. Rozzi et al. [41, 42] modeled a translating laser beam used to heat a rotating workpiece. The model incorporates the effects of surface emission and convection at the machined and unmachined surfaces. For low-thermal diffusivity aerospace alloys plasma-assisted milling has also been reported at the macro scale [43]. Kaldos et al. [44] have reported a two-step procedure for die making that consists of roughing by conventional milling followed by finishing with a 100W Nd:YAG laser. Other related

works include laser assisted machining of compacted graphite iron [45], Inconel 718 [46] and high power diode assisted turning of D2 tool steel [47].

2.2 Pure Laser Machining at the Microscale

Prior work in laser machining of microscale features is mostly limited to ablation processes. The excimer laser (UV, ns pulses) has been used traditionally but other pulsed lasers like CO_2, copper vapor, Nd:YAG and its harmonics have also been used for ablative micromachining [48]. Industrial uses include drilling of High Density Polyethylene (HDPE), laser drilling of via holes in interconnection packages, drilling of inkjet printer nozzles, micromachining of biomedical devices (PVC bilumen catheter, pH-sensor wire etc.) and MEMS [31]. Laser micromachining can be used for fabricating masks, which define shapes or patterns. Alternatively, there are direct write methods that can be interfaced with a CAD system [49]. Zhang et al. [32, 33, 34] studied laser induced plasma assisted ablation for micromachining glass and fused quartz with higher harmonics of the Nd:YAG laser. Fig. 2.6 and Fig. 2.7 show scanning probe microscope images of a square grating created by laser ablation of fused quartz and optical images of holes drilled in fused quartz and Pyrex, respectively.

Hayden et al. [50] investigated laser ablation assisted fabrication of masks made of glass coated with gold-chrome layer used in photolithography. Laser micromachining of ceramics (Si_3N_4, Al_2O_3, ZrO_2) and diamond through ablation was studied by Hellrung et al. [51] while Yang et al. [52] created copper micro-patterns on silicon substrates. This method simplifies manufacturing of printed circuit boards. Exner et al. [53] simulated the material removal by TEA (Transversal Electrical Excitation at Atmospheric pressure) CO_2 laser ablation process using a half empirical rotation symmetrical model. Pfledging et al. [54, 55] focused on rapid fabrication of microcomponents using laser micromachining for mold insert and replication in PMMA

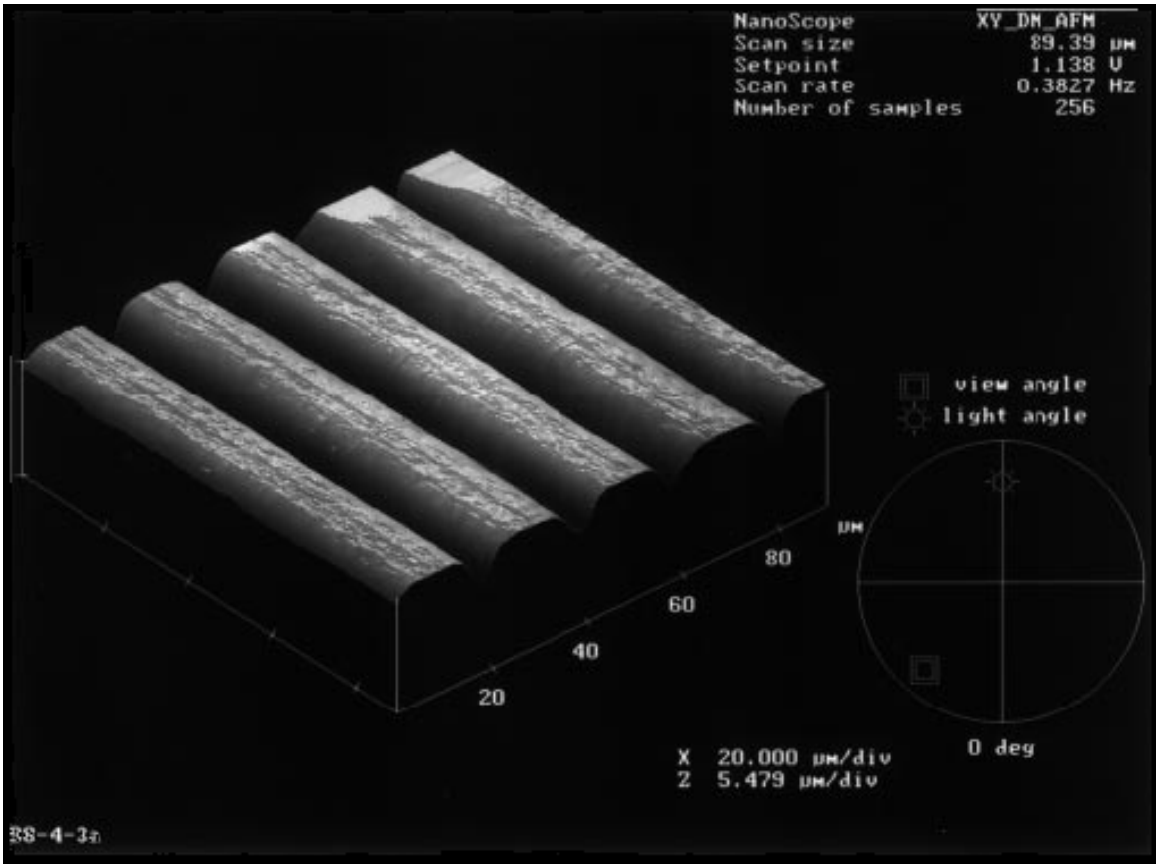

Figure 2.6: Three-dimensional image of square grating produced by laser micromachining [34]

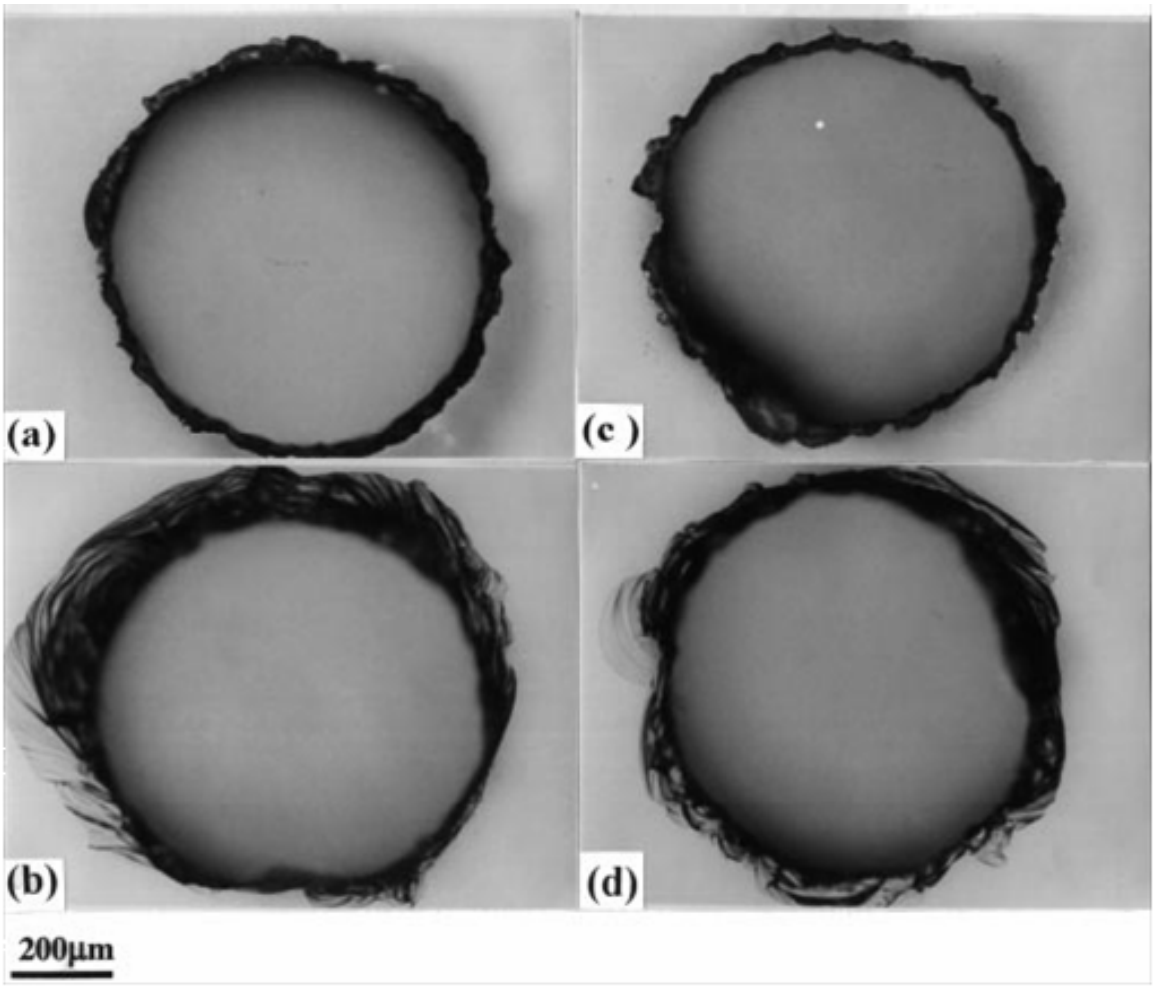

Figure 2.7: Optical microscope images of holes produced in fused quartz (a: rear surface, b: front surface) and Pyrex glass (c: rear surface and d: front surface) by laser micromachining [34]

using photomolding.

The use of ultra-short pulsed (e.g. femtosecond) UV lasers for pure laser micromachining has drawn the attention of researchers in the past few years. These laser systems have been successfully applied to micromachining of masks for lithography, MEMS, photonics, coronary stents and dental surgery [6, 56, 57, 58, 59, 60]. The primary motivation for their use has been has been the small spot sizes, high laser intensity ($\sim$Terawatts/cm^2), high peak power ($>$ 10 GW), small heat affected zone, burr free surfaces, fine detail and tight tolerances that these systems are capable of producing. These characteristics enable efficient laser ablation of transparent materials [61]. It can also be used for processing dielectrics [62]. Studies have been reported on the application of such laser systems in microfluidics [7] and silica ablation [63]. Deep-drilling of hard metals with a femtosecond laser has been shown to increase the hardness of the material in the ablation zone although the residual surface does not show any deterioration [64]. Processing of hard metals using nano/femtosecond lasers for pure laser micromachining of WC-Co has also been reported [65]. More detailed and higher quality processing is possible with UV lasers with shorter pulse (ns, fs) durations. Unfortunately, this is at the expense of average power and productivity. Material removal rate (MRR) is an issue in femtosecond laser machining. Typical etch rates for nanosecond and femtosecond lasers vary from 1- 0.032 μm/pulse. Typical feature size is between 3-20 μm [66]. The typical MRR's are of the order of 0.1 mm^3/min for deep drilling of hardened steel and 1 mm^3/min for grooving in PMMA [65, 66]. In contrast, in pure mechanical micromachining (e.g. micromilling), a MRR of 25 mm^3/min has been reported [67]. Although ultra-short pure laser micromachining can give fine detail, it is a slower process and much better suited for processing of thin films. In addition, generating a sculpted surface with complex three-dimensional surface features can be difficult with these systems.

2.3 Pure Mechanical Micromachining

In recent years, pure mechanical micromachining (e.g. micro grooving/turning/milling) has gained considerable attention due to its potential advantages noted previously. Friedrich et al. [68, 69] adapted the macroscale milling process for microscale fabrication of masks for lithography. The milling tools used ranged from 22-100 μm in diameter. Their efforts were focused primarily on machining of PMMA, a relatively soft plastic. They later extended it to mask fabrication of layered architecture titanium and gold films on graphite. These masks were subsequently used in deep X-ray lithography. Fig. 2.8 shows trench and stepped structures micromilled in PMMA using a 22 μm diameter milling tool; trenches are 62 μm deep and consist of 15 steps.

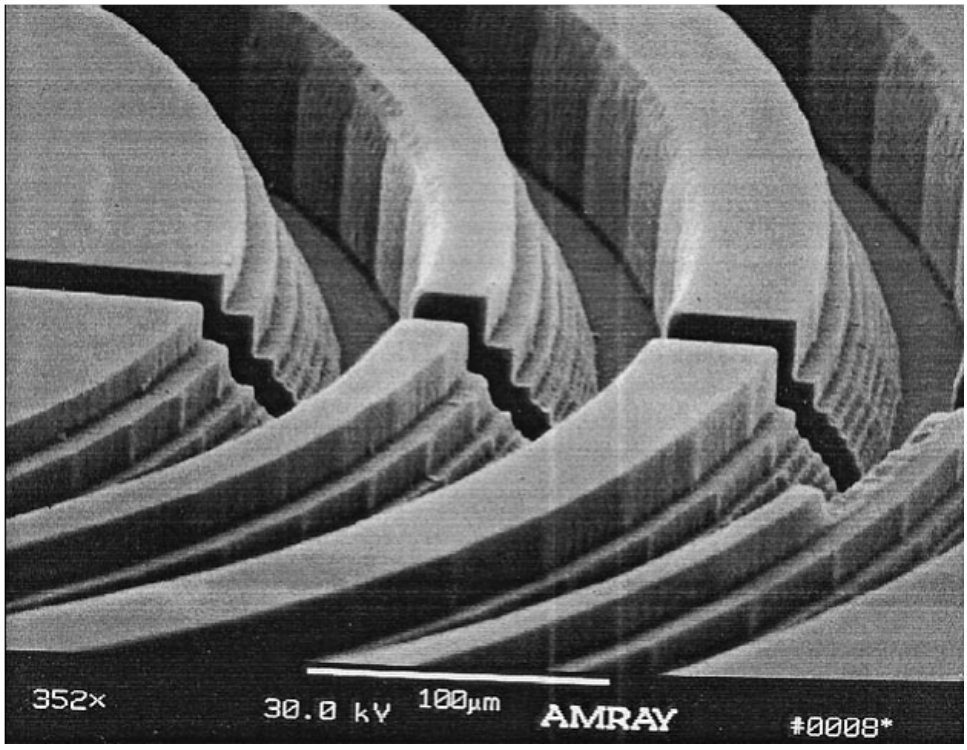

Figure 2.8: Micromilled trench and stepped structures in PMMA [69]

Schaller et al. [70] suggested that mechanical micromachining was an effective way of fabricating mold inserts. These inserts are used in hot embossing where the mold insert is pressed under vacuum into a semi-finished plastic layer heated

above the glass transition temperature. Inserts fabricated by micromachining have also been used in powder injection molding at the micro-scale. MicroPIM (Powder Injection Molding) uses ceramic or metallic powder with a binder system that is processed in a furnace to remove the binder system and then sintered [70]. Thus, the fabrication of micromolds is becoming an increasingly important application of mechanical micromachining. Schaller et al. [71] also investigated micromachining of aluminum, copper, brass and other non-ferrous materials by profiled micro-diamond tools on an ultra-precision machine tool. Micro milling of hard ferrous metals using diamond tools presents considerable tool wear problems. Adams et al. [72] combined focused ion beam sputtering with mechanical micromachining. Tackas et al. [73] studied milling of metallic materials. The end mills used in his study ranged from 150-600 μm diameter. Rahman et al. [74] studied micro milling of copper with a 1 mm end mill aimed at investigating material removal and wear mechanisms.

Most of the studies employing pure mechanical micromachining are experimental in nature. Very limited modeling effort in mechanical micromachining has been reported. Yong et al. [75] modeled cutting forces for shallow cuts in hard turning. Vogler et al. [76] modeled micro milling of multiphase materials. Both analytical [77] and numerical [78] models of orthogonal micro cutting incorporating strain gradient effects active at small depth have been presented. Fig. 2.9 shows strain gradient contours in micro cutting with uncut chip thickness of 1 μm and 10 m/min cutting speed. Recently, Liu et al. [68] modeled the dynamic effect of elastic recovery in micro milling of single phase ferrous materials. Cox et al. [79] studied thermal, static, and dynamic stability of a precision micromachining setup. The effect of edge radius becomes important at low depths of cut typically encountered in mechanical micromachining. The effect of edge radius has been modeled using slip line field theory [80, 81, 82]. Venkatachalam et al. [83] modeled the effects of ploughing forces and friction coefficient in microscale machining. They used an integration approach to

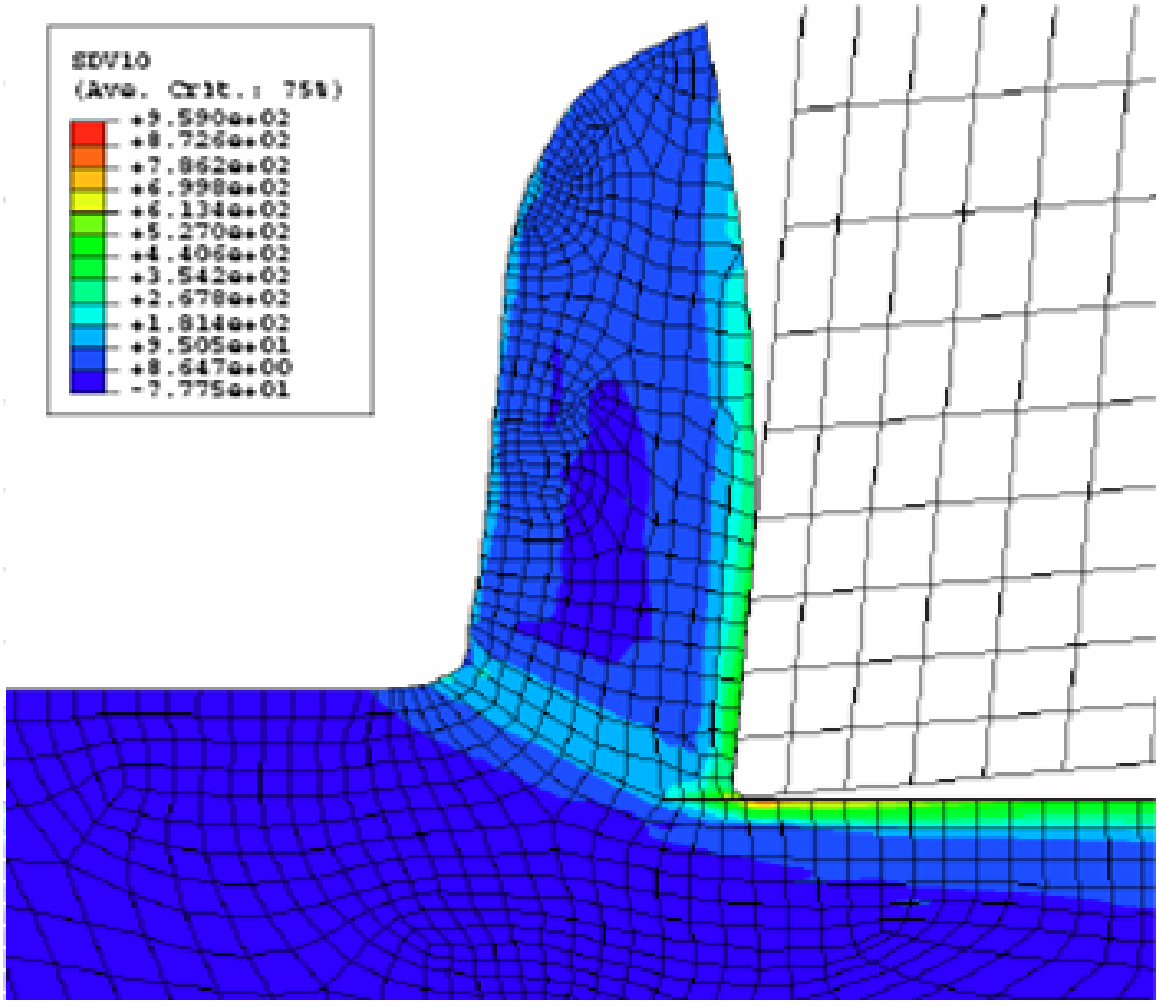

Figure 2.9: Strain gradient contours in micromachining [78]

estimate the ploughing force and the friction model shown in Fig. 2.10 assumes hard transverse cylinder sliding on a soft surface. A few other studies account for elastic recovery of the workpiece material in micro milling [84, 85].

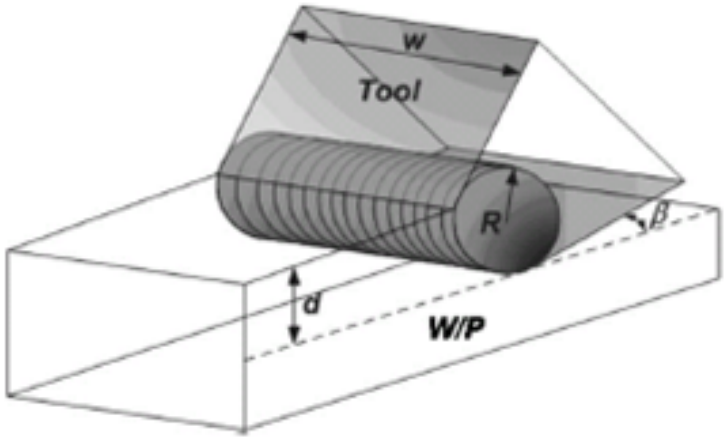

Figure 2.10: Schematic of the tool ploughing the workpiece [83]

2.4 Thermal Modeling of a Moving Heat Source

The LAMM process developed in this thesis involves a moving heat source on a semi-infinite body. Consequently, a brief review of the relevant works on thermal modeling of a moving heat source is warranted. Jaeger [86] derived analytical temperature field solutions for a moving heat source applied to semi-infinite bodies. Welding process characterization efforts have used transient and quasi-static solutions for a moving heat source [87, 88]. The quasi-steady state three dimensional problem of a moving circular Gaussian heat source for a finite depth and width was solved by Manca et al. [89]. Komanduri et al. [90, 91] recently solved the problem of a circular disk moving heat source with a Gaussian distribution. The solution domain is illustrated in Fig. 2.11 and the solution for temperature rise is given by the Eq. 2.1.

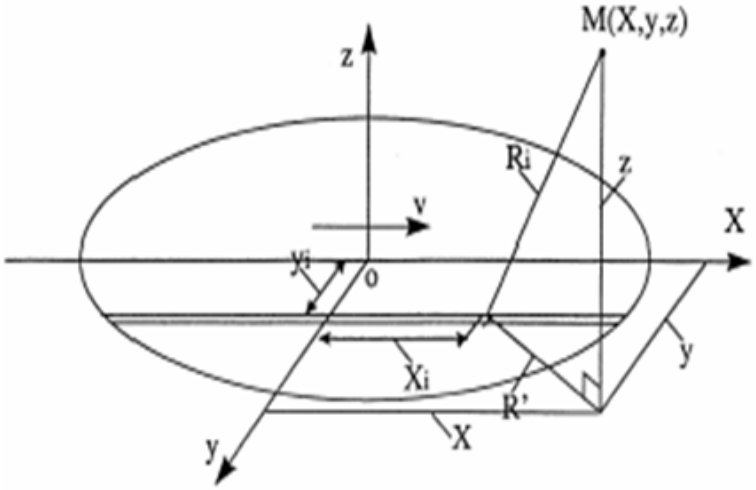

Figure 2.11: Schematic of disk heat source [91]

$$\theta_M = \frac{9qv}{4\lambda a\pi^{3/2}r_0^2} e^{-XV} \int_0^{r_0} e^{-(3r_i/r_0)^2} r_i dr_i \int_0^{\omega} \frac{e^{-\omega-\frac{u^2}{4\omega}}}{\omega^{3/2}} d\omega \times I_0 \left[\frac{r_i V^2}{2\omega} \sqrt{\left(x + \frac{2\omega}{V}\right)^2 + y^2} \right] \tag{2.1}$$

where, q = laser power, a = thermal diffusivity of the medium, λ = thermal conductivity, r_0 = beam radius of the laser, v = scan velocity, $V{=}v/2a$, r_i = instantaneous radius (varies from 0 to r_0), $\omega = v^2\,\tau/4a$ for transient; for quasi-steady state $t{=}5$ and I_0 = Modified Bessel function of the first kind of order zero.

In certain situations, such as when the characteristic dimension of the physical object subjected to thermal loading is of the same order of magnitude as the mean free path of phonon interaction O(10^{-8}m) for metals (longer for dielectrics) and/or the response time of heat transport in the medium is of the same order of magnitude as the mean free time of phonon/electron interaction (O(10^{-12} s) for metals; O(10^{-9}-10^{-12} s) for dielectrics), standard macroscale heat conduction models are no longer

accurate and microscale heat transfer models that consider the individual phonon-electron interaction (in metals) and phonon scattering (in dielectrics) are needed [92, 93]. These situations arise when processing thin films using ultra-short pulse width (e.g. picosecond/femtosecond) lasers. In the present work, however, these conditions are not met and, consequently, macroscale moving heat source conduction models are still useful.

2.5 Laser Assisted Mechanical Micromachining

Laser assisted machining of hard materials at the micro scale is a relatively recent development. Early investigations of laser-assisted micro-grooving of as-received AISI 1018 steel and later for H-13 by Singh and Melkote [11, 94] demonstrated the potential of the hybrid approach. Recently, Jeon and Pfefferkorn [95] have examined the effect of laser preheating on micro-end milling of relatively soft engineering metals (Al 6061-T6 and 1018 steel). They however used a conventional milling machine integrated with a 100 W Nd:YAG laser with a relatively large (mm sized) beam diameter. Also, hard-to-cut materials were not studied in their work. Fig. 2.12 shows the the schematic for laser preheating in micro-end milling.

2.6 Summary

It is clear from the literature survey that:

- Very limited experimental and theoretical work has been carried out on hybrid micro manufacturing processes, in particular, laser assisted mechanical machining at the micro scale.
- Pure laser micromachining and pure mechanical micromachining processes, when used separately, are limited in their abilities to process hard materials.
- A logical solution to address the above limitation is to develop a hybrid process

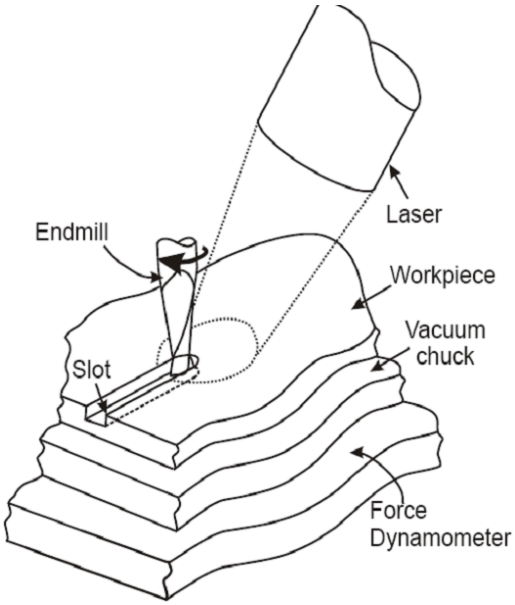

Figure 2.12: Schematic of laser preheating in micro-end milling [95]

that combines the beneficial features of these two methods.

The rest of this thesis describes the development and characterization of a hybrid laser-assisted mechanical micromachining process via experimental and modeling approaches.

CHAPTER III

DESIGN, FABRICATION AND TESTING OF LASER-ASSISTED MECHANICAL MICROMACHINING SETUP

This chapter is aimed at designing and fabricating a setup to realize a hybrid micromachining process for hard materials that combines the beneficial aspects of laser heating and 3D mechanical micro-cutting. As mentioned earlier, there is a need to enhance the pure mechanical micromachining process by developing methods to overcome its limitations. This chapter describes the design, fabrication and testing of the first and second generation LAMM machines for simple micro-grooving operations to understand the process mechanics. The grooving operation can be modeled as an orthogonal cutting process and analytical models can be developed for cutting force, temperature distribution and machine elastic deflections that in turn will provide the process know-how to control and optimize the process.

3.1 Basic Approach

The basic approach consists of combining a low-power continuous wave fiber laser with a mechanical micro grooving process. The laser beam, which is 70-120 μm in spot size, is focused in front of a miniature grooving tool (300 μm -1 mm in width) to soften the workpiece material just ahead of the cutting tool thereby lowering the forces required to cut the material. Once modeled and understood, local thermal softening can be controlled and confined to the material volume being removed by the tool, thereby minimizing thermal damage in the machined surface. The design

and fabrication approach and associated preliminary experimental investigation are reported in the following sections of this chapter.

3.2 Design and Fabrication of the First Generation LAMM Setup

A schematic of the first generation LAMM setup for 3-D micro-grooving is shown in Fig. 3.1. An actual picture of the first generation LAMM setup is shown in Fig. 3.2.

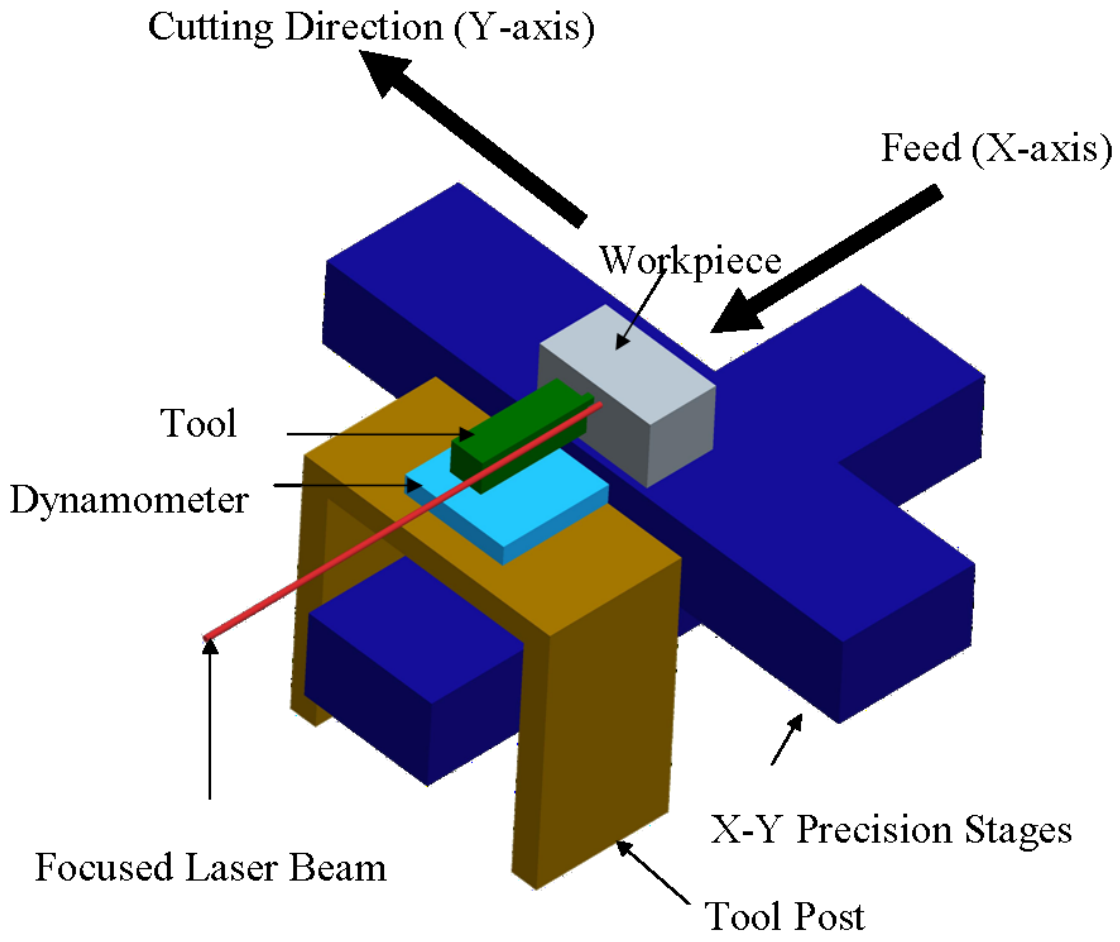

Figure 3.1: Schematic of laser-assisted mechanical micro-grooving process

A 10 W solid-state Ytterbium fiber laser (Model YLM-10, IPG Photonics) is integrated with a precision 2-axis motion control stage (Aerotech ATS-125). The positioning resolution of the stage is 0.1 μm with 1 μm accuracy per inch of axial

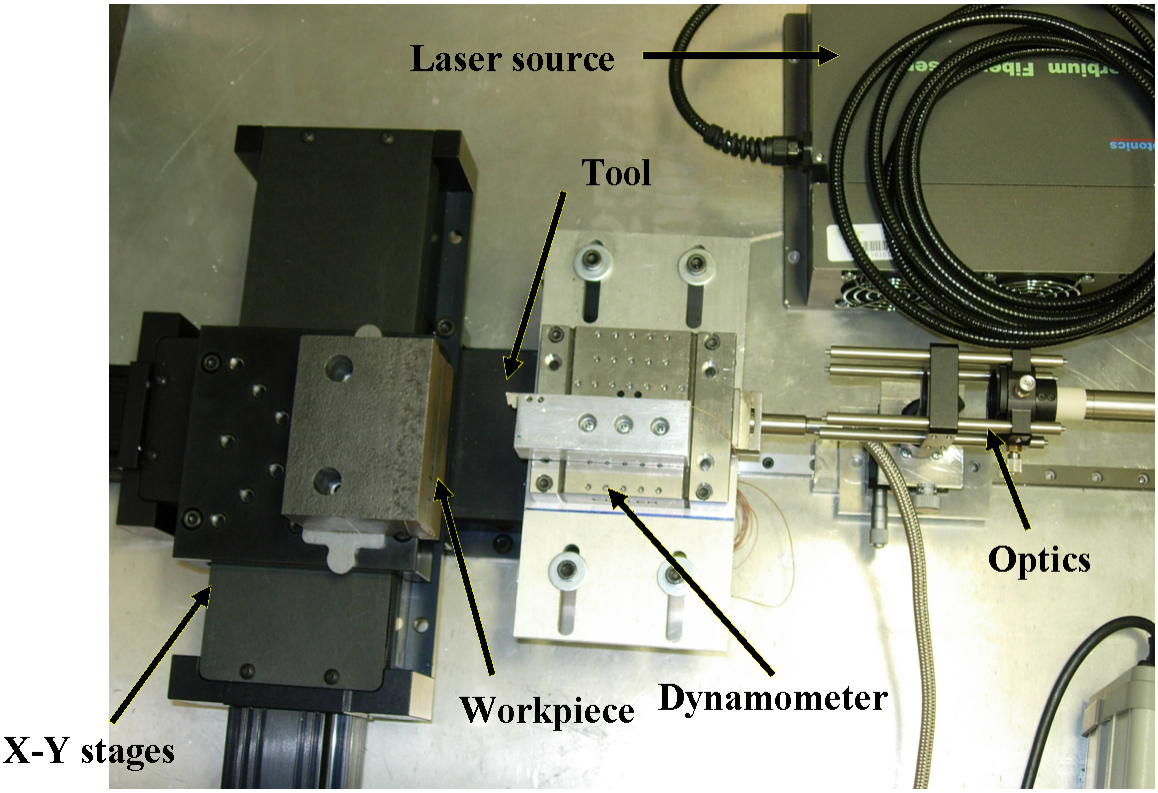

Figure 3.2: Picture of first generation laser-assisted mechanical micro-grooving setup

travel. The only moving component is the workpiece, which is mounted on the stage. All other components including the tool holder and laser are stationary. As such, the machine is capable of generating features on the order of a few microns. The laser beam is emitted from a 7 μm diameter single mode fiber through a collimator. The beam has a near infrared wavelength of 1064 nm. A red aiming beam that is collinear with the laser beam allows the laser beam to be approximately spotted. The collimator and focusing lens are mounted on a small Y-Z stage mounted on the carriage of a precision slide. The distance of the focusing lens from the workpiece can be adjusted to vary the spot size of the laser. The focal length of the lens used in the current setup is can be varied from 250 mm to 400 mm, which yields a laser spot diameter of about 70 μm and 110 μm. The laser controller is used to modulate the laser power.

The components of the setup are mounted on an aluminum base plate and the entire setup is placed on a vibration isolation table. The setup is instrumented to measure the cutting forces using a piezoelectric force dynamometer (Kistler Minidyne 9256 C2). The tool holder is mounted on the dynamometer and holds a micro grooving tool of 100-1000 μm cutting width. The dynamometer is bolted to the tool post. The top plate of the tool post has slots for adjusting the location of dynamometer and tool holder.

The cutting tool material used in this study is tungsten carbide (WC) coated with TiAlN. The rake angle is 0^o, the back clearance angle is 2.5^o and the side clearance angle is 5^o. The workpiece is fixed to the X-Y stages that move it in the X and Y directions. The stage has a maximum speed of 30 m/min, 100 mm maximum travel, and can withstand up to 180 N axial force. The feed velocity is obtained by moving the workpiece along the X-axis while the cutting velocity is imparted by moving it along the Y-axis. A digital microscope is used to monitor the process and to precisely spot the laser beam at a known distance from the tool cutting edge.

The X and Y stages are controlled using two separate controllers integrated using the N-View software and communicate with the computer via a firewire connection. G-codes can be used to execute coordinated X-Y motion. The geometric capability of the machine is illustrated in Fig. 3.3, which shows a white light interferometer image of a sinusoidal profile cut in Al-6061.

3.3 Second Generation LAMM Setup

The tool-tool post assembly used in the first generation LAMM setup lacked sufficient stiffness. The deflections in the cutting directions were observed experimentally and also modeled in ANSYS. The result of the finite element analysis of the thinner Al-7075 plate (10 mm thickness) used in the first generation setup is shown in Fig. 3.4. The maximum deflection in the direction of the cutting force (Y-axis) for producing a 25 μm groove in H-13 steel (cutting force $\approx$ 40 N) can exceed 2 μm.

To increase the stiffness of the tool post was made thicker (25 mm thick side walls)in the second generation setup. The slots and bolting assembly used in the first generation setup were eliminated and the tool post was made out of single piece of Al-7075. It can be seen in the finite element simulation in Fig. 3.5 that the design change yields a much lower deflection under similar loading conditions. The maximum deflection in the direction of cutting force is 0.3 μm.

The other important change is the integration of a 35 W fiber laser (Model YLM-30, IPG Photonics) into the second generation LAMM setup. This increased power will result in higher temperatures in the workpiece and consequently higher thermal softening can be achieved. The picture of the improved second generation LAMM setup is shown in Fig. 3.6.

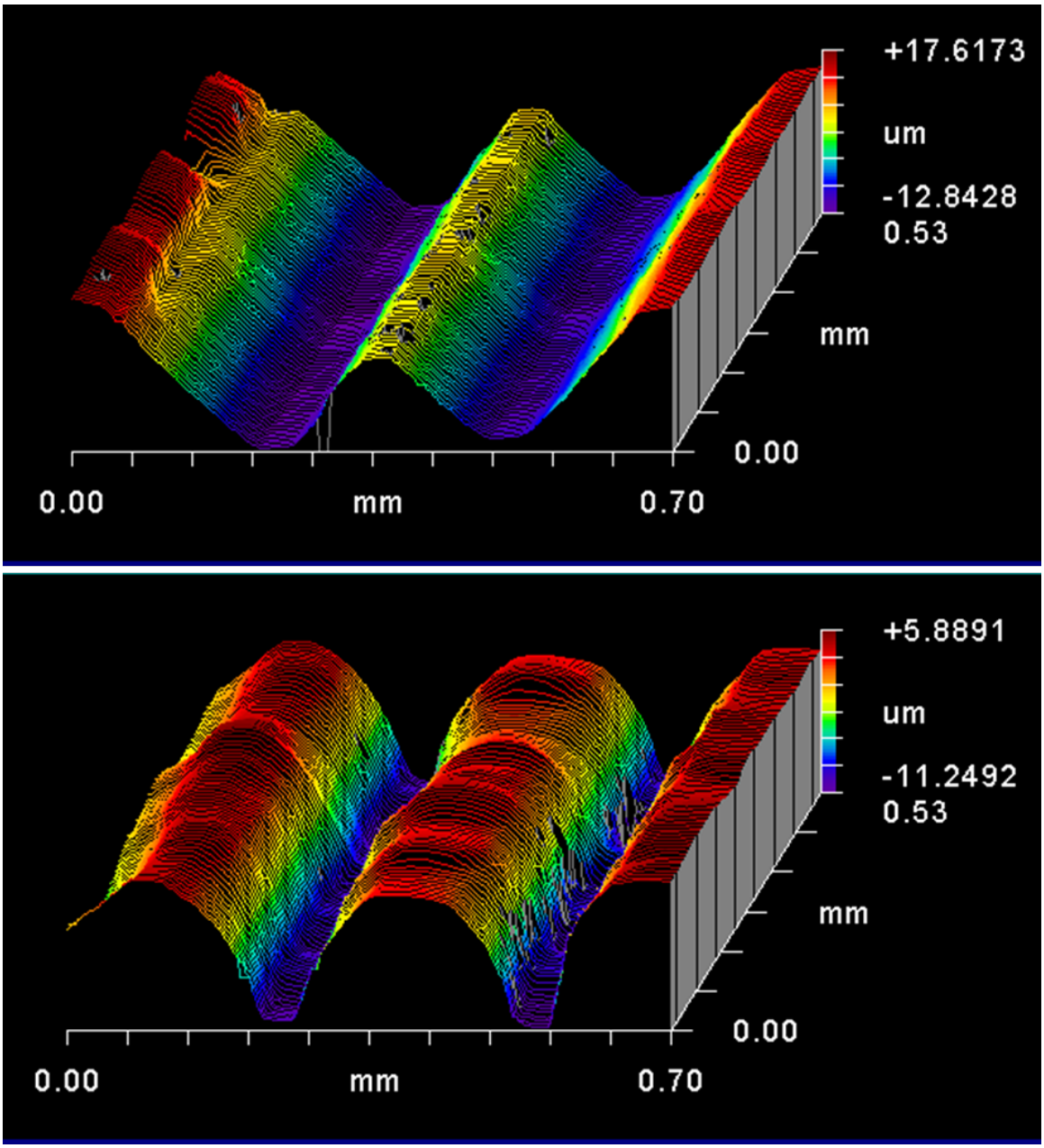

Figure 3.3: Sinusoidal profiles created by laser-assisted mechanical micro-grooving process for 1 mm tool width, 5W laser power, spot size 110 μm, 10 mm/min cutting speed and 15 μm depth of cut

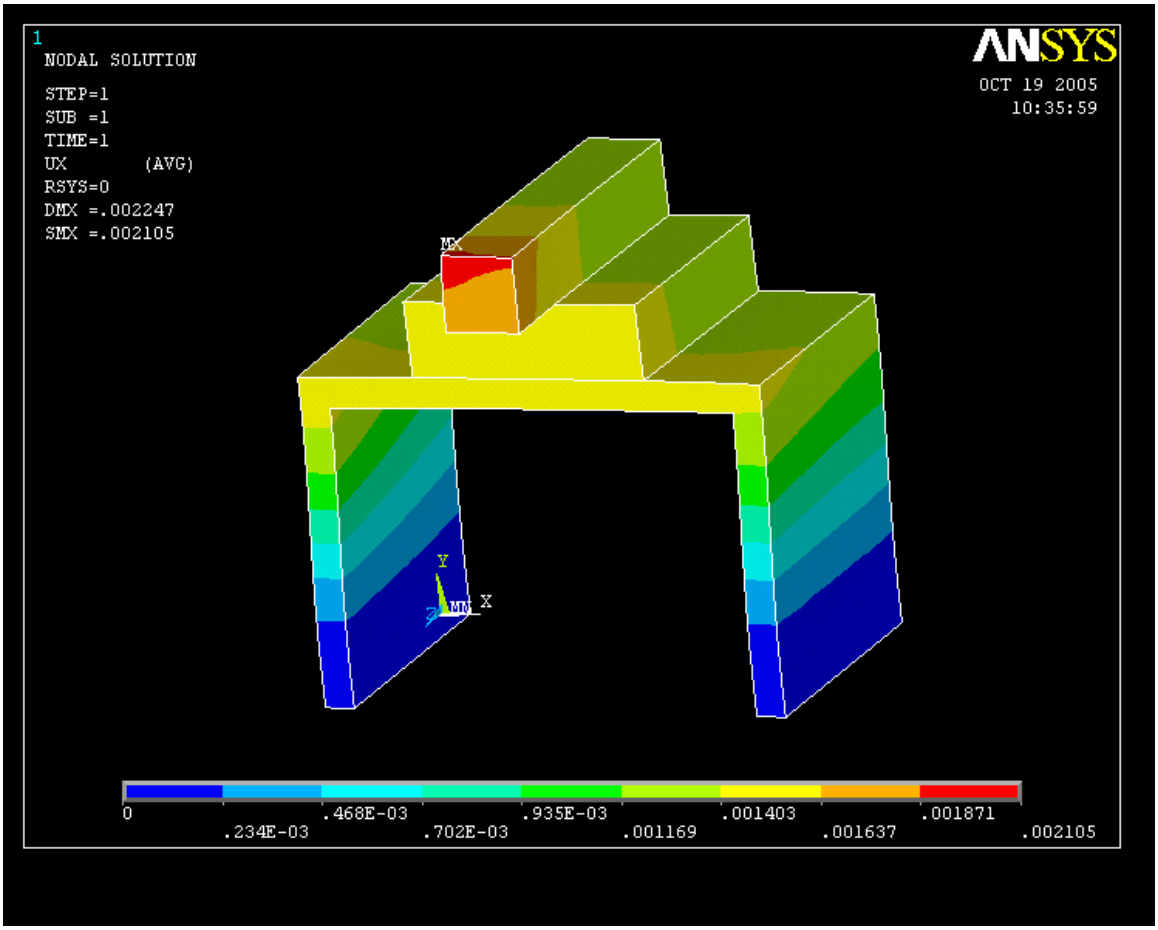

Figure 3.4: Deflections in tool-tool post assembly in first generation LAMM setup

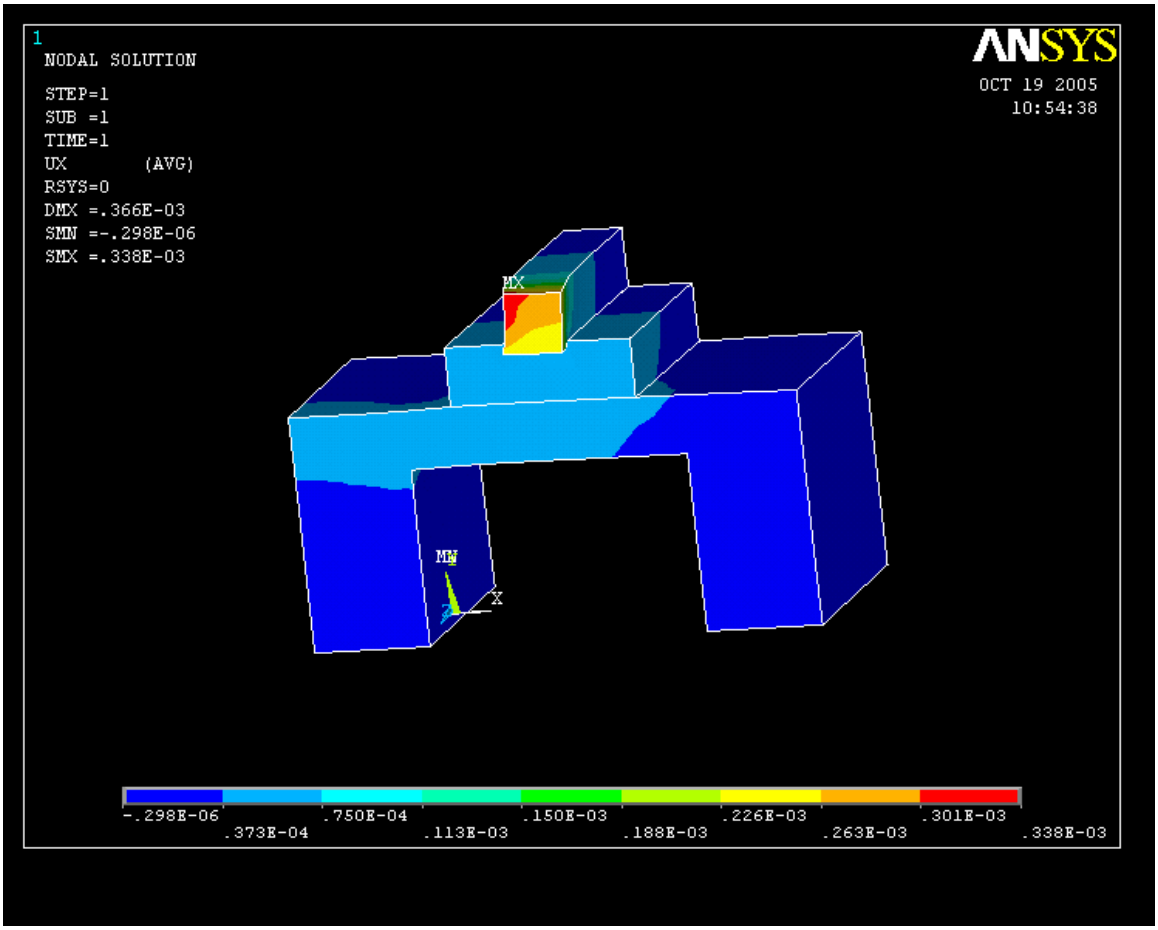

Figure 3.5: Deflections in tool-tool post assembly in second generation LAMM setup

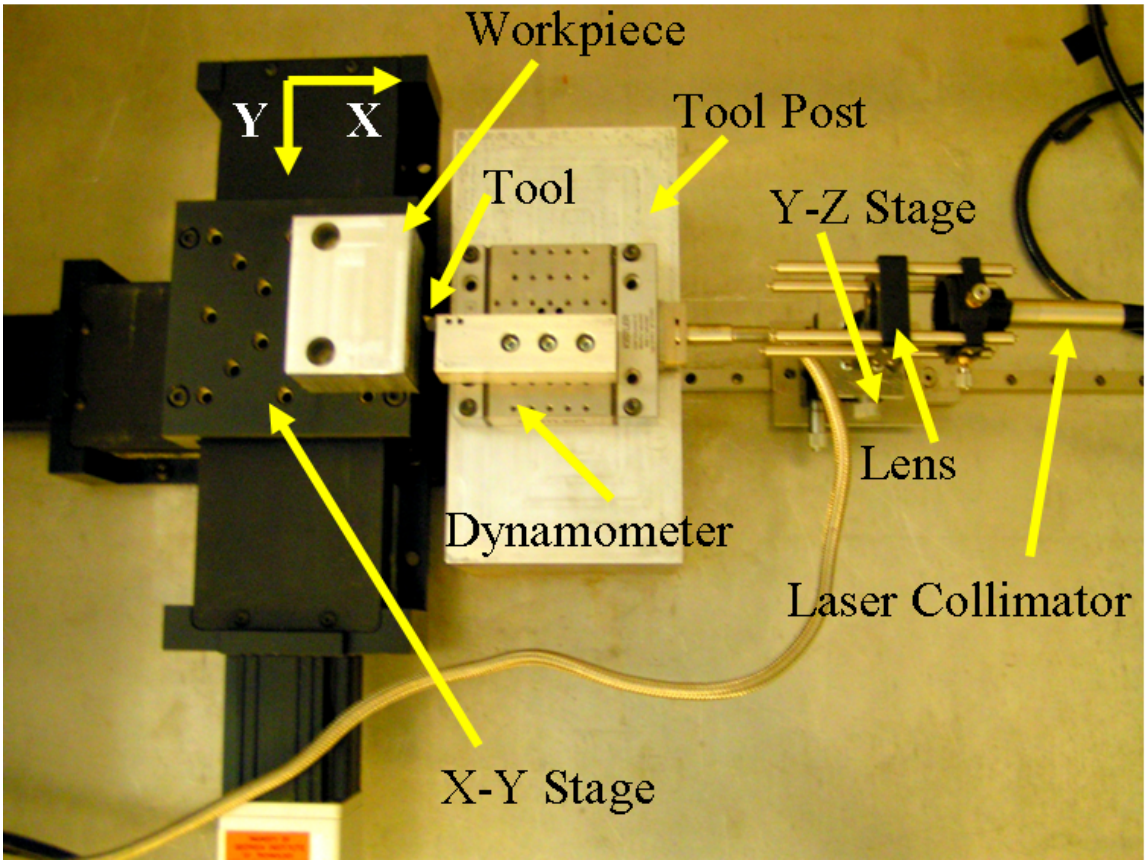

Figure 3.6: Picture of second generation laser-assisted mechanical micro-grooving setup

3.4 Preliminary Investigation of Laser-Assisted Micromachining

Preliminary micro-grooving experiments were conducted with the continuous fiber laser to study the feasibility of laser-assisted mechanical micromachining of as received 1018 steel. The nominal composition of 1018 steel is given in Table 3.1. The laser beam is focused in front of a miniature cutting tool to soften the workpiece material prior to cutting thereby lowering the forces required to perform the operation. Initial results shown in Fig. 3.7 reveal that thermal softening and subsequent lower cutting forces are observed with 1 mm wide tool, 5 μm depth of cut, 10 mm/min cutting speed, 10 W laser power and 70 μm spot size. It can be seen that there is a 30% reduction in cutting forces which indicates that the LAMM process indeed induces thermal softening.

Table 3.1: Nominal chemical composition of 1018 steel

C	Mn	P	S
0.15-0.20%	0.60-0.90%	0.04%	0.05%

A simple two-level experiment with four factors was designed to further investigate the effect of laser variables (spot size and laser power) and cutting parameters (depth of cut and cutting speed) on the cutting forces in machining 1018 Carbon Steel. Table 3.2 shows the factors and the values of both levels for each factor.

Table 3.2: Factors and their levels for 1018 steel experiments

Levels	Laser Power (W)	Depth of Cut (μm)	Cutting Speed (mm/min))	Laser Spot Size (μm)
0	5	5	10	70
1	10	10	50	110

The ANOVA performed on the measured cutting force data based on the design

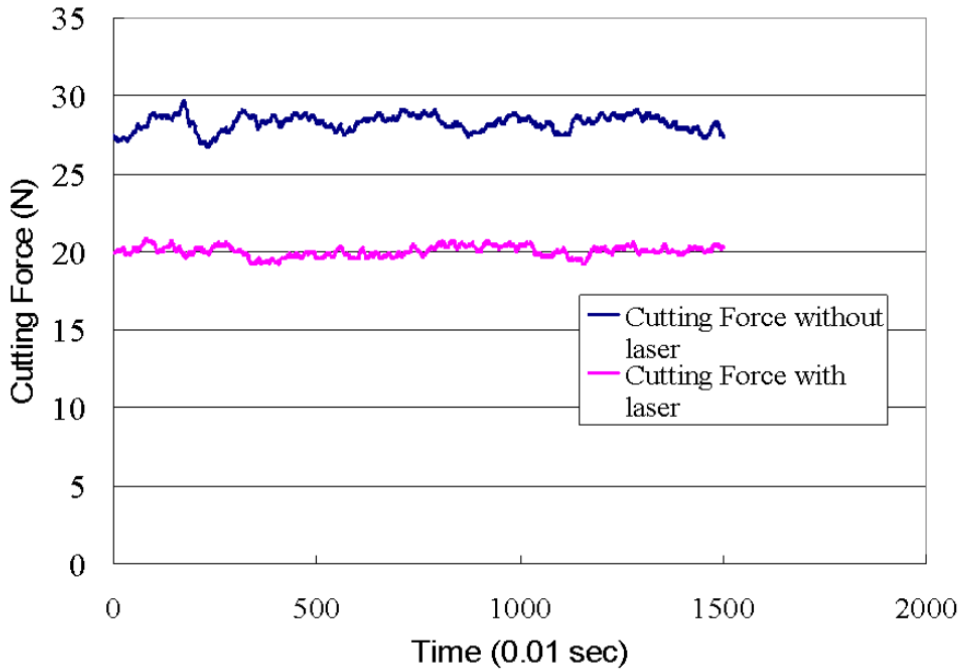

Figure 3.7: Effect of thermal softening on cutting force

of experiments showed that the main effects of depth of cut and laser power are significant. Two-way interaction effects of spot size/depth of cut and spot size/cutting speed on the cutting speed are statistically significant at an level of 5%. Fig. 3.8 shows the Pareto chart, which shows the comparison of main and interaction effects.

The main effect plot of the mean cutting force is shown in Fig. 3.9. The plot for spot size is flat, which signifies that during the transition from 70 μm to 110 μm there is no appreciable change in the mean cutting force. The depth of cut is a significant factor as there is an increase of 48% in the mean cutting force when the depth of cut increases from 5 μm to 10 μm. The increase in depth of cut is expected to increase the cutting forces owing to more material being removed and hence more material resistance. The cutting speed exhibits slight increase in cutting forces when the speed increases from 10 mm/min to 50 mm/min. The laser speed controls the time available for heat conduction and hence thermal softening. The effect of laser

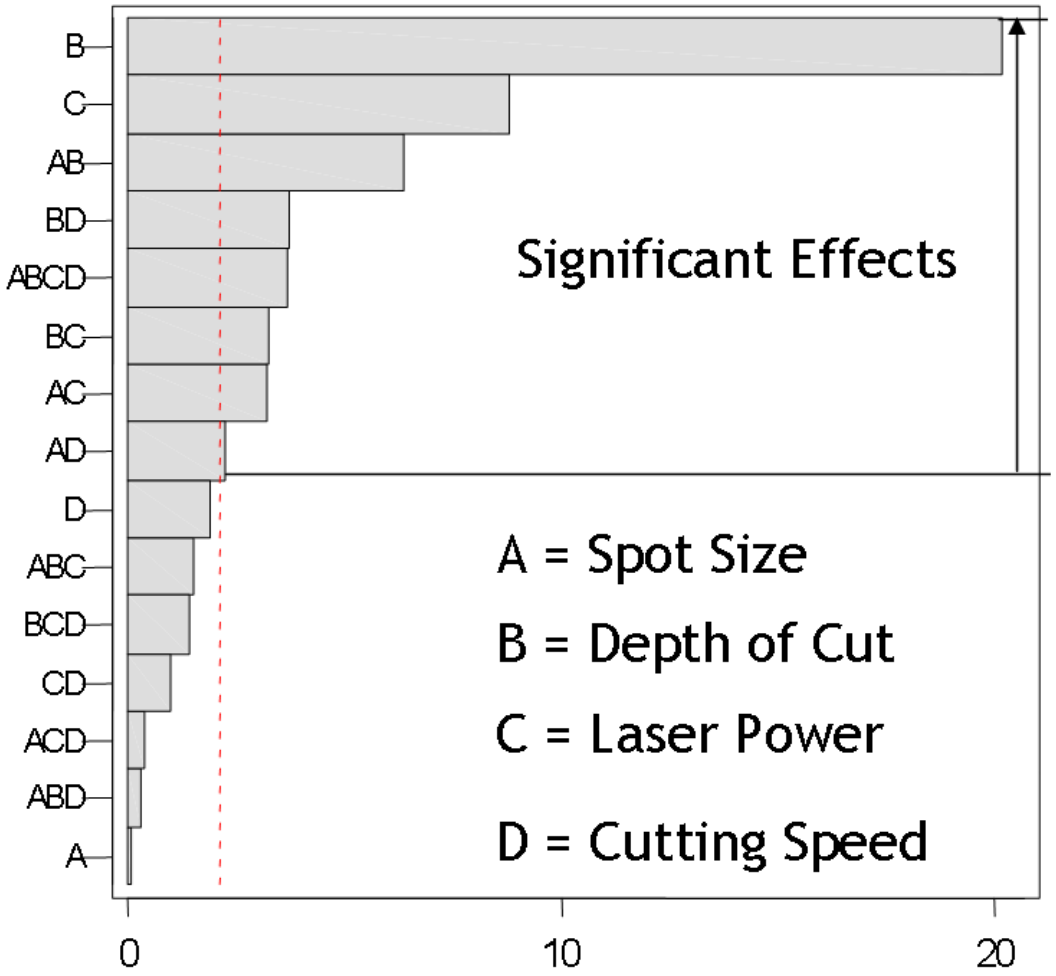

Figure 3.8: Pareto chart for main effects

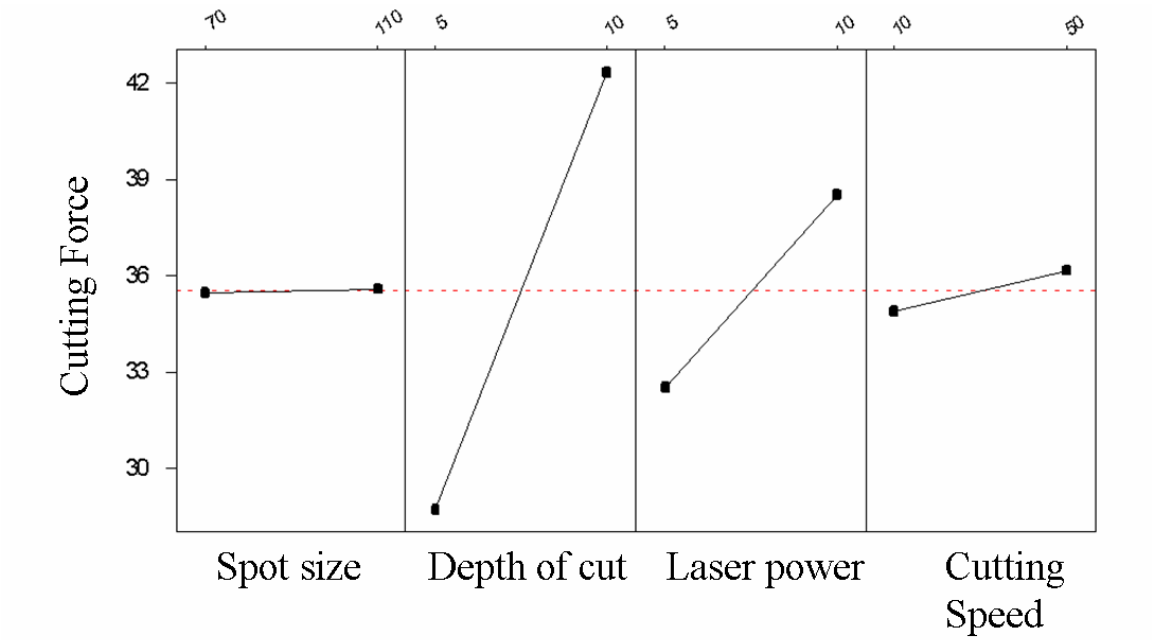

Figure 3.9: Main effects on cutting forces

power is contrary to expectation as the cutting force increases with the increase in laser power. A possible explanation for this behavior is the effect of thermal expansion of the tool and workpiece, which results in an increased depth of cut. This behavior needs further investigation and a detailed experimental characterization of the LAMM process for hardened H-13 mold steel is conducted in the following chapter.

3.5 Summary

In this chapter, design and fabrication of a setup for laser-assisted mechanical micromachining was presented. A preliminary experimental study of the process was conducted to determine proof of concept. These initial experiments demonstrate that laser assisted mechanical micromachining can lower the cutting forces. This method can possibly overcome the limitations of tool stiffness, strength and excessive wear usually encountered in micromachining of hard-to-machine materials and enable faster micro cutting of these materials. The softening is achieved in some cases while

in other cases the cutting force shows an increase with laser power. This phenomenon needs to be studied further. The following chapter presents a detailed experimental characterization of hardened mold steel (H-13, 42 HRC) to better understand the process.

CHAPTER IV

EXPERIMENTAL CHARACTERIZATION OF THE LAMM PROCESS

The previous chapter discussed the design and fabrication of the LAMM setup and demonstrated the presence of thermal softening in 1018 steel. It further revealed that the expected decrease in cutting force is not observed under all conditions. A plausible explanation for this is that the effect of thermal softening can be offset by thermal expansion of the tool, which results in an increased depth of cut. Other factors such as limited machine-tool system stiffness and tool flexural strength, specially for small footprint machines with micro-tools, are major impediments to the efficient use of mechanical micromachining methods for difficult-to-machine materials such as mold and die steels. In addition, at micron length scales of cutting, the effect of tool/machine deflection on the dimensional accuracy of the machined feature can be significant. This chapter presents a detailed experimental characterization of the Laser Assisted Mechanical Micromachining (LAMM) process designed for three-dimensional micro-grooving. To understand the LAMM process, a design of experiments method is employed to investigate the effects of laser variables and cutting parameters on the cutting forces and surface finish in micro cutting of heat treated mold steel (H-13, 42 HRC). The effects of tool/machine deflections and tool thermal expansion on the depth of cut are also evaluated.

4.1 Experimental Work

4.1.1 Design of Experiment

The workpiece material used in this study (H-13 steel, 42 HRC) finds application in the fabrication of molds and dies for micro-injection molding of polymeric biomedical implants. The nominal chemical composition of H-13 steel is given in Table 4.1.

Table 4.1: Nominal chemical composition of H-13 steel

C	Cr	Mn	Mo	V
0.40%	5.25%	0.40%	1.35%	1.00%

A full factorial design of experiment was used to investigate the effects of laser and cutting parameters on the cutting force and surface roughness. The maximum laser power was limited by the first generation LAMM setup that had a 10 W fiber laser system. Consequently, the three levels of 0, 5 and 10 W of laser power were selected in order to explore the entire range available. Subsequently, with the addition of a slightly higher power laser in the second generation system, additional tests were conducted at 35 W laser power and 10 and 100 mm/min cutting speeds. It is known from the experiments described in the previous chapter that variation in spot size in the feasible range of the setup does not have a significant effect on the cutting force. Hence, the laser spot size was fixed at 70 μm. The combination of laser location, speed and depths of cut were selected so that there is approximately 50% reduction in the flow stress of H-13 tool steel due to thermal softening. The five factors and their respective levels are given in Table 4.2. The full factorial design consisted of 96 test runs. Three replications were conducted for each test condition.

The measured responses of the experiments included the cutting (Y) force, thrust (X) force, and the three dimensional arithmetic surface roughness parameter, S_a.

Table 4.2: Factors and their levels for H-13 mold steel experiments

Levels	Depth of Cut (μm)	Tool Width (μm)	Cutting Speed (mm/min)	Laser Location (μm)	Laser Power (W)
0	10	300	10	100	0
1	15	500	50	200	5
2	20				10
3	25				

4.1.2 Experimental Procedure

The distance of the laser from the tool was determined by burning a spot on the workpiece with the laser and measuring its location relative to the tool cutting edge using the digital microscope as seen in Fig. 4.1. If the spot was not at the desired location, the laser collimator was translated (on the precision carriage) and a new spot burnt again. This procedure was repeated until the desired location of the laser beam spot from the tool edge was achieved. The normal distance between the laser spot center and the tool cutting edge is indicated in Fig. 4.1.

The depth of cut was controlled using the X-Y stages. G-code programming was used in the NView controller software for controlling the depth of cut and imparting a constant cutting speed. The laser controller was used to set the laser power. The lengths of cut were 10 mm for 10 mm/min cutting speed and 5 mm for 50 mm/min cutting speed.

4.2 Results and Discussion

4.2.1 Effect of Laser Variables and Cutting Parameters on Forces

Analysis of variance (ANOVA) was carried out on the experimental force data to identify the main effects and interactions. The ANOVA performed on the cutting force data showed that the main effects of depth of cut, width of cut and laser power were statistically significant at a risk level (α) of 5%. Further, two-way interaction

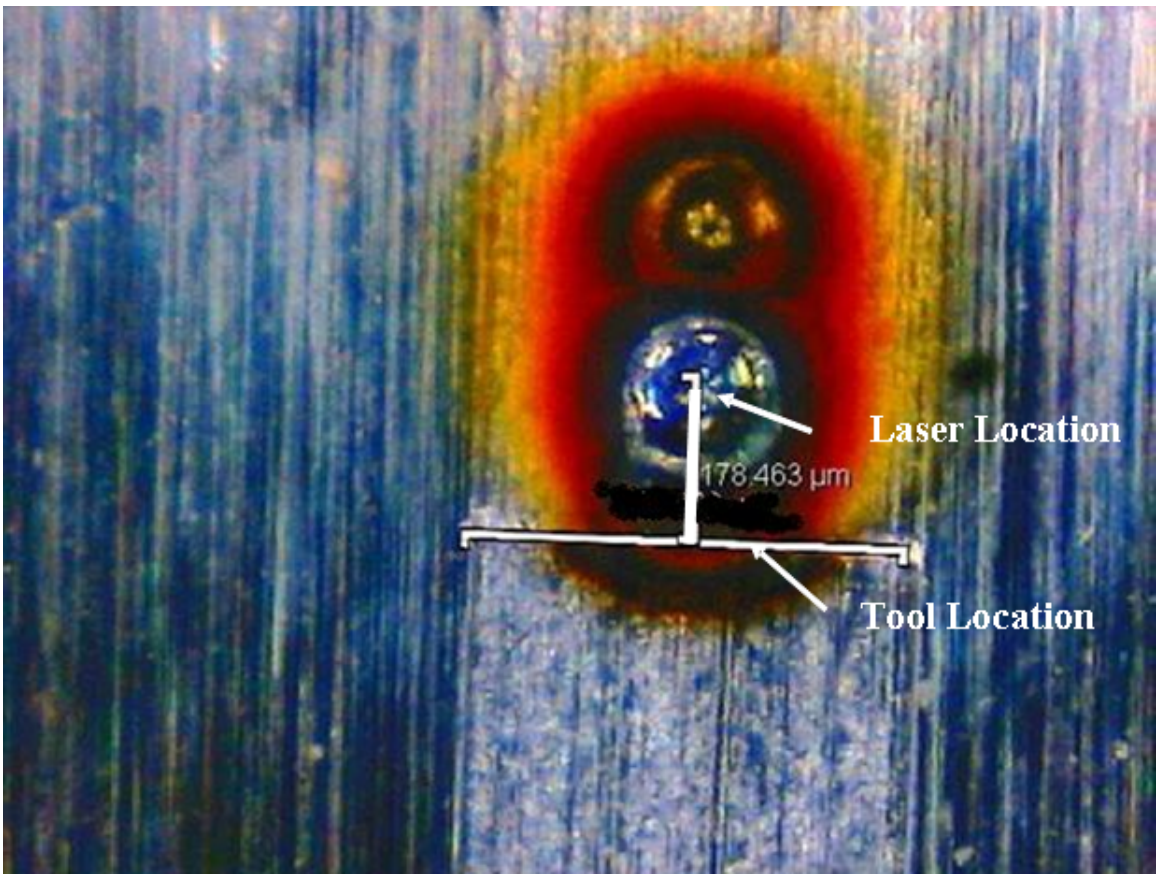

Figure 4.1: Magnified image of laser beam location with respect to the tool edge

effects of depth of cut and laser power, depth of cut and tool width, tool width and laser power, cutting speed and laser power and laser location and cutting speed on the cutting force were also found to be statistically significant at a risk (α) level of 5%. ANOVA was also performed to identify the main effects and interactions on the thrust force. The results showed that the main effects of depth of cut, width of cut, cutting speed, laser location and laser power are statistically significant at a 5% α level. Further, all two-way interaction effects except the depth of cut and cutting speed, and laser location and laser power, were found to be statistically significant at 5% level. The main effect plots of the cutting and thrust forces are shown in Fig. 4.2.

Analysis of the results in Fig. 4.2 shows a 112% increase in the mean cutting force as the depth of cut is increased from 10 μm to 25 μm. There is a 45% increase in the mean cutting force when the tool width is increased from 300 μm to 500 μm. The effect of laser power on the cutting force, even though statistically significant, is not very pronounced. An explanation for this interesting observation is given later in this chapter.

On the other hand, all main effects on the thrust force are statistically significant. The mean thrust force increases by 97% when the depth of cut is increased from 10 μm to 25 μm. The increase in tool width from 300 μm to 500 μm results in a 46% increase in the mean thrust force. These results can be easily explained by noting that an increase in the depth of cut and tool width result in a larger uncut chip area thereby increasing the cutting and thrust forces. An 8% increase in the mean thrust force due to change in laser location is seen. The mean thrust force drops by 4% with increase in the cutting speed. Although the effects of laser location and cutting speed are statistically significant, the observed change is no more than 8% , which indicates that these factors are not as important as the others. A 17% drop is observed in the mean thrust force when the laser power is increased from 0 to 10 W. This clearly indicates that laser heating does induce thermal softening, which in turn produces a

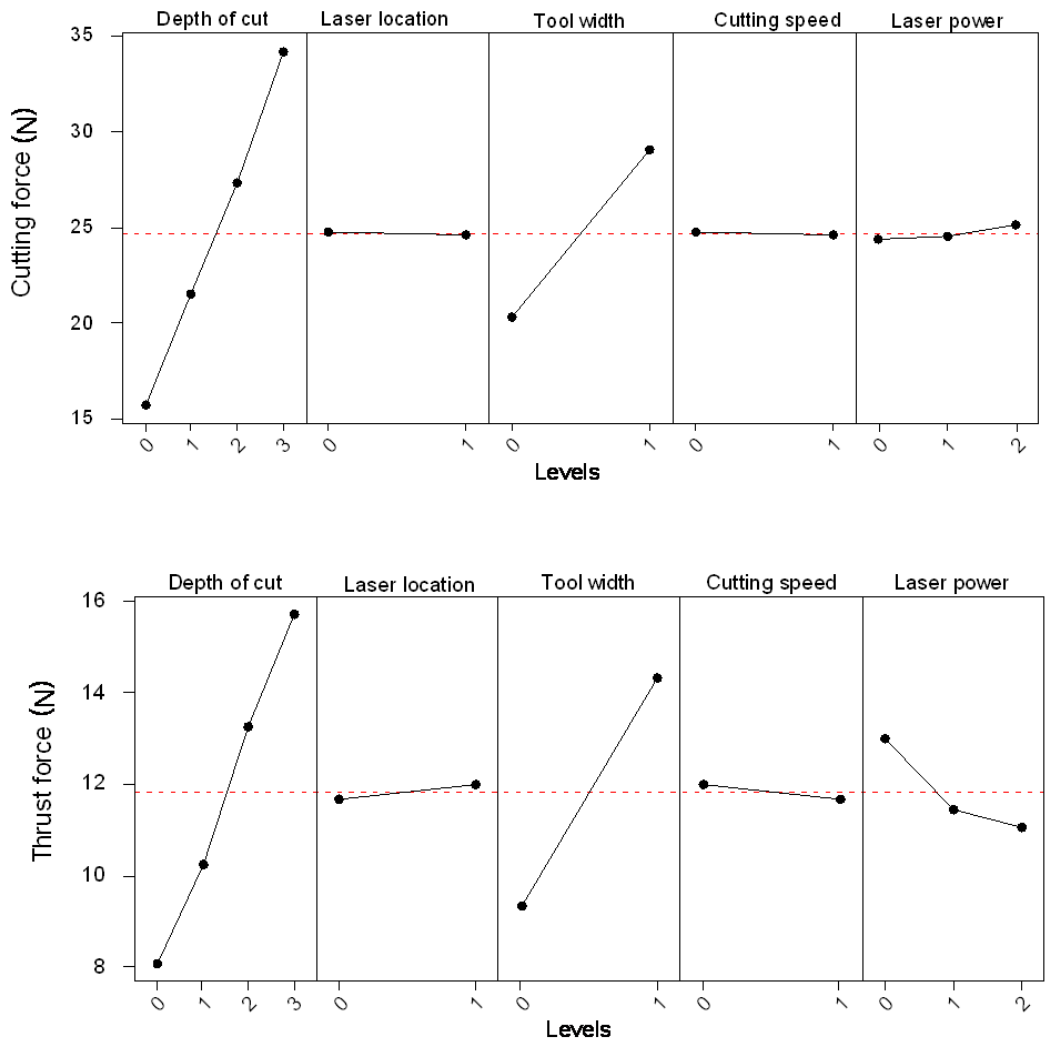

Figure 4.2: Main effect plots for cutting and thrust forces

lower thrust force.

Fig. 4.3 shows the mean and range of the cutting and thrust forces for all conditions evaluated for the 300 μm wide tool located 200 μm from the laser beam center. Paired student t-tests were performed on the difference in the mean forces and it was observed that the differences in cutting force with and without laser heating are statistically insignificant (at a risk level of 5%) for all but the two cases of 0 W and 10 W laser power and depths of cut of 20 μm and 25 μm at 10 mm/min cutting speed. The thrust force data with and without laser heating were found to be statistically different in all but three cases (0 W and 5 W laser powers for 10 μm depth of cut at 10 mm/min and 50 mm/min cutting speeds, and 0 W and 10 W laser powers for 15 μm depth of cut at 50 mm/min cutting speed). When testing for the alternate hypothesis, the thrust forces at 5 W and 10 W laser powers were found to be statistically lower than the thrust force data without laser heating, clearly indicating thermal softening due to laser heating. For the cases shown in Fig. 4.3, the cutting force does not exhibit a large change with increase in laser power for the conditions investigated. In contrast, the thrust force is seen to generally decrease with increase in laser power. This result can be explained as follows.

The LAMM setup has a finite stiffness (2.85 N/μm) and can deflect under the machining forces. Since the depth of cut is of the order of a few microns, a small deflection of the machine and/or thermal expansion of the tool in the thrust (X) direction can easily alter the depth of cut. The reduced thrust force due to laser heating causes a smaller deflection of the machine stage and this in turn yields a higher effective depth of cut than would be obtained without laser heating. In addition, thermal expansion of the tool due to laser heating ($\sim$1-3.5 μm for the conditions studied) yields a higher actual depth of cut. The cumulative increase in the depth of cut due to smaller machine deflection and tool thermal expansion can offset the effect of reduced material strength due to thermal softening. Consequently, the measured

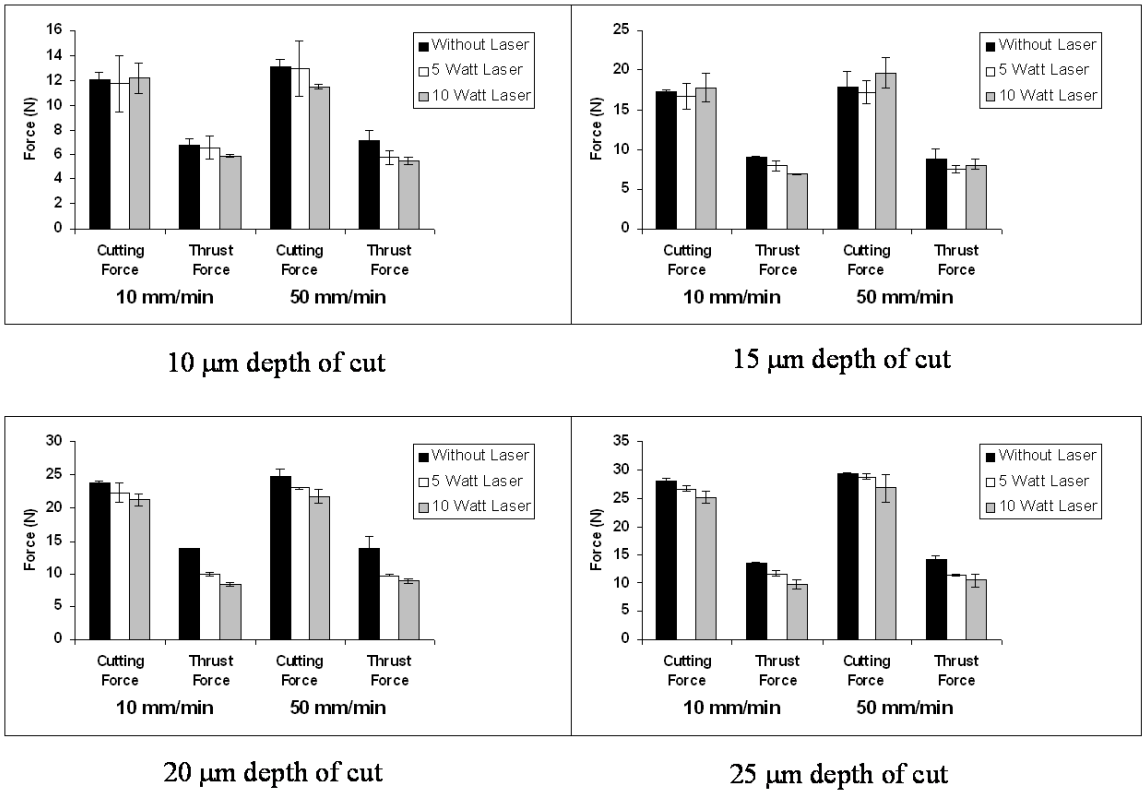

Figure 4.3: Cutting and thrust forces for 300 μm wide tool located 200 μm from the laser spot

cutting forces do not always exhibit the expected decrease with laser heating. These factors affecting the depth of cut are analyzed in detail in the next section of this chapter.

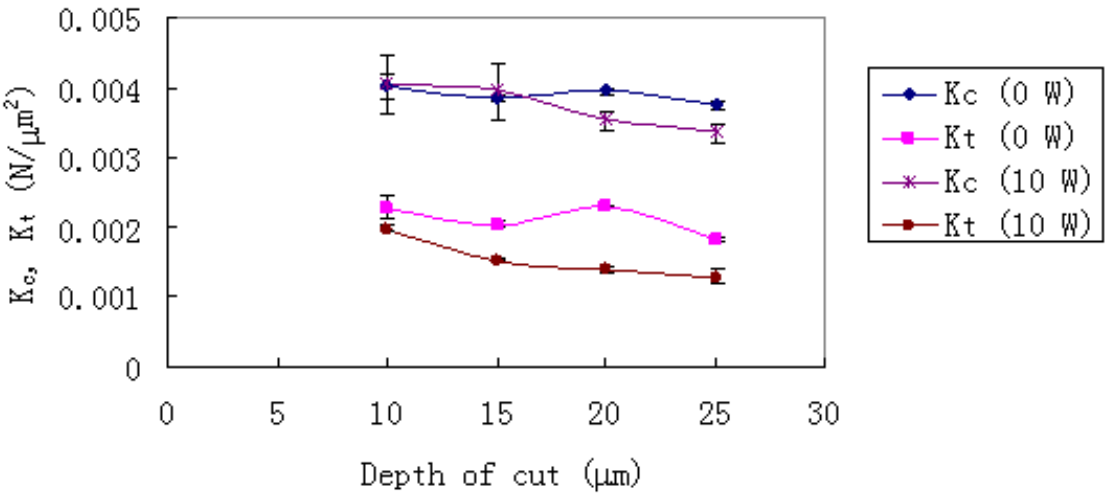

Figure 4.4: Plot of specific cutting (K_c) and thrust (K_t) pressures calculated from the measured force data and cutting conditions

Note also that the decrease is more prominent in the thrust force data than in the cutting force data due to the inherently greater sensitivity of the thrust force to changes in material strength with laser heating under the above conditions. This can be seen in the plot of specific cutting and thrust pressures shown in Fig. 4.4. These quantities were computed by dividing the respective measured force component by the uncut chip area. It can be seen in Fig. 4.4 that, for a given depth of cut, the laser power has a more noticeable effect on the specific thrust pressure than on the specific cutting pressure.

As seen in the previous section, at low laser powers ($\leq$10W), the cumulative increase in the depth of cut arising from smaller machine deflection and tool thermal expansion tends to offset some of the reduction in material strength due to thermal

softening. Following the above argument, if the laser power is increased further an appreciable thermal softening should be achievable. This is confirmed in Fig. 4.5, which shows the effect of laser power on the cutting and thrust forces for the following conditions: 300 μm tool width, 25 μm nominal depth of cut, and 10 mm/min cutting speed. As seen in the figure, significantly higher reductions in both cutting and thrust forces are seen when the laser power is increased to 35 W. The cutting force decreases by 56% and a reduction of 46% in the thrust force is observed.

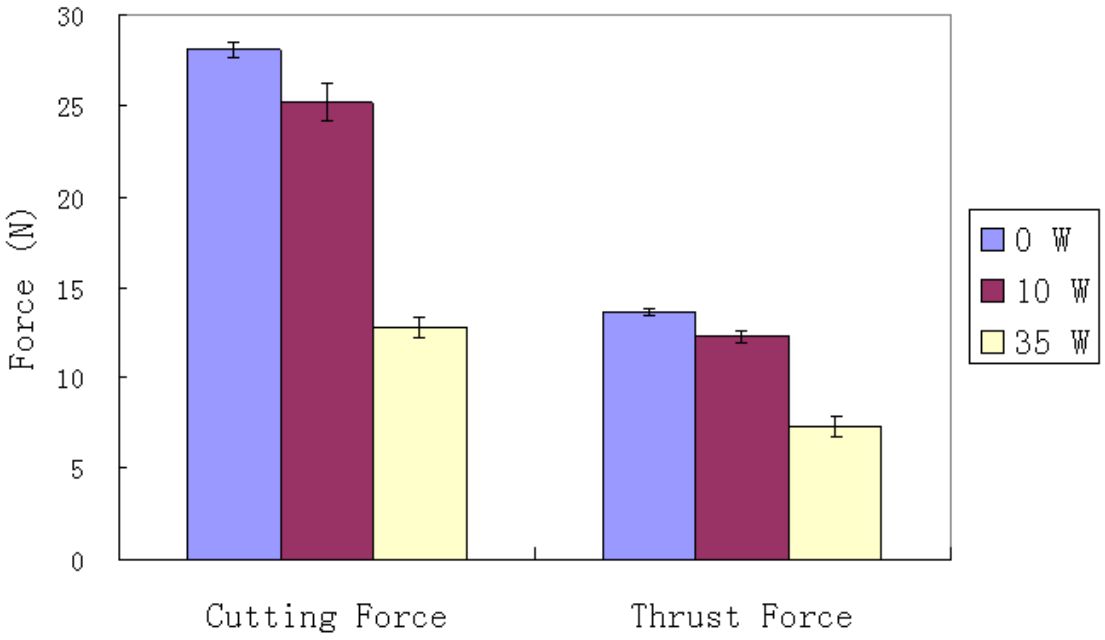

Figure 4.5: Effect of laser power on forces. Cutting conditions: 300 μm tool width, 10 mm/min cutting speed and 25 μm nominal depth of cut

4.2.2 Factors Affecting the Depth of Cut

The main factors that contribute to the change in depth of cut are the stage deflection, tool deflection and tool thermal expansion. These factors are analyzed below.

4.2.2.1 Stage deflection

The setup shown schematically in Fig. 4.6 was designed to determine the static stiffness of the stage in the depth of cut (X) direction. Two precision stages (Aerotech ATS-125) stacked perpendicular to each other and configured to perform coordinated X-Y motion were used in the experiment. A piezoelectric actuator (Physik Instru-

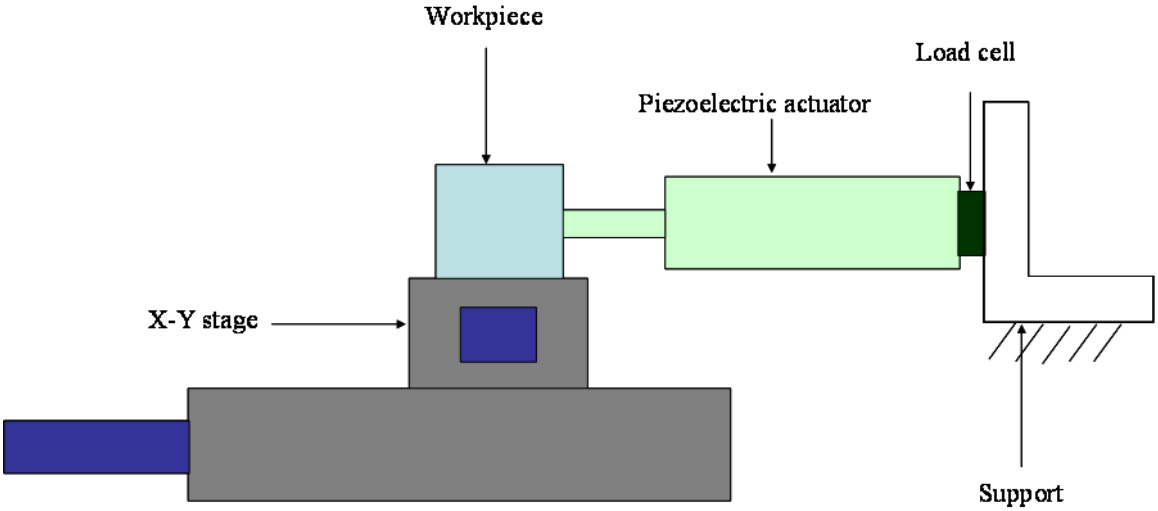

Figure 4.6: Schematic of setup for determining static stiffness of the stage

ments, PI-129077) with a maximum displacement of 30 μm was used to apply a known displacement to the stage. The piezoelectric actuator was fastened to an L-bracket as shown in Fig. 4.6 and a 3-axis piezoelectric load cell (Kistler 9251A) was sandwiched between the L-bracket and the actuator. The tip of the actuator was in contact with the workpiece, which was mounted on the top stage. The stage was translated in the X direction to make initial contact with the actuator. Once contact was made, the stage was set at that location. The actuator displacement was controlled by the current supplied by a variable power supply. The measured load versus deflection curve in the depth of cut or X direction is shown in Fig. 4.7.

Fig. 4.7 yields a maximum deflection of 22 μm for a normal load of 60 N. The highest thrust force observed in the current set of experiments is 20 N, which yields

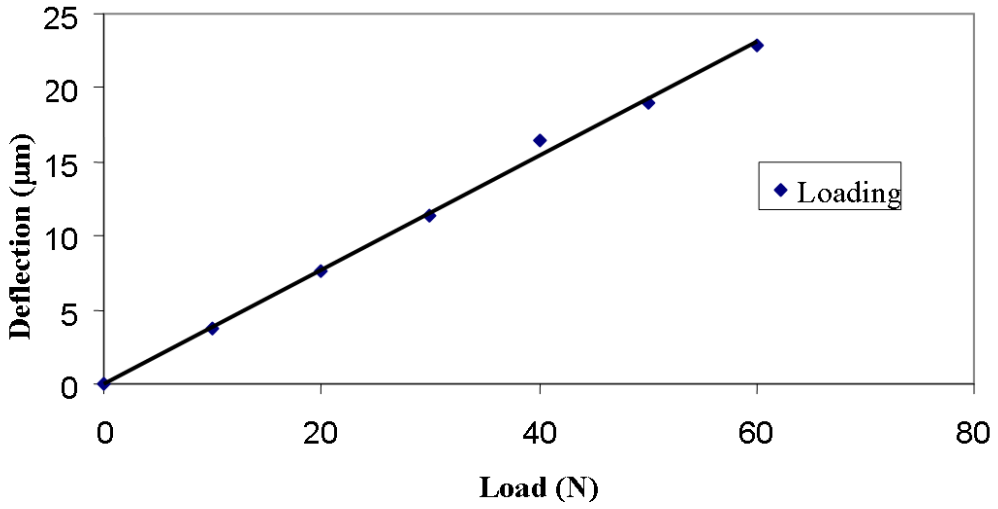

Figure 4.7: Load vs. deflection curve for the stage in the X direction

a deflection of 7 μm. Hence, in the current experiments, the actual depth of cut can vary by up to 7 μm from the nominal depth of cut due to stage/machine deflection. It can be seen from Fig. 4.7 that the stage deflection is strongly dependent on the thrust force. As discussed earlier, the mean thrust force decreases by up to 17% in the presence of laser heating. This reduction in the thrust force produces a smaller stage deflection, which results in a higher actual depth of cut compared to the case without laser heating. This increase in the actual depth of cut tends to partially offset the effect of laser softening of the material and thus partly explains the observed behavior of the cutting force, especially at lower laser power settings.

4.2.2.2 Tool deflection

The load-deflection curve for the cutting tool was simulated using the ANSYS ® finite element software. The tool holder, dynamometer and the tool post were considered to be rigid with respect to the overhung tool and consequently, only the tool was modeled.

The actual shape of the 300 μm wide grooving tool was modeled using solid 3-D 8-node brick elements (Solid 45). The modulus of elasticity of the tungsten carbide

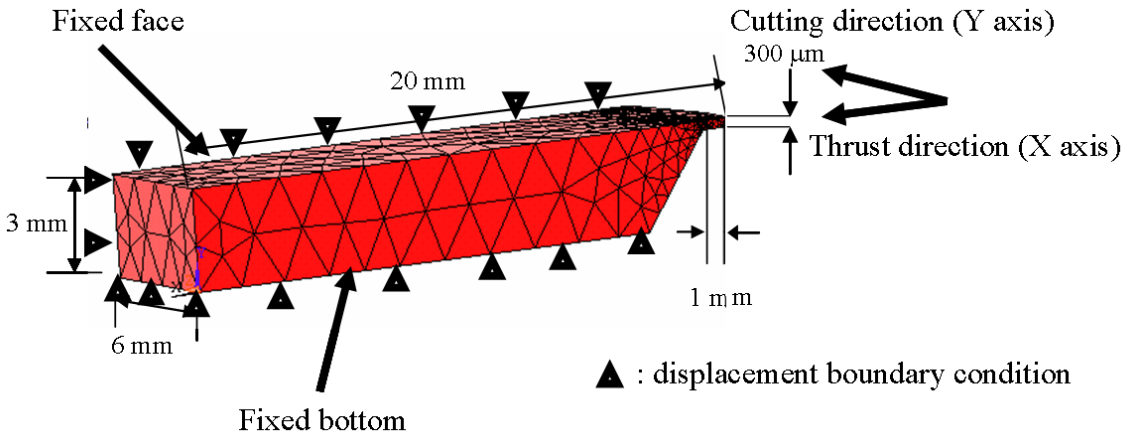

Figure 4.8: Finite element model of the tool

tool was taken to be 600 GPa. The model is shown in Fig. 4.8. All six degrees of freedom at nodes on the tool base and the face of the tool in contact with the tool holder were constrained. Note that the tool is mounted in the tool holder (secured by set screws) and these faces are in complete contact with the tool holder (not modeled). The applied cutting forces are uniformly distributed on the tool edge.

It is evident from Fig. 4.9 that the static tool deflection in the X (depth of cut) direction is negligible. The maximum deflection in the X direction is 0.1 μm for the extreme case representing the resultant of the maximum cutting and thrust forces. This indicates that, in the current experimental setup, tool deflection has a negligible effect on the depth of cut.

4.2.2.3 Tool thermal expansion

The tool thermal expansion was analyzed using a combination of an analytical thermal model and finite element simulation. Specifically, the temperature distribution derived from the analytical thermal model was used in the ANSYS ® finite element software to estimate the tool thermal expansion. The analytically determined 3-D transient temperature rise in the workpiece is based on the following solution of a

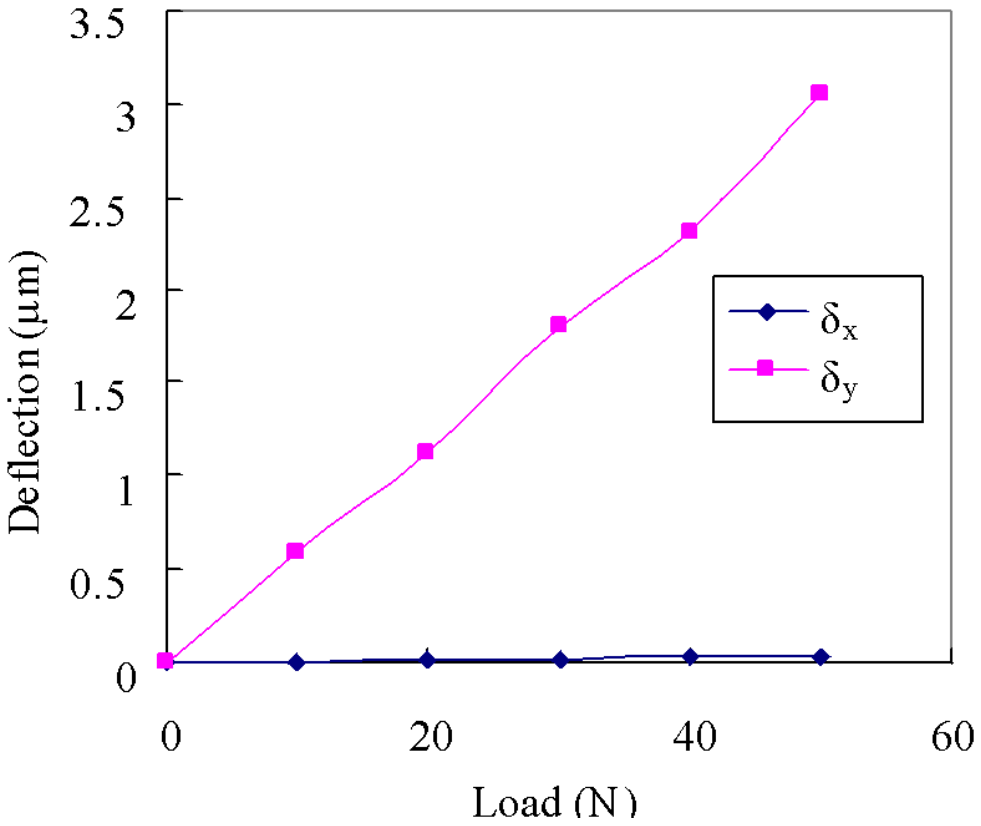

Figure 4.9: Load deflection curve for 300 μm wide grooving tool

moving disk shaped Gaussian heat source acting on a semi-infinite body with coordinates aligned with the laser beam center [91, 92]:

$$\theta_M = \frac{9qv}{4\lambda a\pi^{3/2}r_0^2} e^{-XV} \int_0^{r_0} e^{-(3r_i/r_0)^2} r_i dr_i \int_0^{\omega} \frac{e^{-\omega-\frac{u^2}{4\omega}}}{\omega^{3/2}} d\omega \times I_0 \left[\frac{r_i V^2}{2\omega} \sqrt{\left(x + \frac{2\omega}{V}\right)^2 + y^2} \right] \tag{4.1}$$

where, q = laser power, a = thermal diffusivity of the medium, λ = thermal conductivity, r_0 = beam radius of the laser, v = scan velocity, $V{=}v/2a$, r_i = instantaneous radius (varies from 0 to r_0), $\omega = v^2\ \tau/4a$ for transient; for quasi-steady state $t{=}5$ and I_0 = Modified Bessel function of the first kind of order zero and time step for ω used in integration is 0.005 sec. Note that the heat generated due to cutting induced deformation is ignored because it is very small compared to the heat generated by laser heating.

The tool thermal expansion analysis also assumes that the heat conducted to the tool is small compared to the portion conducted into the workpiece. In order to verify this assumption, a finite element analysis of the tool in perfect contact with the workpiece under static condition was conducted to determine the fraction of heat transferred from the workpiece to the tool. Employing half symmetry, the tool was modeled as a 150 μm wide solid, 1 mm in length and 3 mm in height using solid brick 8-noded elements (Solid 70). The workpiece dimensions were scaled down to 5 mm x 2 mm x 2 mm. The spot size of the laser beam was 70 μm (semi-circular region of laser spot is modeled due to half symmetry) and the laser power was 10 W. The vector sum of the heat flux in the workpiece and tool is shown in Fig. 4.10. The distribution reveals that less than 10% of the heat is conducted into the tool while more than 90% remains in the workpiece. Consequently, the earlier assumption ignoring heat transfer to the tool is considered to be valid for the conditions investigated in this work and the solution of Eq. 4.1 can be used to analyze the tool thermal expansion.

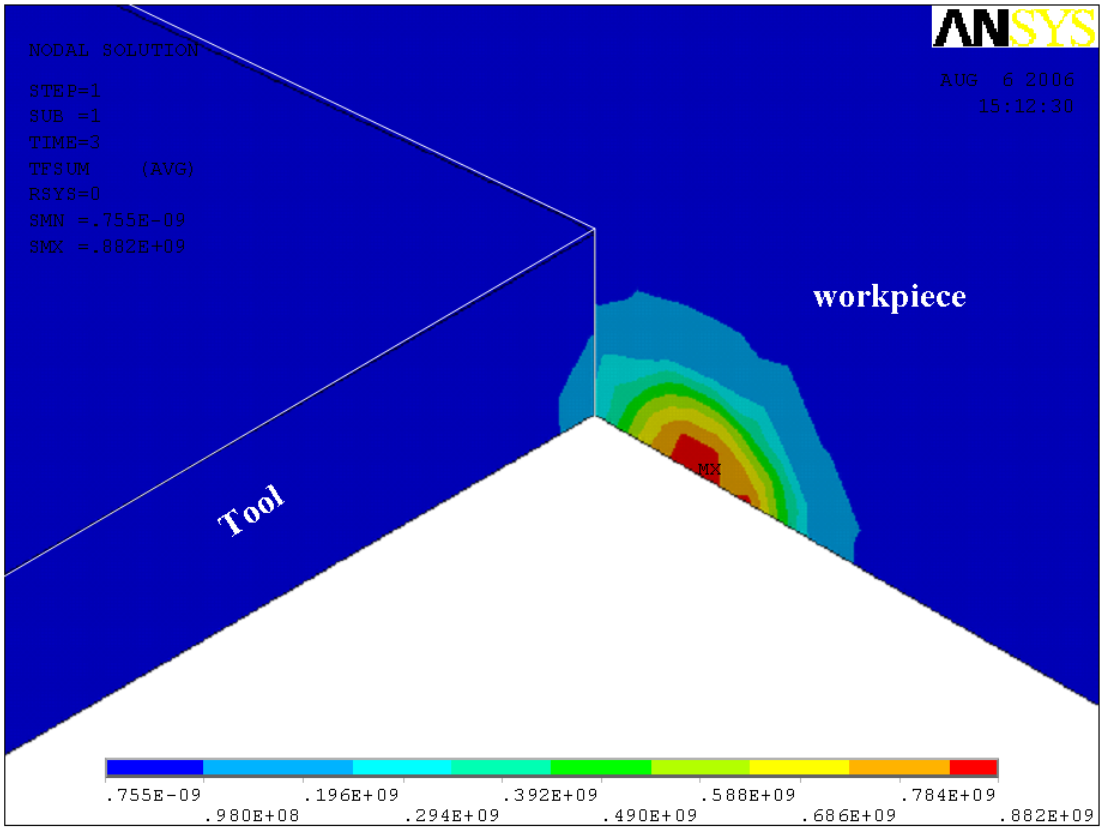

Figure 4.10: Distribution of the vector sum of heat flux in the workpiece and the tool

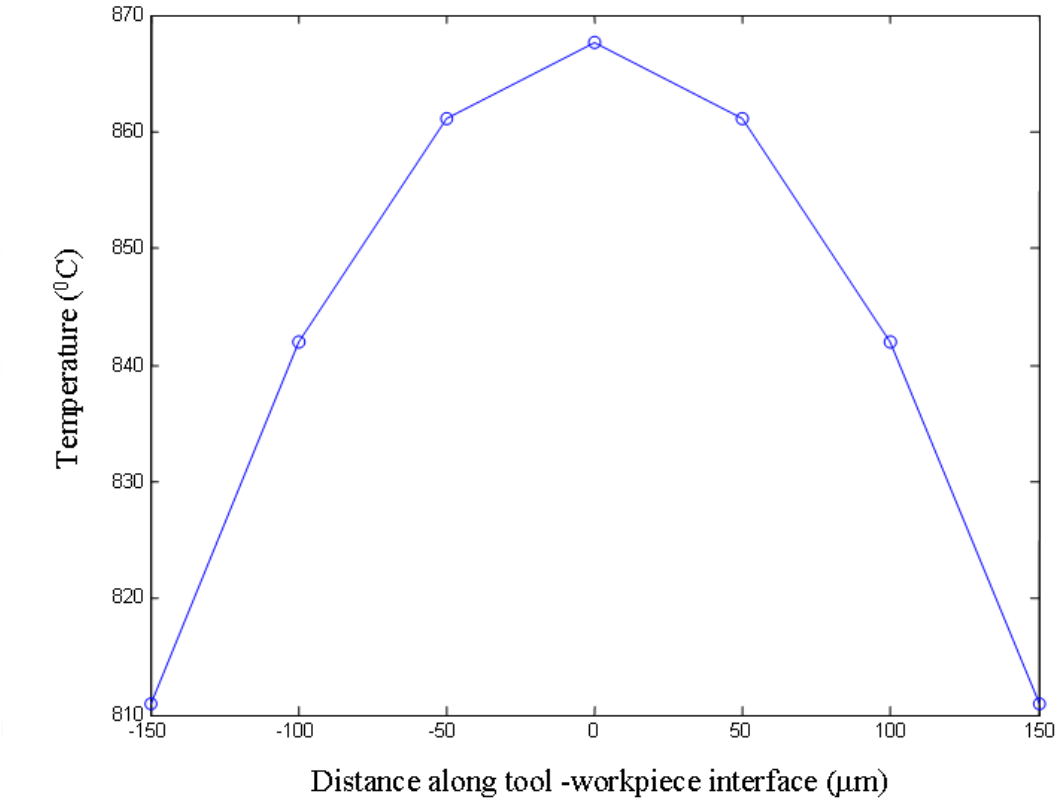

Figure 4.11: Temperature rise at the tool-workpiece interface at 10 μm depth of cut, 10 mm/min cutting speed, 10 W laser beam with 70 μm spot size located at 100 μm from the laser beam center

Fig. 4.11 shows the distribution of temperature rise in the workpiece after 1 minute at 10 μm below the surface for 10 mm/min laser speed, 10 W laser beam and 70 μm spot size located 100 μm from the laser beam center calculated using of Eq. 4.1. It can be seen from Fig. 4.11 that the temperature rise varies from 868°C at the center of the irradiated spot to 810°C at the tool edge. The workpiece temperature profile at the tool edge location obtained from this distribution is superimposed onto the tool edge for thermal expansion analysis. Based on thermal equilibrium considerations, it is reasonable to assume that the tool and workpiece temperatures at the interface are identical. Note however that in reality the tool-workpiece contact occurs over a finite area and therefore superposing the workpiece temperatures only on the tool edge may underestimate tool thermal expansion, particularly at large depths of cut. Also the predictions from Eq. 4.1 have not been validated at the tool-chip interface. A more precise thermal model with validations is presented in the next chapter.

Fig. 4.12 shows a portion of the actual tool modeled in ANSYS. The circled portion is the tool overhang, which is in contact with the workpiece during cutting. The remaining portion fits into the slot of the tool holder. Since the thermal mass of the remainder of the tool and the tool holder are significantly higher than that of the tool overhang portion, the temperature observed at the end of the tool overhang is close to ambient. The tool was modeled as a 300 μm wide solid, 1 mm in length and 3 mm in height, using solid brick 8-noded elements (Solid 70). The thermal conductivity of the tool material was taken to be 42 W/m.K (to account for TiAlN coating that acts as a thermal barrier), the specific heat was assumed to be 200 J/Kg.K and the coefficient of thermal expansion was 6.5 x 10-6/℃. Convection boundary conditions (h = 5 W/m^2.K, estimated for natural convection on a heated plate) were applied on all the tool surfaces, while at the end of the overhang (1 mm from the edge of the tool, as shown in Fig. 4.12) the ambient temperature boundary condition was applied. All displacement degrees of freedom at the end face of the tool (shown in Fig. 4.13)

were restricted in the subsequent mechanical analysis to determine the magnitude of thermal expansion.

Fig. 4.13 shows the top view of the tool overhang after model solution. It reveals that the maximum tool thermal expansion can be as high as 2.2 μm in the extreme case (at the center of the tool),which represents 22% of the 10 μm depth of cut. The workpiece thermal expansion based on a linear coefficient of thermal expansion of 13.1 X 10-6/° is about 0.05 μm, which is considered negligible in this work.

4.2.3 Measurement of Groove Depth

A white light interferometer image of the cut groove geometry is shown in Fig. 4.14. The difference between the perpendicular trace of the groove (shown by the double-headed arrow in Fig. 4.14) for the machining pass (with/without laser heating) and the preceding clean-up pass gives the actual depth of cut. Note that clean-up cuts are required for removing the laser marks made during the laser spot alignment process.

Fig. 4.15 shows the profiles of the cut grooves at 10 W laser power, 10 mm/min cutting speed and laser beam center located at 100 μm from the tool edge. The upper trace in each graph of Fig. 4.15 shows the groove profile created by the clean up cut used to remove the laser burn marks. This profile represents the initial condition and is marked "before machining" in Fig. 4.15. The subsequent lower trace represents the machined groove depth (the actual depth of cut is the difference between the two traces) and is labeled as "after machining" in the graphs.

Table 4.3: Nominal and measured depths of cut

Nominal depth of cut (μm)	Measured depth of cut (No laser) (μm)	Measured depth of cut (10 W laser)(μm)
10	7 ± 0.76	10 ± 1.01
15	10 ± 0.81	14 ± 0.87
20	12 ± 1.15	19 ± 1.86
25	18 ± 0.99	22 ± 1.23

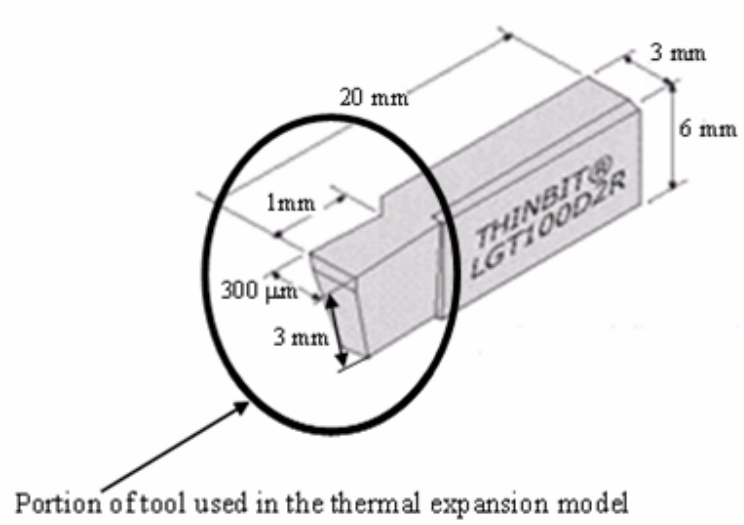

Figure 4.12: Tool geometry used in thermal modeling

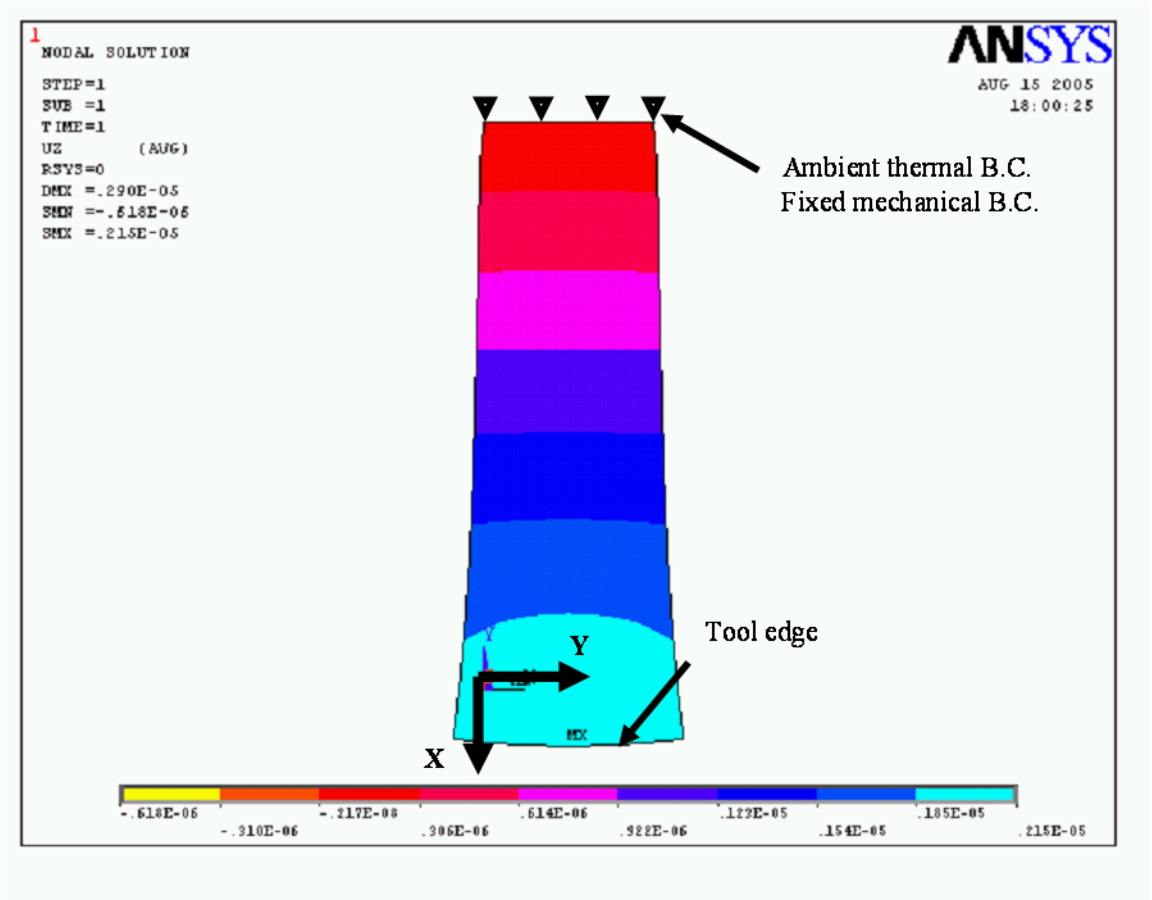

Figure 4.13: Thermal expansion of tool solved in ANSYS ®

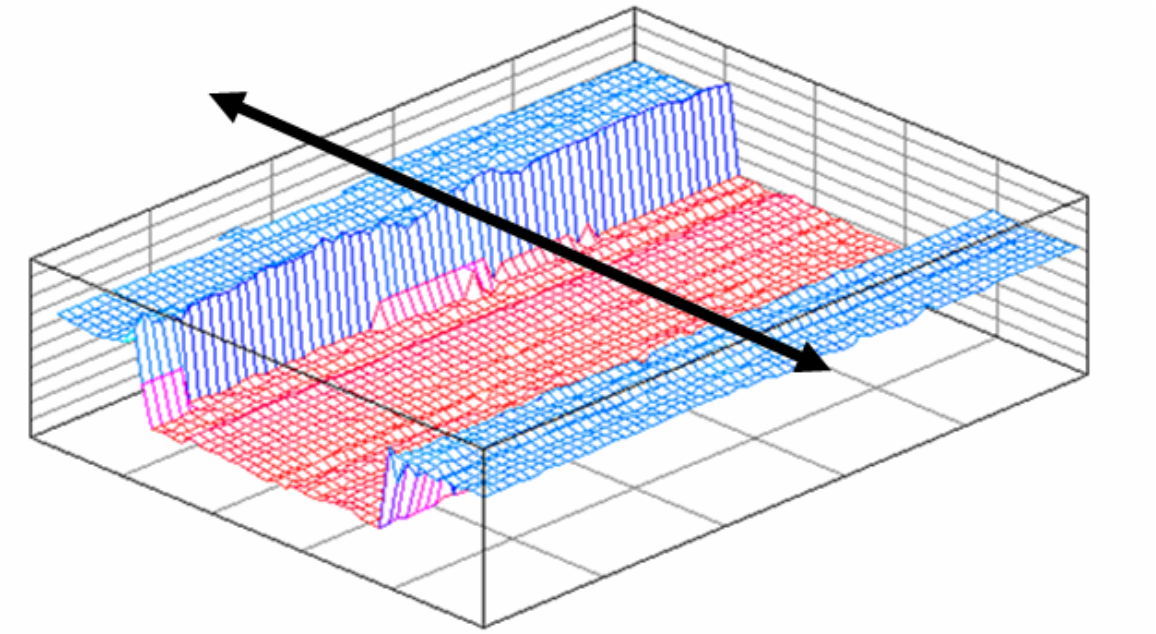

Figure 4.14: 3-D plot of a typical micro groove (10 W laser power, laser spot location: 100 μm from the tool, 10 μm nominal depth of cut, 10 mm/min cutting speed)

It can be seen that, for different nominal depths of cut with and without laser heating, the dimensional accuracy of the groove depth increases appreciably with laser heating. Table 4.3 lists the nominal and measured values of the mean depth of cut with and without laser heating and their standard deviation. A 30% difference between the nominal and measured depths of cut is observed for a 10 μm nominal depth of cut. A 28% difference is observed between the nominal and measured depths of cut for 25 μm nominal depth of cut. In the presence of laser heating, negligible difference is observed between the nominal and measured depths of cut for a nominal depth of cut of 10 μm while the difference is reduced to 12% for a nominal depth of cut of 25 μm.

It is evident from Table 4.3 and Fig. 4.15 that higher actual depths of cut are observed with laser heating compared to without laser heating, which, as noted earlier, can be attributed to reduced stage deflection (due to lower thrust forces arising from

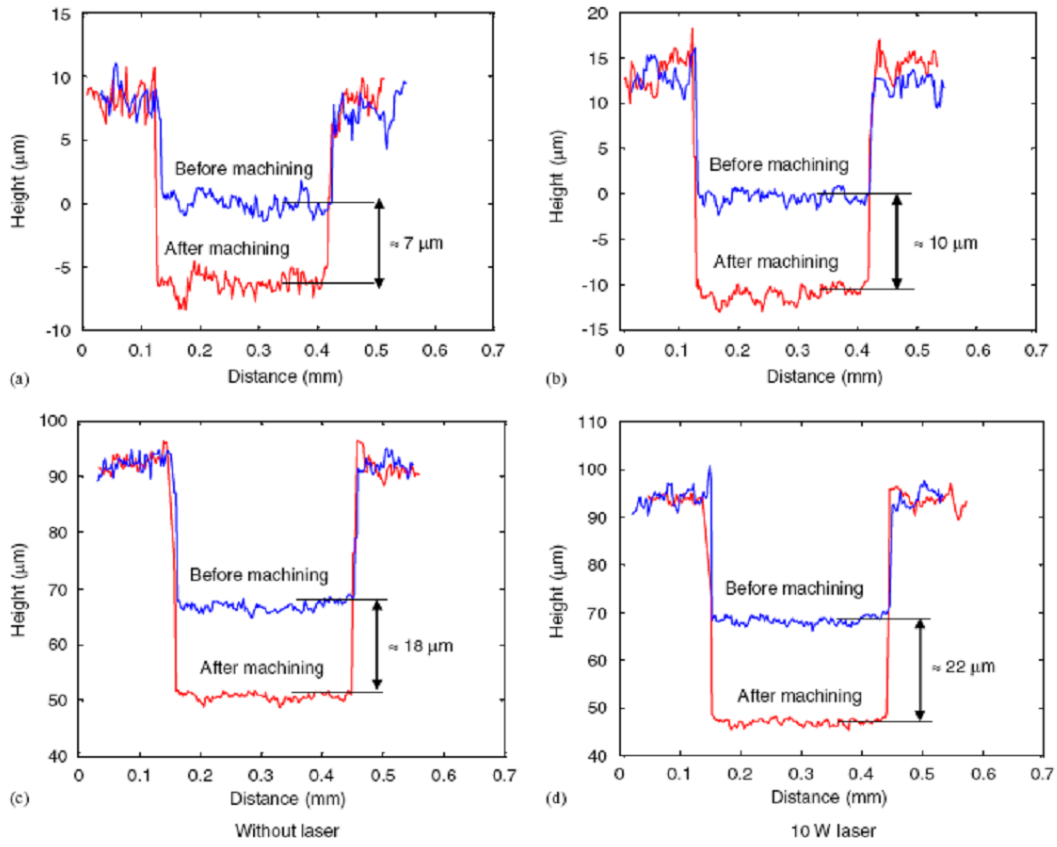

Figure 4.15: Measured depth of groove machined at 10 μm nominal depth of cut (a) without laser heating, (b) with the laser heating; 25 μm nominal depth of cut (c) without laser heating, (d) with laser heating

thermal softening) and tool thermal expansion. As a result, the measured depths of cut with 10 W laser power are closer to the nominal depths of cut than those obtained without laser heating.

4.3 Effect of Laser Variables and Cutting Parameters on Surface Roughness

Three dimensional surface roughness data was acquired by a white light interferometer based instrument (Zygo NewView 200). Fig. 4.16 shows a sample surface plot of the measured surface of the groove bottom.

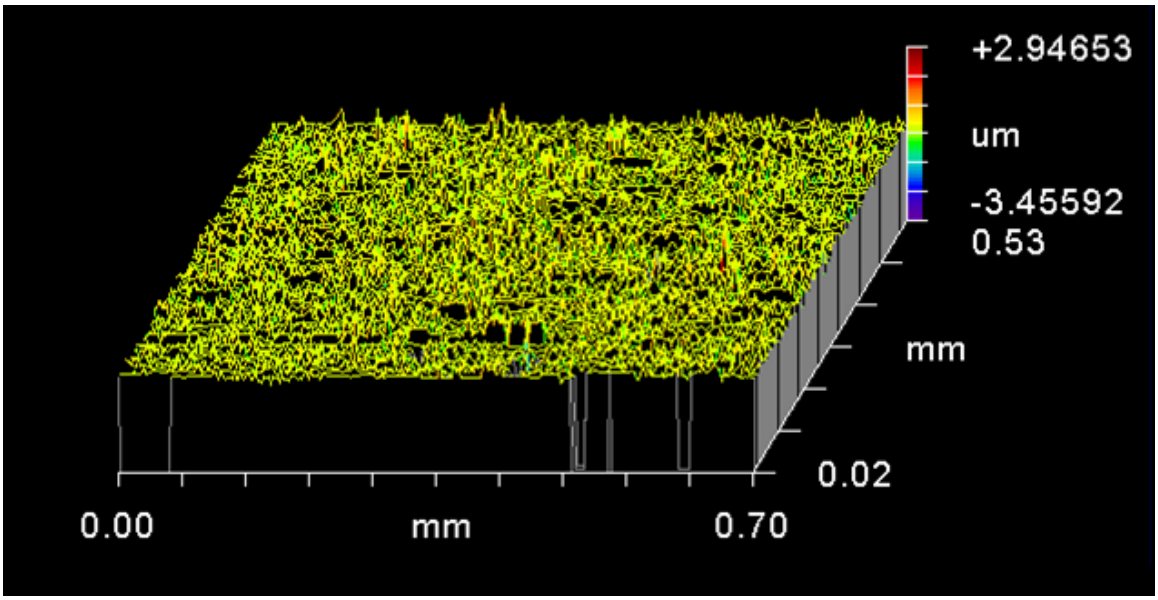

Figure 4.16: 3-D surface plot of LAMM surface

To investigate the effects of the main factors and their interaction on the surface roughness, a full factorial design of experiments was conducted. The ANOVA performed on the surface roughness data showed that the main effect of laser power and depth of cut were statistically significant at an α level of 5%. The two-way interaction effects of width of cut and laser location, depth of cut and laser location and depth of cut and laser power were found to be statistically significant at an α level of 5%.

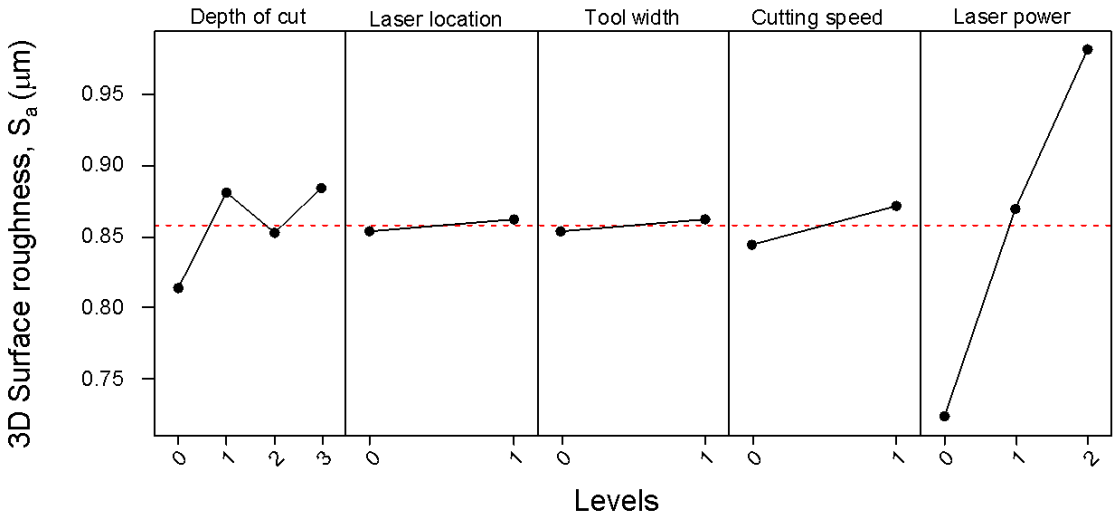

Figure 4.17: Main effect plot for 3-D average surface roughness, S_a

Fig. 4.17 shows the main effects plot for the 3-D average surface roughness parameter, S_a. The surface roughness is lowest for 10 μm depth of cut while an increase of 7.3% is observed when the depth of cut is increased to 15 μm. The surface roughness exhibits no discernable pattern as a function of the depth of cut. The surface roughness decreases if the depth of cut is increased to 20 μm and increases again by 4% when the depth of cut is increased to 25 μm. An increase of 36% is observed when the laser power is increased from 0 to 10 W. It has been observed that burr formation increases with laser heating in laser assisted micro milling [95], and in laser cutting of mild steel [96] the surface roughness deteriorates with increase in laser power. The surface roughness results in the present work appear to be consistent with the trends reported in these prior studies.

4.4 Summary

This chapter described a detailed experimental characterization of the LAMM process. The process attempts to overcome the limitations of low tool stiffness and bending strength in pure mechanical micro cutting and the geometry limitations of pure laser

micromachining. The study revealed that machine stiffness and thermal expansion of the tool can affect the actual depth of cut in LAMM-based micro-grooving process. The following specific conclusions can be drawn from the experimental study presented in the current chapter:

- The main effects of depth of cut, width of cut and laser power on the cutting force are statistically significant at a risk level (α) of 5%. The two-way interaction effects of depth of cut and laser power, depth of cut and tool width, tool width and laser power, cutting speed and laser power, and laser location and cutting speed on the cutting force are also statistically significant.

- The main effects of depth of cut, width of cut, cutting speed, laser location and laser power are statistically significant on thrust force at a risk level (α) of 5%. All two-way interaction effects except the depth of cut and cutting speed, and laser location and laser power, are statistically significant on thrust force.

- Thermal softening can be induced by laser heating and up to 56% and 46% reduction in the cutting and thrust forces, respectively is observed at 35 W laser heating.

- Decrease in the cutting force with laser heating is not always observed because of an increase in the actual depth of cut due to smaller stage deflection (as a result of lower thrust forces) and thermal expansion of the tool at low laser powers ($\leq$ 10 W).

- Laser induced thermal softening improves the accuracy of the groove depth by reducing the stage deflection (due to lower thrust force).

- The main effect of laser power and depth of cut are statistically significant on surface roughness at a risk level (α) of 5%. The two-way interaction effects of

width of cut and laser location, depth of cut and laser location and depth of cut and laser power are statistically significant on surface roughness.

- Laser power appears to significantly affect the surface roughness in the LAMM process; an increase of up to 36% is observed in the current study.

The experimental study shows the effects of laser heating on thermal softening and improvement in dimensional accuracy but since it is a thermally-assisted process it can induce undesirable microstructural changes in the residual surface. The following chapter is focused on characterization and prediction of the heat affected zone (HAZ) to ensure desired softening without inducing any detrimental HAZ.

CHAPTER V

CHARACTERIZATION AND PREDICTION OF THE HEAT AFFECTED ZONE

Laser Assisted Mechanical Micromachining (LAMM) is a micro-cutting process that employs highly localized thermal softening of the material by continuous wave laser irradiation focused in front of a miniature cutting tool and has been described in detail in the previous chapters. Since it is a heat assisted process, it can induce a detrimental heat affected zone (HAZ) in the part. This chapter focuses on characterization and prediction of the HAZ produced in a LAMM-based micro-grooving process. The heat affected zone generated by laser heating of H-13 mold steel (42 HRC) at different laser scanning speeds is analyzed for changes in microstructure and microhardness. A 3-D transient finite element model for a moving Gaussian laser heat source is developed to predict the temperature distribution in the workpiece material. The thermal model predicts the temperature distribution in the vicinity of the laser beam, which is then correlated with the HAZ via microhardness tests. Based on this correlation analysis, the size of the HAZ and the critical temperature corresponding to formation of the HAZ in the material are determined. Using the model and the critical temperature, suitable laser and cutting parameters can be determined to achieve the desired amount of thermal softening with the smallest possible HAZ. To demonstrate this approach, an experimental result illustrating the use of the thermal model to limit the size of the HAZ to the volume of material removed in the LAMM based micro-grooving process is also presented.

5.1 Experimental Work

Prior to developing a thermal model to simulate the HAZ in LAMM-based micro-grooving, it is helpful to examine the impact of laser irradiation on the workpiece microstructure and its characteristics. Consequently, experiments were conducted to characterize the HAZ produced in pure laser heating of hardened H-13 steel (42 HRC) at different speeds. The test setup and procedures used in the experiments are described in the following subsections. The experimental setup (described in Chapter 3) minus the cutting tool is used to run laser scans on the surface of the H-13 steel workpiece of 85 mm x 50 mm x 50 mm size in order to study the resulting thermal damage in the workpiece.

5.1.1 Characterization of the HAZ

In order to examine the effect of laser heating on the HAZ, experiments were conducted at 10 W laser power and three scanning speeds of 10, 50 and 100 mm/min. Note that in these tests only the laser is operational and no mechanical cutting is involved. The purpose of these tests is to determine the extent of the HAZ produced below the surface due to laser heating alone. It should also be noted that in general, the heat produced in plastic deformation associated with chip formation by the grooving tool is negligible compared to the heat generated by laser irradiation.

Fig. 5.1 shows optical images of the laser scanned H-13 workpiece surface at different speeds. The heat affected area is clearly visible in each image. It can be seen that the heat affected area is confined to smaller widths with increase in laser scanning speed. The widths of the visible heat affected areas in Fig. 5.1 are approximately 100 μm, 85 μm and 62 μm at 10, 50 and 100 mm/min scanning speeds, respectively. This is because faster the scan the less time there is for heat to be conducted into the workpiece and consequently it is restricted to a smaller region. Fig. 5.2 shows the 3-D surface topography of the laser scanned surface for 10 mm/min and 100 mm/min. It

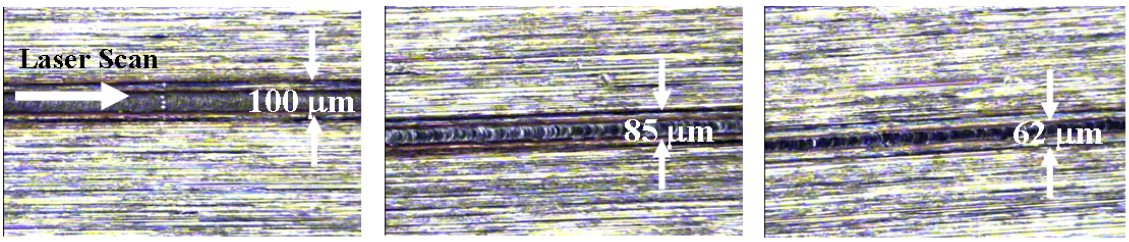

Figure 5.1: Surface of H-13 steel (42 HRC) exposed to laser scans (CW, 10W, 110 μm spot size) at 10, 50 and 100 mm/min scanning speeds

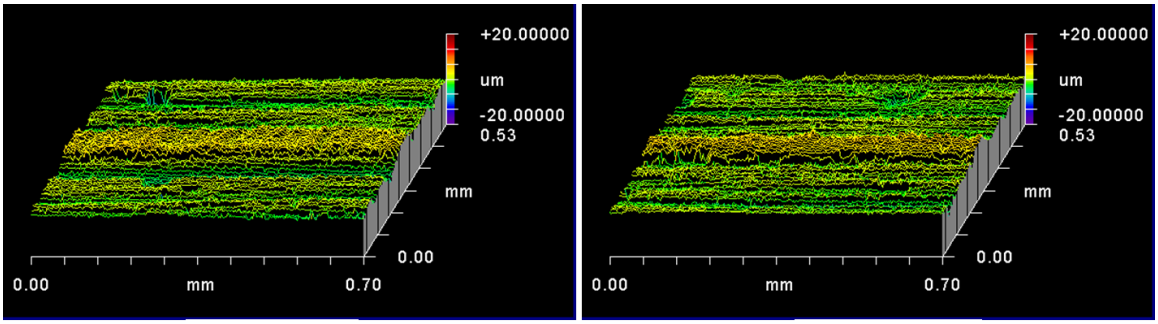

Figure 5.2: 3-D surface topography of H-13 steel (42 HRC) exposed to laser scans (CW, 10W, 110 μm spot size) at 10 and 100 mm/min scanning speeds

can be seen that there is no evidence of any material ablation.

Metallographic methods were used to examine the laser scanned surfaces in cross-sectional view. The samples were first cut from the workpiece using wire-EDM, molded in epoxy, polished using 240, 320 and 400 grit SiC paper and then with 9 μm, 3 μm and 1 μm diamond slurry. The samples were finally polished with 0.05 μm alumina suspension and etched using a 2% Nital solution. Fig. 5.3 shows the cross-sectional view of the laser scanned surface at 10 W laser power, 10 mm/min scan speed and 110 μm spot size. Fig. 5.3(b) (top) shows the presence of a remelted zone, which is a hard brittle layer formed by solidification of the molten metal pool. The remelted zone has an uneven surface due to fracture of the brittle layer during polishing. This causes the blur observed in the picture. Fig. 5.3(b) (bottom) shows the tempered martensitic bulk microstructure. The initial structure of the material is tempered martensite.

Although no sign of microstructure change is evident immediately below and around the laser scanned region of the workpiece in the optical micrograph of Fig. 5.3(a), the presence of a re-melted material on the surface suggests that some microstructure change must have occurred. To determine any microstructural changes in the material and to evaluate the extent of the HAZ, microhardness tests were conducted below the laser scan path on the polished cross-section of the sample. A contour map of the microhardness distribution was generated using a square measurement grid of 12.5 μm spacing. Fig. 5.4 shows a contour plot of the hardness variation for 10 W laser power and 10 mm/min scan speed. The change in hardness is clearly discernible in the micro-hardness contours. It can be seen that the maximum hardness observed is 54 HRC near the surface and it decreases with increase in depth. The hardness approaches the bulk hardness at about 50 μm below the surface.

The increase in hardness can be explained by the mechanism of laser hardening as follows. It involves the use of high intensity laser radiation, which rapidly heats the

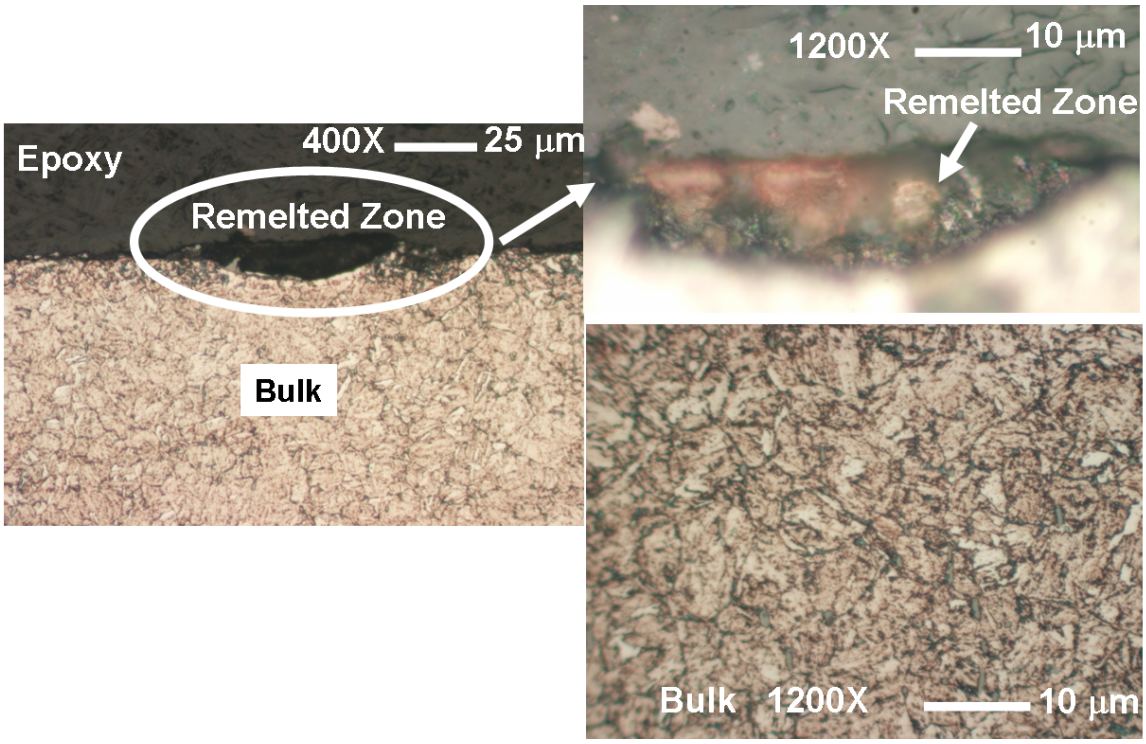

Figure 5.3: Micrographs of laser scanned H-13 samples (CW, 10 W, 110 μm spot size and 10 mm/min scanning speed): (a) Cross-section of the bulk and re-melted zone at 400X magnification, (b) Magnified (1200X) view of the re-melted zone (top) and bulk microstructure (bottom)

steel surface into the austenitic region described by the critical temperatures Ac_1 and Ac_3. For H-13 steel, austenitization starts when the temperature reaches the 840°C (Ac_1) and is complete when it reaches 890°C (Ac_3) the austenitization. The very steep temperature gradients result in rapid cooling by conduction of heat from the surface to the bulk. This causes transformation from austenite to martensite without external quenching. The self-quenching occurs as the low temperature of the bulk provides a sufficiently large heat sink to quench the hot surface by heat conduction to the interior at a rate high enough to prevent pearlite or bainite formation at the surface, resulting in untempered martensite formation instead [97].

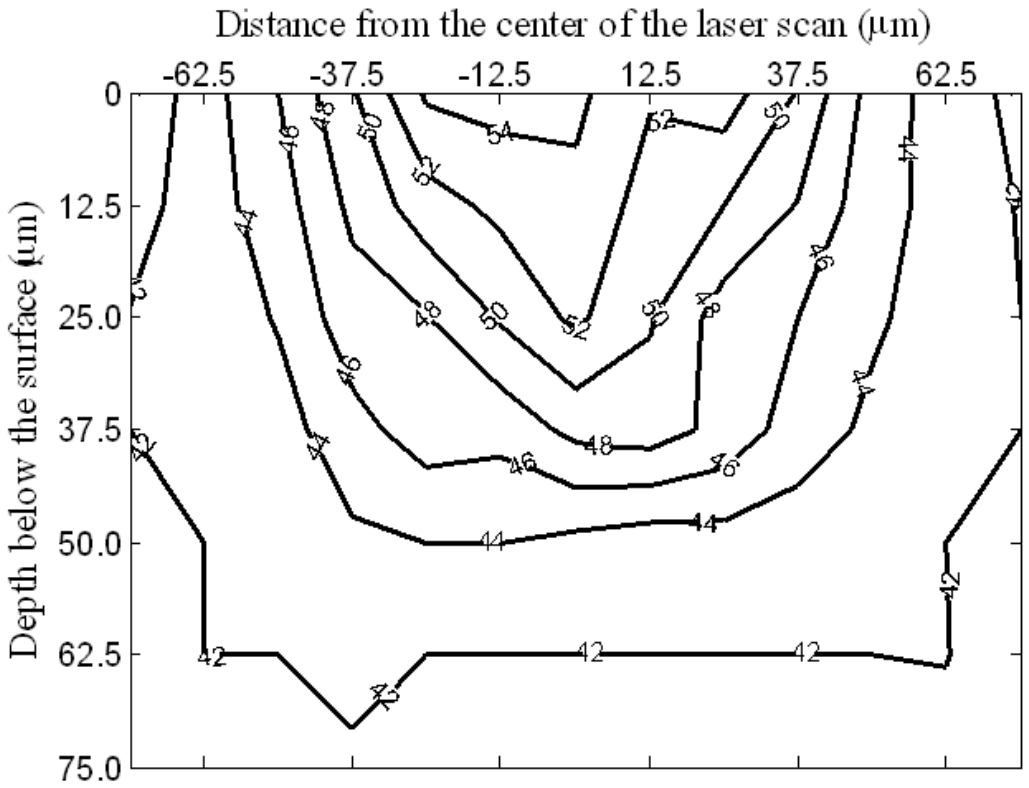

Figure 5.4: Hardness contours (HRC) in the cross-sectioned H-13 steel sample (10 W laser power and 10 mm/min scan speed)

Although the depth at which the hardness value approaches the base material

hardness is representative of the depth of the HAZ, confirmation of this fact can be obtained by examining the correlation between the temperature distribution in the workpiece and the hardness contours shown in Fig. 5.4. The temperature distribution in the workpiece produced by laser irradiation can be determined from the thermal analysis of a moving Gaussian heat source incident on the workpiece surface. The model and solution approach underlying this analysis are discussed in the following section.

5.2 Thermal Modeling

5.2.1 Physical and Mathematical Description of the Model

The thermal model for determining the temperature distribution in the workpiece due to laser heating is based on a 3-D transient heat conduction analysis of a moving Gaussian heat source applied to the workpiece surface. The model is solved using the finite element method and makes use of certain key assumptions, equations, and modeling procedures that are summarized below.

1. Heat generated due to energy dissipated in plastic deformation during chip formation is assumed to be small compared to the heat generated by laser irradiation.

2. A scaled model of dimensions 5mm x 2mm x 2mm is used to reduce the problem size, which ensures faster solution times.

3. The Gaussian distribution of laser power intensity $P_{x,y}$ at location (x, y) (shown in Fig. 5.5) is given by:

$$P_{x,y} = \frac{2P_{tot}}{\pi r_b^2} e^{-\frac{2r^2}{r_b^2}} \tag{5.1}$$

where $r = \sqrt{x^2 + y^2}$ is the distance from the laser beam center and r_b is the laser beam radius; $P_{tot} = \eta\ P_{incident}$, where P_{tot} is the total absorbed power,

$P_{incident}$ is the incident laser power, and η is the average absorptivity of the workpiece material.

4. The average absorptivity, η, of the workpiece material is determined by calibrating the model against a measured temperature at a known workpiece location for given power and speed combinations.

5. All workpiece physical properties are considered to be temperature dependent. The thermal conductivity is assumed to be isotropic. The temperature-dependent thermophysical properties are given in Table 5.1 and Table 5.2. Note that the specific heat data is estimated from alloy steel (Fe + Cr + $\sum X_i$) data derived from Touloukian et al. [98] and the ASM Ready Reference [99].

6. When temperature at a node exceeds the melting point, the node remains in the mesh and the latent heat of fusion is simulated by an artificial increase in the liquid specific heat as given by Brown et al. [100] and Frewin et al. [101].

Table 5.1: Thermal conductivity of H-13 steel

Temperature (℃)	Thermal conductivity (W/m ℃)
27	17.6
204	23.4
427	25.1
649	26.8
787	29.6

The three-dimensional transient heat conduction equation for the problem is given by,

$$\frac{\partial}{\partial x}\left(k\frac{\partial T}{\partial x}\right)+\frac{\partial}{\partial y}\left(k\frac{\partial T}{\partial y}\right)+\frac{\partial}{\partial z}\left(k\frac{\partial T}{\partial z}\right)+\dot{Q}=\rho C_p\frac{\partial T}{\partial t}+\rho C_p V_x\frac{\partial T}{\partial x} \tag{5.2}$$

where ρ, C_p, k, $\dot{Q}$ and V_x are the density, specific heat, thermal conductivity, rate of volumetric heat generation and laser scan speed, respectively.

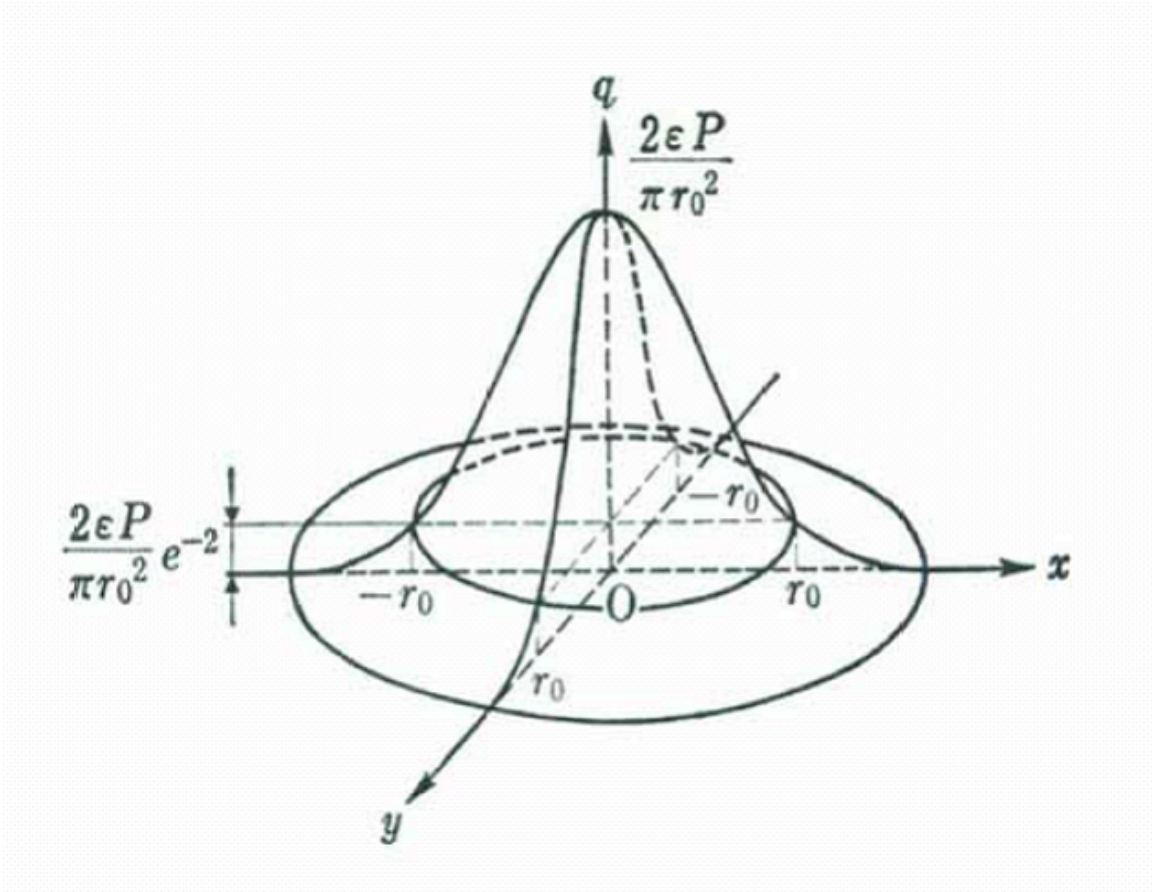

Figure 5.5: Gaussian distribution

The initial condition at time $t=0$ is given as,

$$T(x, y, z, 0) = T_0 \tag{5.3}$$

The natural boundary condition takes into account the imposed heat flux, radiation and convection at the laser irradiated surface and is given by,

$$k\frac{\partial T}{\partial n} - q + h\left(T - T_0\right) + \sigma\epsilon\left(T^4 - T_0^4\right) \tag{5.4}$$

where h = convective heat transfer coefficient, σ = Stefan-Boltzmann constant = $5.67 \times 10^{-8} Wm^{-2}K^{-4}$ and ϵ = emissivity. Note that the temperature dependent emissivity for H-13 steel has been determined by Gogol et al. [102].

The inclusion of temperature-dependent thermophysical properties and a radiation term in Eq. 5.4 makes the analysis highly nonlinear. To avoid this, one can use the following lumped convection coefficient that accounts for radiation as suggested by Ferwin et al. [101].

$$h = 2.4 \times 10^{-3}\epsilon T^{1.61} \tag{5.5}$$

Previous studies [101, 103] have shown only a 5% change in the calculated temperatures with and without the radiation term in Eq. 5.4. Consequently, the current work uses the lumped convection coefficient to model the combined convection and radiation heat losses.

The boundary conditions at the remaining surfaces in the model mimic the actual block. Since only a small portion of the actual block is modeled, the heat flux on the model surfaces should be approximately equal to the heat conducted from the smaller portion of the block into the bulk. Experiments were conducted on a small block having the model dimensions stated earlier and temperatures were measured at the side and top surfaces using thermocouples. The average temperatures measured on these surfaces are used as boundary conditions in the model. Since the finite

element model employs half symmetry, the heat flux at the bottom face is set to zero. The initial workpiece temperature is set to 25℃.

5.2.2 Finite Element Model

The finite element model is created in ANSYS ® ver. 10 based on the physical and mathematical description of the problem given above and is shown in Fig. 5.6. Note that a very finely mapped mesh is used in the area where the Gaussian laser heat flux is incident. This is to capture the steep temperature gradient as accurately as possible. The size of the mapped element is 25 μm along the X-axis (length), 12.5 μm along the Y-axis (height) and 20 μm along the Z-axis (depth). The mapped mesh portion is 5 mm x 200 μm x 200 μm. An eight noded 3-D thermal element (Solid70) is used. The model contains 48,610 nodes and 107,288 elements.

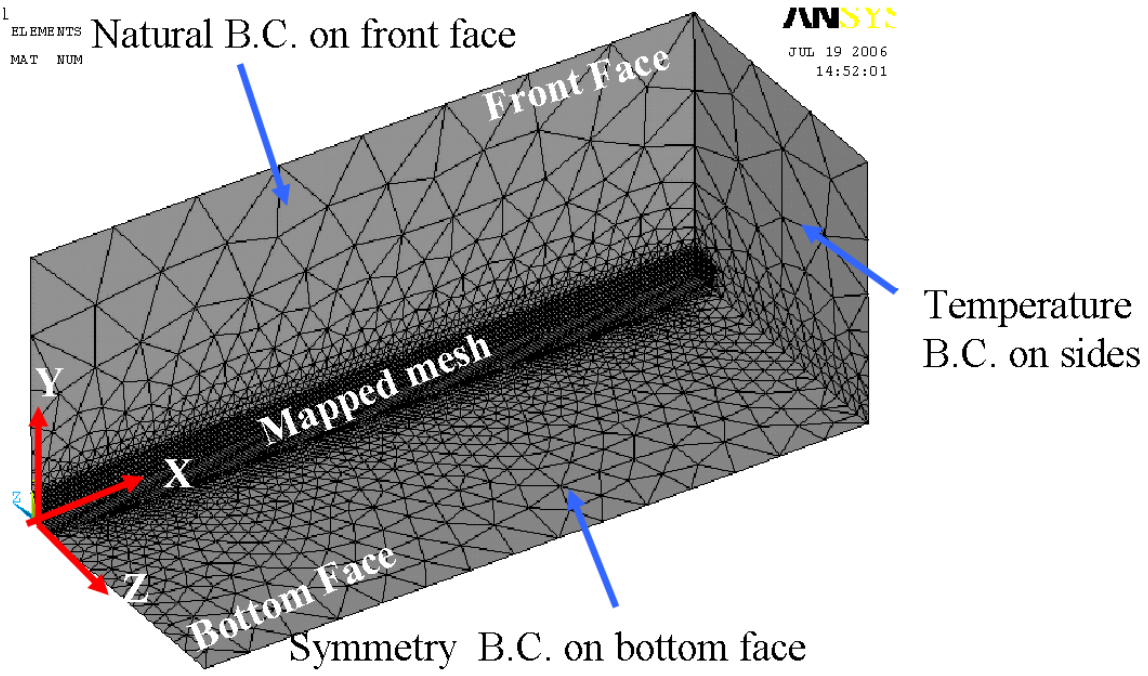

Figure 5.6: Finite element mesh of workpiece

The moving laser heat source is symmetric and hence the semi-circular Gaussian distribution of heat flux is defined by a matrix of 5 × 5 elements and the total area

of heat flux application is $100\mu m \times 50\mu m$. The heat flux table is computed using Eq. 5.1 and is made to sweep the mesh on the front face of the block to simulate the moving heat source. The heat transfer coefficient on the front face is implemented by approximating a polynomial fit to the function given in Eq. 5.5. The value of $h$varies from $5W/m^2K$ at 25°C to 300 W/m^2K at 1900°C. The variation of h is shown in Fig. 5.7.

As explained in the previous section, a temperature boundary condition is used on the remaining faces. The heat flux matrix is moved for a distance of 3 mm, which comprises of 121 load steps. The heat transfer equation is solved at each step till the solution converges. It was observed that the solution stabilizes after about 41 steps. The laser scan speed is realized by specifying the time interval for the total number of load steps. The time increment during one load step can also be specified and is an order of magnitude lower than the load step time interval.

A contour plot of the temperature distribution on the front face of the block is shown in Fig. 5.8 for the case of 10 W laser power and 10 mm/min laser scan speed. The maximum temperature for the case shown is 1876°C and the temperature at a distance of 200 μm from the center of the laser beam along the Y-axis is about 363°C. This indicates that the temperature distribution in the semi-circular region decays very rapidly. The temperature distribution for this low speed case appears to be symmetric about the Y-axis.

5.2.3 Model Validation

The model was validated by temperature measurements made using a K-type thermocouple of 75 μm diameter. The thermocouple was glued to the front face of the block using conducting cement (Omega Bond 400) and was calibrated using a temperature controlled furnace. The calibration chart is shown in Fig. 5.9. The thermocouple bead was always in contact with the metal surface as seen in Fig. 5.10. The laser

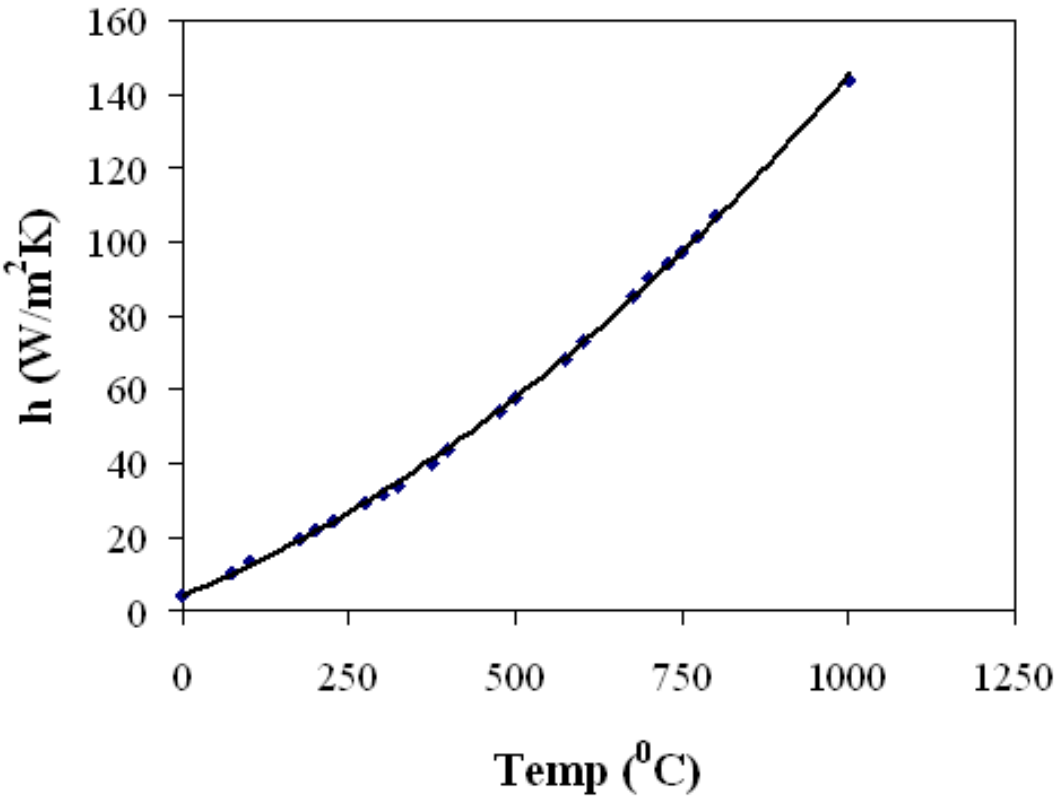

Figure 5.7: Variation of lumped convection coefficient, h, as a function of temperature

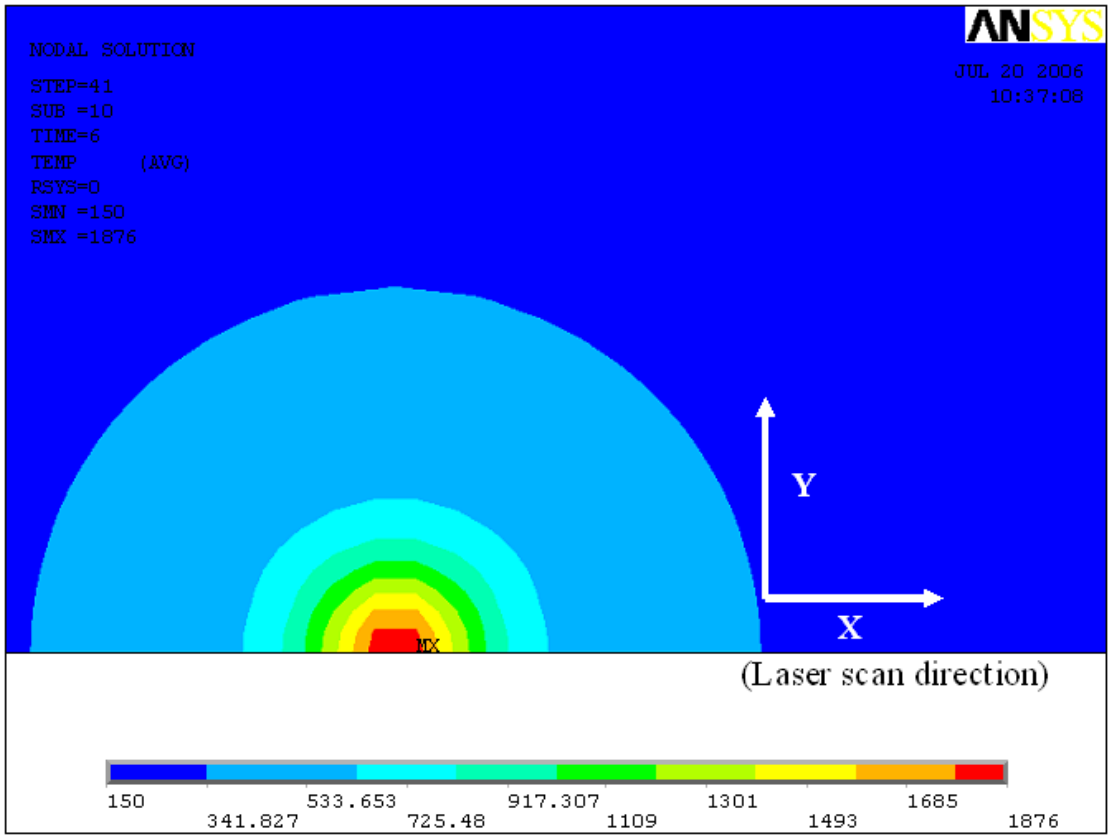

Figure 5.8: Simulated temperature distribution (10 W laser power, 10 mm/min scan speed and 110 μm spot size)

was scanned close to the thermocouple at a constant speed and the temperature recorded. The maximum temperature occurs when the laser beam center is closest to the thermocouple. The distance between the thermocouple and laser scan center was measured using a microscope camera (see Fig. 5.10).

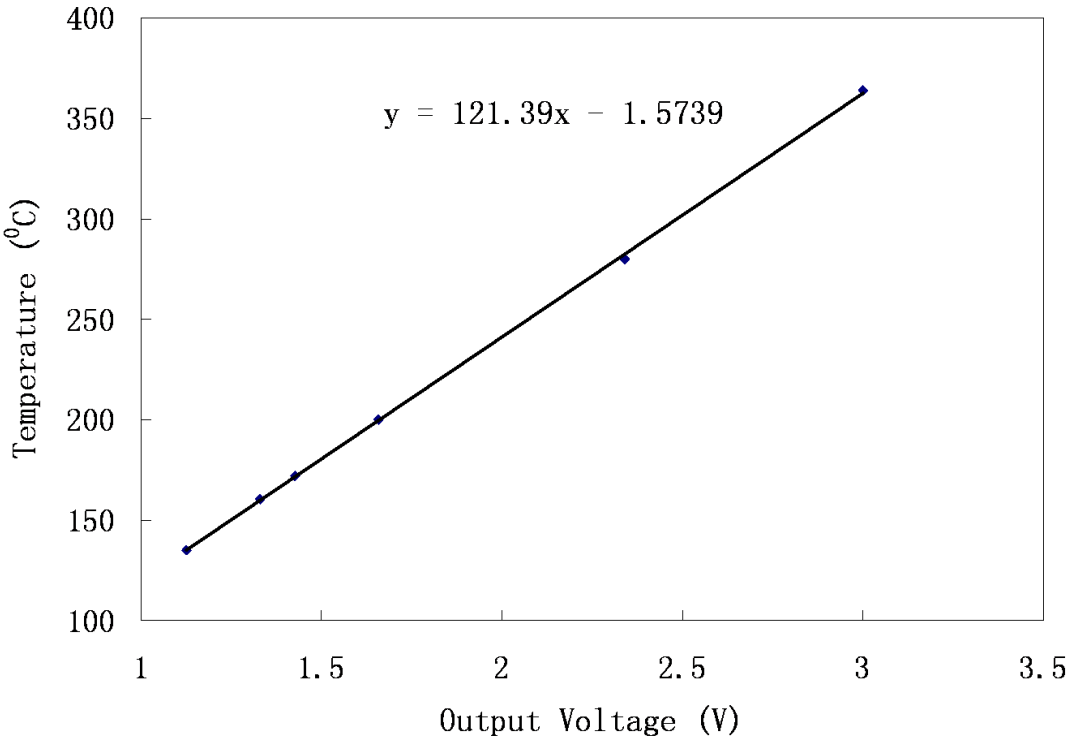

Figure 5.9: Calibration plot for thermocouple

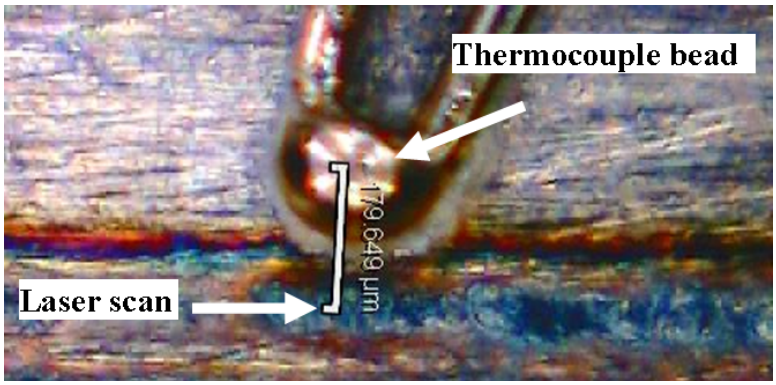

Figure 5.10: Location of thermocouple with respect to laser scan

The thermal model was calibrated by varying the absorptivity, η, till the model output matched the measured temperature at a point 250 μm from the laser beam center along the Y-axis. Absorptivity obtained in this manner was between 0.4-0.6 for the different cases examined. This is in agreement with values reported in the literature [104]. Once the absorptivity was determined, simulations were performed for three laser scanning speeds (10, 50 and 100 mm/min) and two laser powers (5 W and 10 W).

Fig. 5.11 and Fig. 5.12 show the predicted and measured temperatures as a function of the distance from the laser beam center at 5 W and 10 W laser powers, respectively. Six temperature readings were taken at each location of the thermocouple and the error bars in the figures represent one standard deviation of the measurements. The prediction error is $4-6\%$ at a distance of 20 μm from the laser beam center for a laser power of 5 W and between 5-15% when the thermocouple is between 100 and 200 μm from the laser beam center. At 10 W laser power, it can be seen that the model slightly under predicts the temperature close to the laser beam center. At 60 μm from the laser beam center, the errors are between 10-12% at all three speeds.

It is evident from the validation results that the predicted and measured temperatures are in fairly good agreement. The prediction errors may be attributed to the uncertainty associated with the exact location of the thermocouple, approximations in the temperature dependent thermophysical properties and the assumption of average temperature boundary conditions at the sides (excluding the front and bottom faces shown in Fig. 5.6. Next, the thermal model is used to analyze the temperature distribution below the surface and its correlation with the HAZ, which is characterized by the micro-hardness contours obtained earlier.

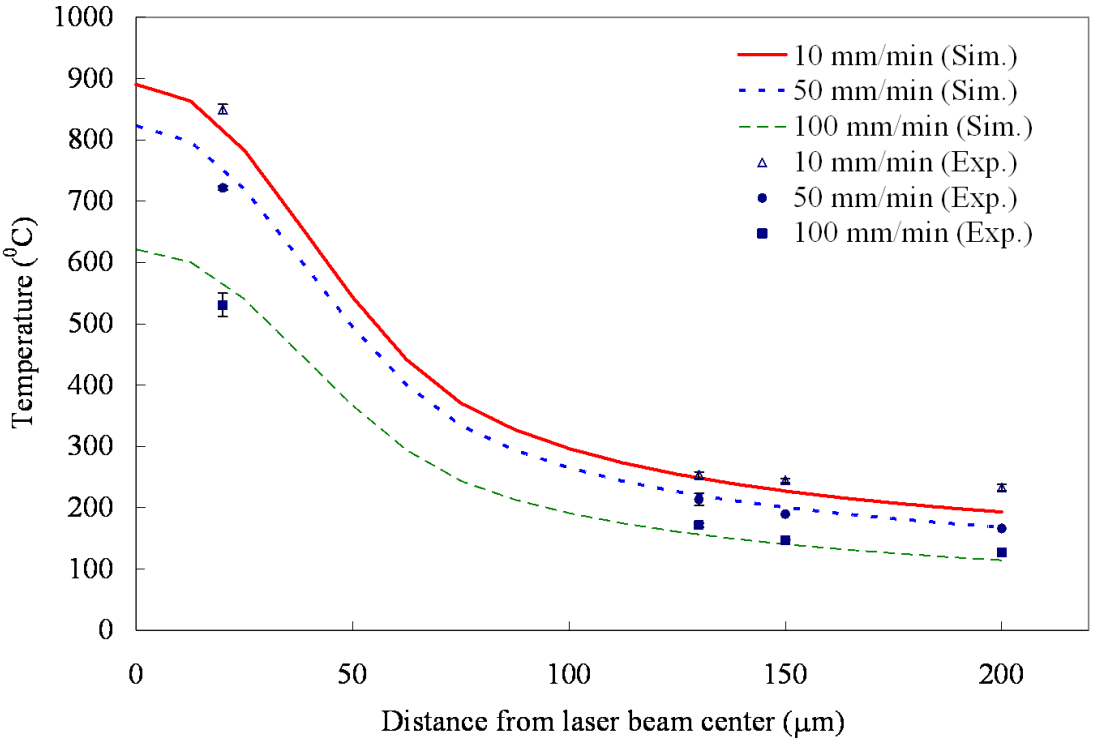

Figure 5.11: Simulation and experimental results for 5 W laser power

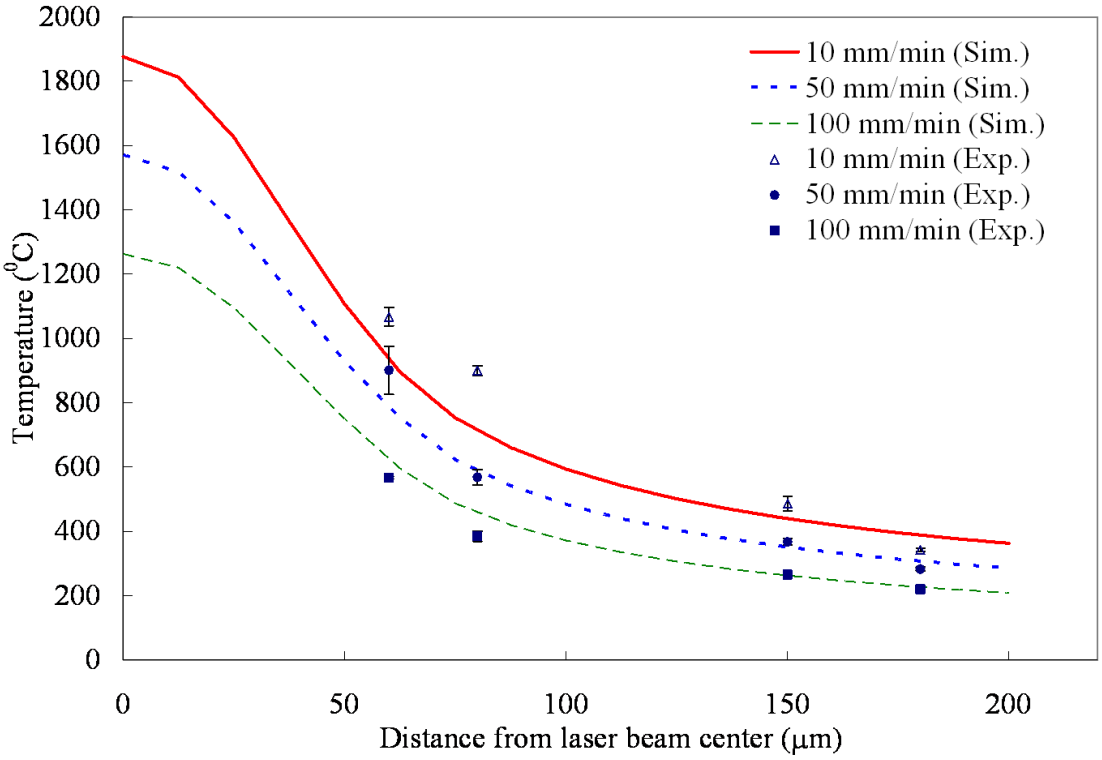

Figure 5.12: Simulation and experimental results for 10 W laser power

5.3 Results and Discussion

5.3.1 Correlation of Temperature Distribution with HAZ hardness

As described earlier, the mechanism of laser hardening depends on the temperature. Experiments show that the maximum depth of the HAZ depends on the laser scanning speed, which influences the resulting temperature distribution in the material. Fig. 5.13 and Fig. 5.14 show the temperature distribution and the hardness contours in the cross-section containing the HAZ for 10 W laser power and scan speeds of 10 and 50 mm/min, respectively. The horizontal axis in these plots represents the distance measured from the center of the laser scan and the vertical axis represents the depth below the surface. The units of the temperature contours in Fig. 5.13(a) are °C and the hardness contours in Fig. 5.13(b) are in HRC.

Fig. 5.13 shows that the hardness decreases from 54 HRC near the center of the laser scan to 43-44 HRC (transition hardness close to the bulk hardness) at a depth of approximately 50 μm (dashed line in Fig. 5.13) from the surface. The width of the HAZ is about 125 μm at the surface. The temperature corresponding to the transition hardness is close to Ac_1 for H-13 steel (840℃). Fig. 5.14 shows that if the speed is increased to 50 mm/min the hardness decreases from 52 HRC near the center of the laser scan to the transition hardness at a depth of about 35 μm (dashed line in Fig. 5.14) from the surface. The width of the HAZ in this case is about 110 μm at the surface. It is evident from Fig. 5.14 that the temperature corresponding to the transition hardness is close to Ac_1 for this case as well. This correspondence of the critical temperature to the transition hardness (and consequently the depth of the HAZ) can be explained by the mechanism of laser hardening discussed earlier. The initial microstructure of H-13 steel used in the current study is tempered martensite. As predicted by the thermal model, the temperature rise in the material can even exceed the melting point, which is corroborated by the presence of remelted zone near the surface as shown in Fig. 5.3. Austenitization starts in the portion of the

Table 5.2: Specific heat, density and emissivity of H-13 steel

Temperature (℃)	Density (kg/m^3)	Specific heat (J/Kg℃)	Emissivity
25	7850	460.26	0.2
100	7845	473.63	0.4
200	7816	487.01	0.45
300	7740	499.97	0.48
400	7733	513.34	0.51
500	7711	526.72	0.54
600	7669	540.09	0.56
700	7625	551.38	0.57
800	7578	566.43	0.58
900	7565	579.80	0.59
1000	7552	593.18	0.61
1100	7495	606.14	0.62
1200	7438	622.02	0.62
1300	7382	632.05	0.62
1400	7325	731.12	0.62
1500	7268	731.12	0.62
1600	7055	731.12	0.62

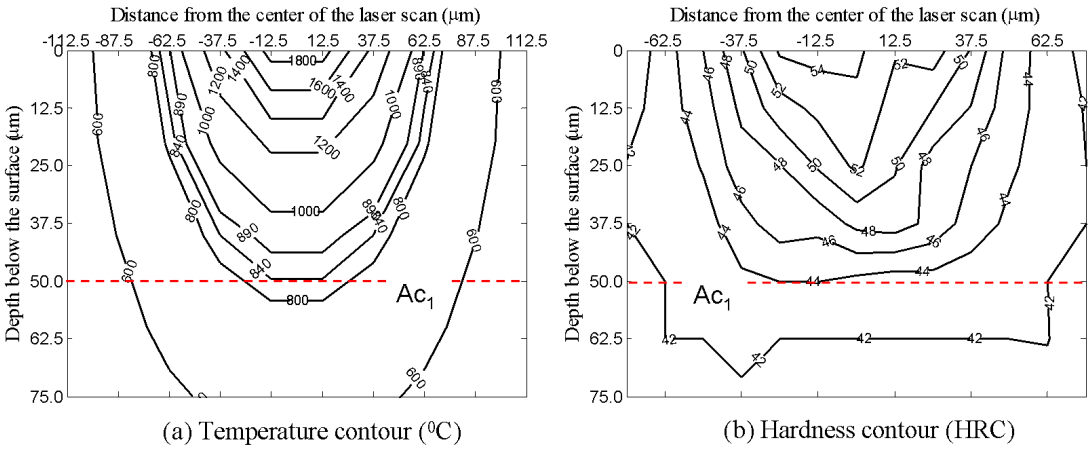

Figure 5.13: Temperature and hardness contours at 10 W laser power and 10 mm/min scan speed

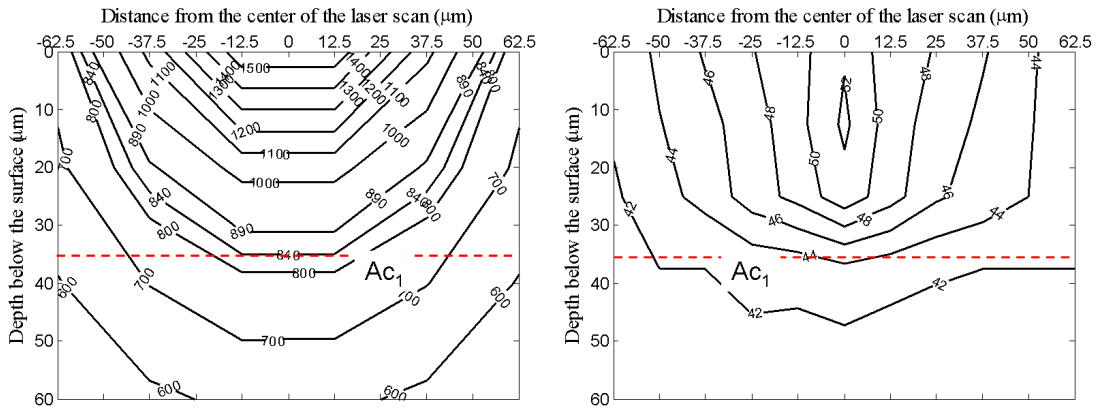

(a) Temperature contour (^{0}C) (b) Hardness contour (HRC)

Figure 5.14: Temperature and hardness contours at 10 W laser power and 50 mm/min scan speed

workpiece volume where the temperatures reach Ac_1 (840℃) and the regions where the temperatures exceed Ac_3 (890℃) are totally converted to austenite. Once the austenite is quenched by the cold interior, untempered martensite is formed, which accounts for the hardness increase in the HAZ.

5.3.2 Application of Thermal Model in Laser Assisted Micro-Grooving

In order to illustrate the utility of the thermal model in establishing the laser parameters and cutting conditions that minimize the HAZ in the final micromachined part in a process such as laser-assisted micro-grooving, an example case of creating a 25 μm deep groove in H-13 steel is selected. A 300 μm grooving tool is used in the LAMM setup described earlier with the laser spot located 100 μm from the edge of the grooving tool. The laser beam diameter is 110 μm. In order to select an ideal speed for the operation which results in no residual HAZ, simulations were carried out at different speeds and a laser power of 10 W. Fig. 5.15 shows the temperature distribution at 100 mm/min scan speed and a laser power of 10 W. The depth corresponding to Ac_1 (840℃) is 19 μm, which should correspond to the maximum HAZ depth beyond which no phase transformation (and consequently, hardness change)

should occur. Therefore, a speed of 100 mm/min was selected for the test case to investigate the presence of residual HAZ, if any.

The cross-section of the machined surface was analyzed for increase in hardness and/or microstructural changes related to the residual HAZ. Fig. 5.16(a) shows the microstructure of the machined groove cross-section and the area close to the base of the groove where the hardness is measured. Fig. 5.16(b) shows a magnified view of the center of the groove base. There is no evidence of the remelted zone as observed previously in Fig. 5.3. Any change in micro-hardness near the base of the groove indicates that the microstructure in that area has changed. Micro hardness tests were conducted near the base of the groove in the area shown in Fig. 5.16(a). Fig. 5.17 shows the hardness as a function of distance measured from the left edge of the groove shown in Fig. 5.16(a).

The hardness measurement varies between 40.4 and 42.5 HRC, which is within the range of the base hardness (42±2 HRC) of the H-13 steel used in the current work. Consequently, it can be concluded that the HAZ and any associated phase transformation was confined to the volume of material removed by the micro-grooving tool. This demonstrates that the thermal model can be used to determine the size of the HAZ in LAMM based micro-grooving.

5.4 Summary

This chapter focused on characterizing and predicting the HAZ produced by laser heating in the LAMM based micro-grooving process. The following conclusions summarize the work presented in this chapter:

- The size of the HAZ depends on the laser scanning speed and laser power. The maximum width and depth of the HAZ decrease by 32% and 62%, respectively, when the scan speed is increased from 10 mm/min to 100 mm/min at a laser power of 10 W.

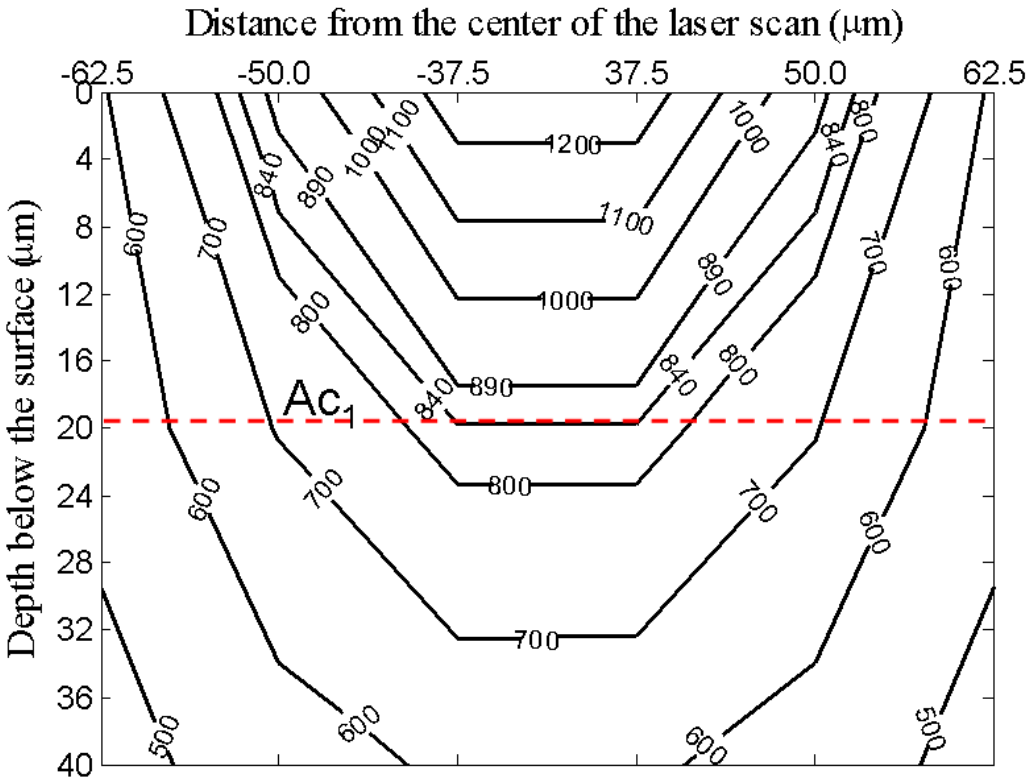

Figure 5.15: Temperature contours (°C) at 10 W laser power and 100 mm/min scan speed

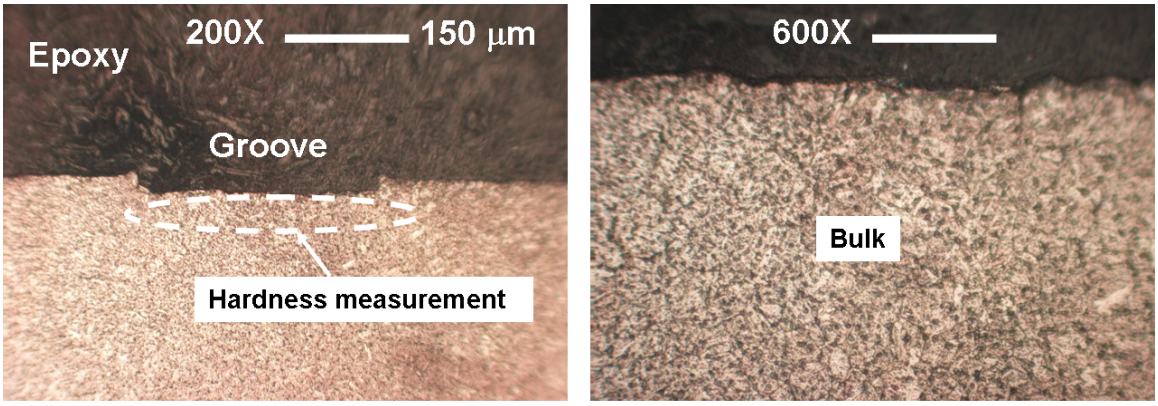

(a) (b)

Figure 5.16: Microstructure of the cross-section of test cut with 300 μm grooving tool at 10 W laser power and 100 mm/min cutting speed

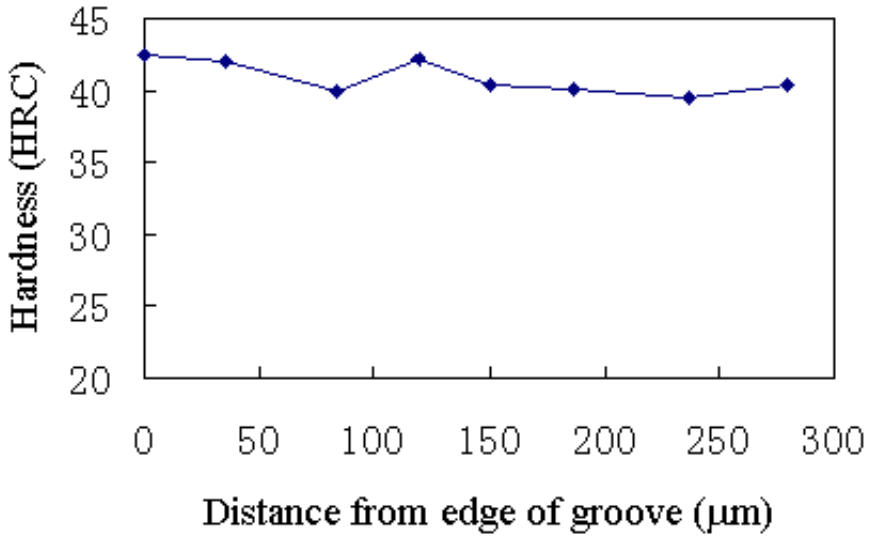

Figure 5.17: Hardness at the base of the groove

- The transient 3-D finite element model developed to analyze the temperatures within the HAZ predicts the temperature to within 15% of the measured values.
- A critical temperature range (840∼890℃) corresponding to the depth of HAZ produced in H-13 steel (42 HRC) at different scan speeds was identified. If the temperature in the material removal region is below the critical range then there will be no residual HAZ in the material after micro cutting.
- The thermal model can be used to determine the laser parameters for a given cut geometry that will yield no residual HAZ in the material after micro-grooving.

CHAPTER VI

FORCE MODELING IN LASER ASSISTED MICRO-GROOVING

The previous chapter discussed the temperature distribution and heat affected zone in the workpiece material. Besides knowing the material temperature and depth of HAZ, knowledge of the cutting and thrust forces is also required in order to understand the impact of machine, tool and/or workpiece deflections on the accuracy of the micromachined feature and for improving feature dimensional accuracy and avoiding premature tool breakage. The LAMM process is characterized by lower cutting forces and deflections, fewer premature tool failures and potentially higher material removal rates. Nevertheless, the selection of laser and cutting parameters that yield the desired reduction in cutting forces and machine-tool deflection, and consequently an improvement in the dimensional accuracy of the micro machined feature, requires an accurate cutting force model. This chapter presents a force model for the laser-assisted micro grooving process. The modeling approach accounts for the effects of thermal softening due to laser heating, machine elastic deflection, and tool edge radius on the depth of cut and forces. Experiments carried out on H-13 steel (42 HRC) are used to validate the force model under different conditions. Model simulations are also carried out to analyze the effects of laser power and cutting speed on the forces and actual feature size (groove depth) produced.

6.1 Force Modeling

The cutting action in laser assisted micro-grooving is assumed to be orthogonal for the purpose of force modeling. The overall methodology for prediction of the forces in

laser assisted micro-grooving is shown in Fig. 6.1. The key elements of the methodology consist of the thermal model of laser heating (discussed in Chapter 5), a slip-line field based geometric model of plastic deformation arising from chip formation [105], a material model of the material flow strength [106], a force model derived from the slip-line field model [105], and a model for taking into account the influence of machine/tool elastic deflection. Each of these elements in the overall methodology is discussed below. The outputs of the complete model are the cutting and thrust forces and the actual (equilibrium) depth of cut.

6.1.1 Temperature Distribution in Material Removal Plane

As described earlier in Chapter 5, the thermal model takes into account the effects of laser parameters such as laser power, spot size, scan speed and distance of the tool edge from the center of the laser spot. The output of the thermal model is the temperature, T, at each point in the material. Note that temperature dependent thermophysical properties are used in the model. Also, the average workpiece absorptivity has been determined for each case using simulations and temperature measurements made at a known location on the workpiece surface as described in Chapter 5 and Singh and Melkote [107-108].

Fig. 6.2 shows the temperature distribution in the material removal half plane, i.e., in the half plane containing the tool edge and perpendicular to the workpiece surface (as indicated by the shaded area in Fig. 6.3). Note that the tool edge is located 100 μm behind the center of the irradiated spot. It can be clearly seen in Fig. 6.2 that the temperatures in the material removal half plane vary quite a bit (from 540 to 380 ℃). This temperature distribution is used as input to the material model to determine the flow stress variation in the material removal plane, as discussed later.

It should be noted that the temperature rise due to laser heating is substantially

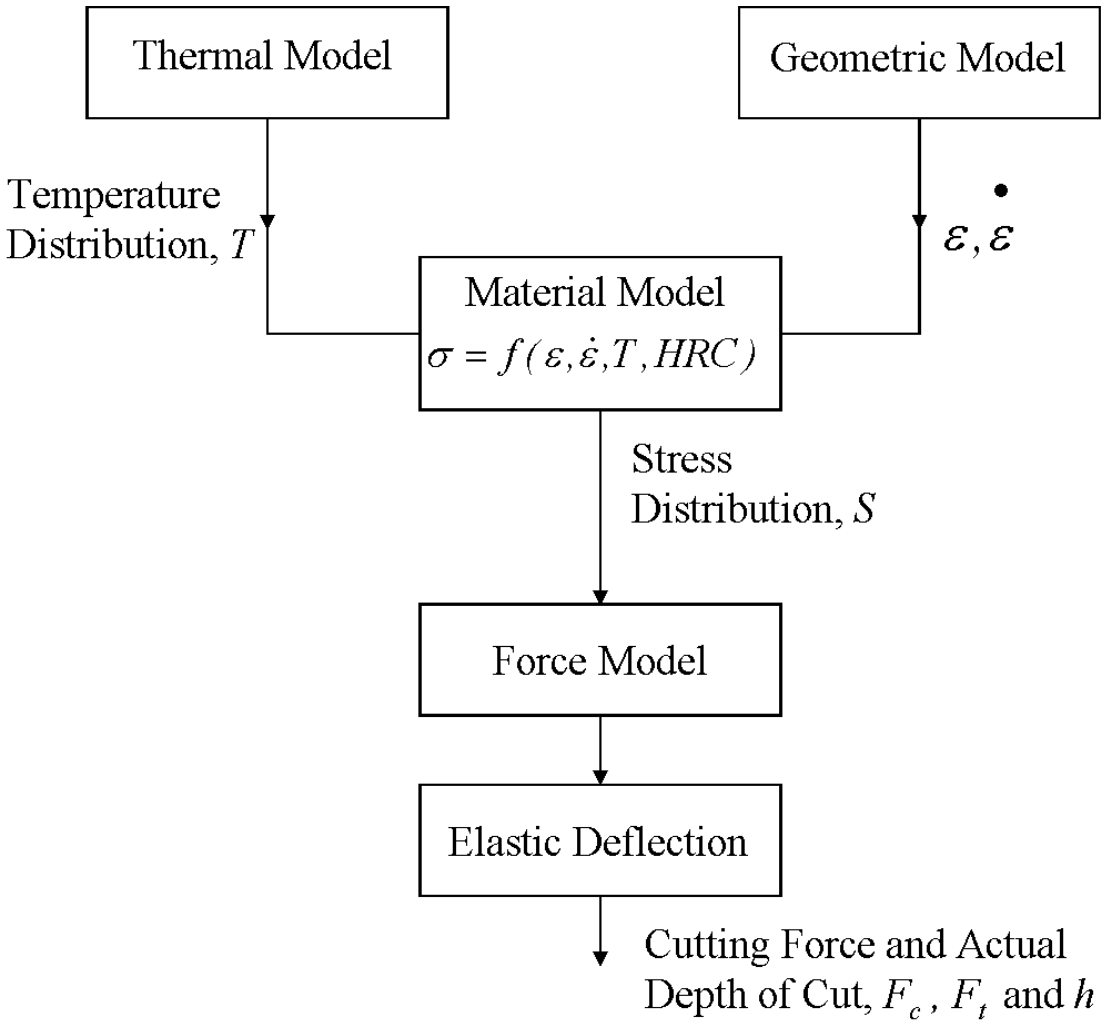

Figure 6.1: Flow chart of force prediction methodology

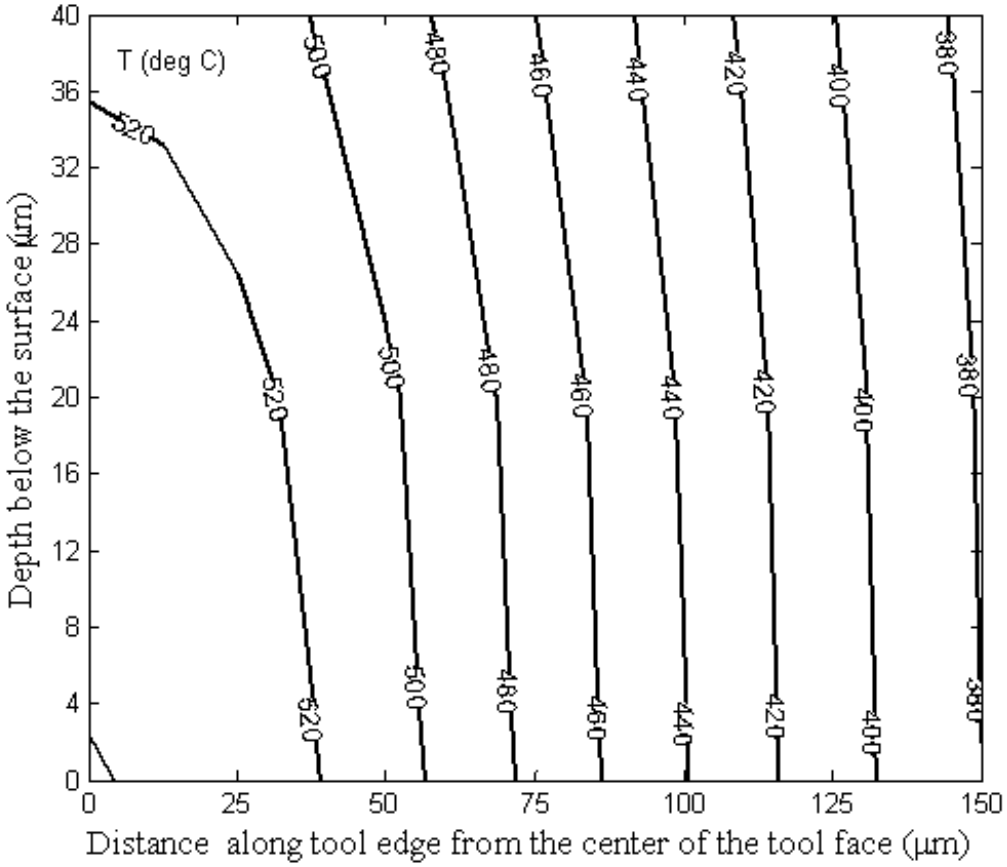

Figure 6.2: Simulated temperature distribution in the material removal half plane

higher than the plastic energy dissipation associated with chip formation due to shearing. For example, the estimated temperature rise due to shearing is only about 52°C (for 10 μm depth of cut and 50 mm/min speed) as compared to a maximum temperature rise in the material removal plane of approximately 1000°C for 35 W laser power. Thus, the temperature rise due to shearing can be ignored in laser assisted mechanical micromachining.

6.1.2 Geometric Model of Slip-line Field

The force model is based on an existing slip-line field model of orthogonal cutting proposed by Manjunathaiah and Endres [105]. For simplicity, the grooving operation

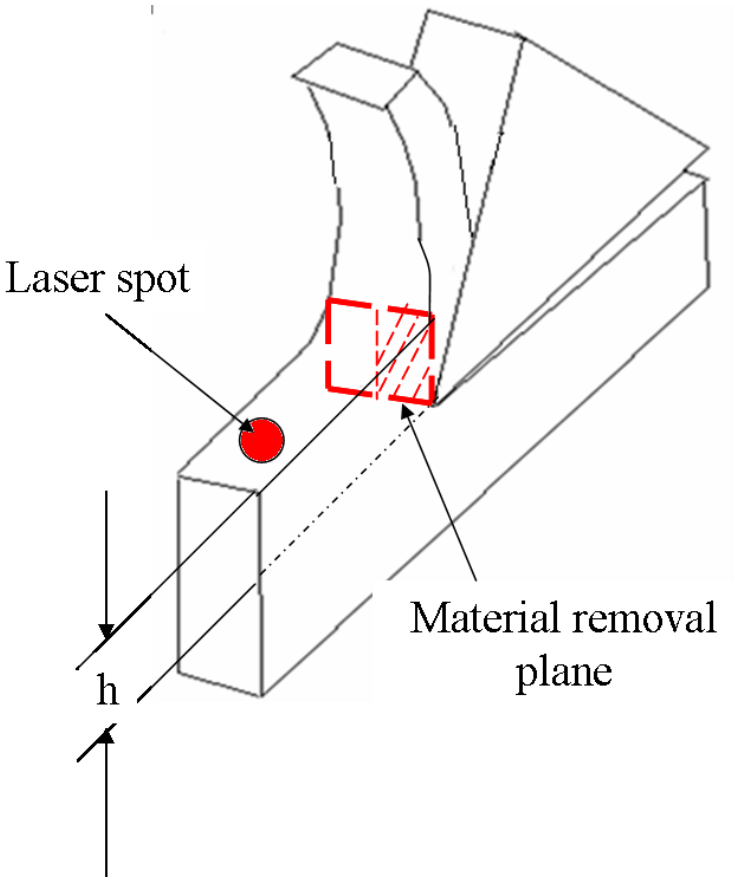

Figure 6.3: Location of material removal plane

is modeled as a plane strain orthogonal cutting process. The validity of this assumption is supported by force measurements that show the third (lateral) component of force to be negligible in comparison to the cutting and thrust forces. In addition, no side-flow is observed in the chip. The use of a slip-line field model is justified here since such models have been used successfully by several researchers for conditions that can be classified as micro-cutting [106, 107] and for other microscale processes such as polishing [108]. Recently, Waldorf et al. [109] have used a slip-line field model to predict cutting forces at depths of cut as low as 6 μm.

In the Manjunathaiah and Endres' model, plastic deformation occurs in the zone ABCP shown in Fig. 6.4; ADP is the deformed chip area and BDCP is the deformed workpiece area.

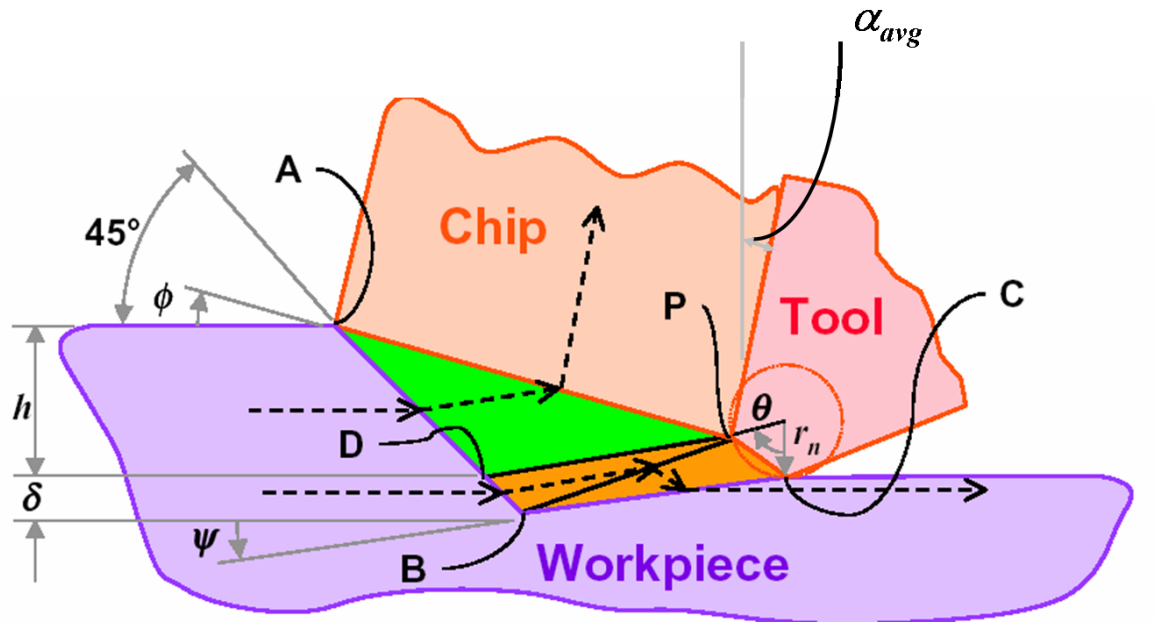

Figure 6.4: Geometric model of the cutting process with an edge radius tool [105]

The depth of plastic deformation below the tool in the workpiece surface is given by [105]:

$$\delta = \frac{(h-p)\,cot\phi + r_n sin\theta - h}{1 + cot\psi} \tag{6.1}$$

where h is the depth of cut and p is the height of the chip separation point P measured from point C; ψ is the angle that BC makes with the horizontal and is assumed to be 20° [105]. The chip separation angle, θ, has been calculated theoretically and experimentally by a number of researchers [110, 111]. The current work assumes the value of θ to be 15° based on the work of Komanduri [111], who observed that the chip ceases to form at a rake angle of about -75°.

The tool edge radius is determined from a magnified image of the side of the grooving tool acquired by an optical microscope (see Fig. 6.5). A circle was fit to the digitized image of the tool edge profile to determine the edge radius (r_n) used in the present study. Its value was found to be about 5 μm.

The shear angle ϕ is calculated from chip thickness measurements given in Table

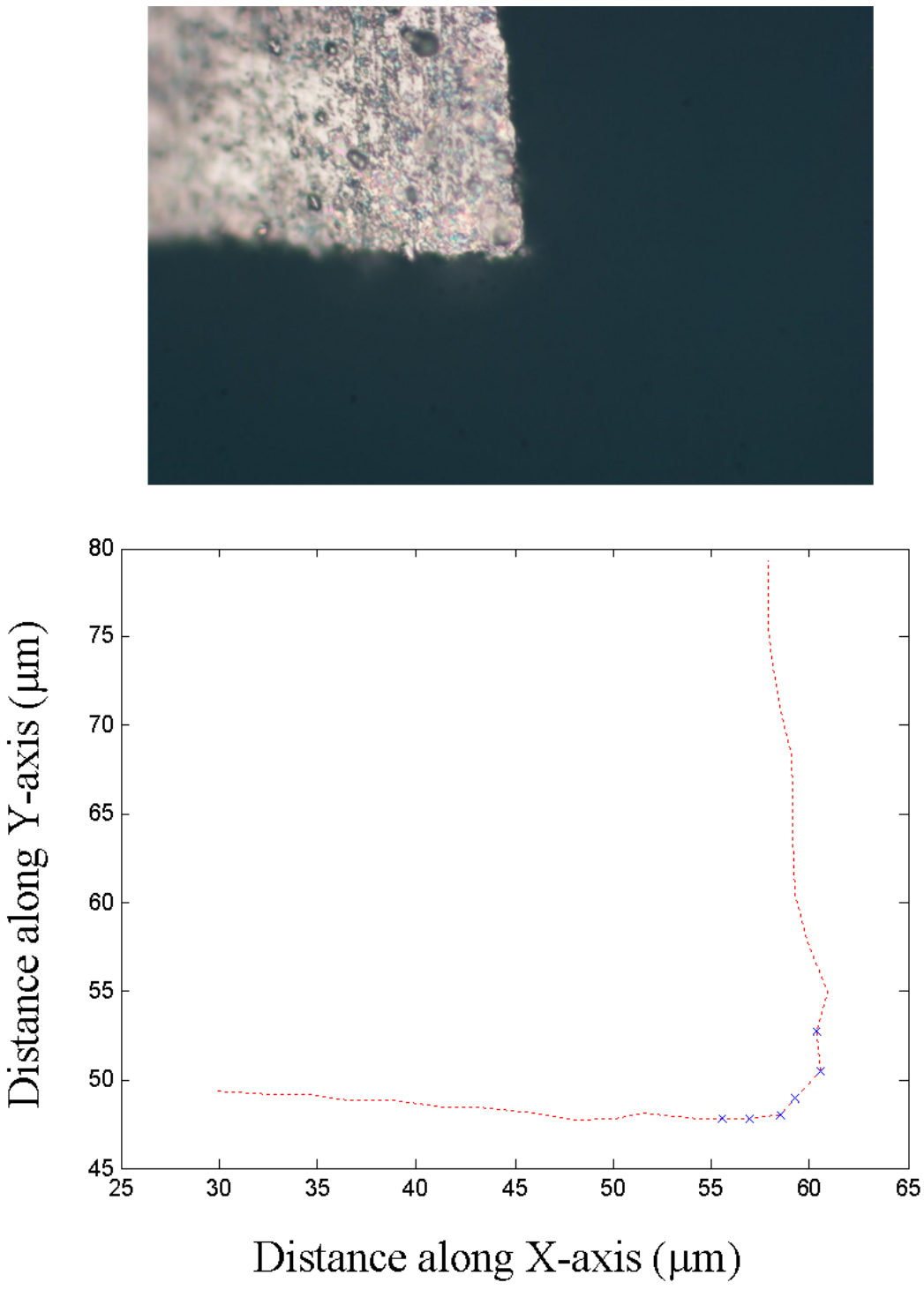

Figure 6.5: Image of the tool edge (top) and tool edge profile (bottom) extracted from it

Table 6.1: Data for calculation of shear angle

Nominal Depth of Cut (μm)	Measured Depth of Cut (μm) Mean± Std. Deviation	Measured Chip Thickness (μm) Mean± Std. Deviation
10	7.00 ± 0.76	23.13 ± 1.23
15	11.00 ± 0.81	33.29 ± 1.52
20	13.50 ± 1.15	45.54 ± 1.98
25	20.00 ± 0.99	65.26 ± 2.43

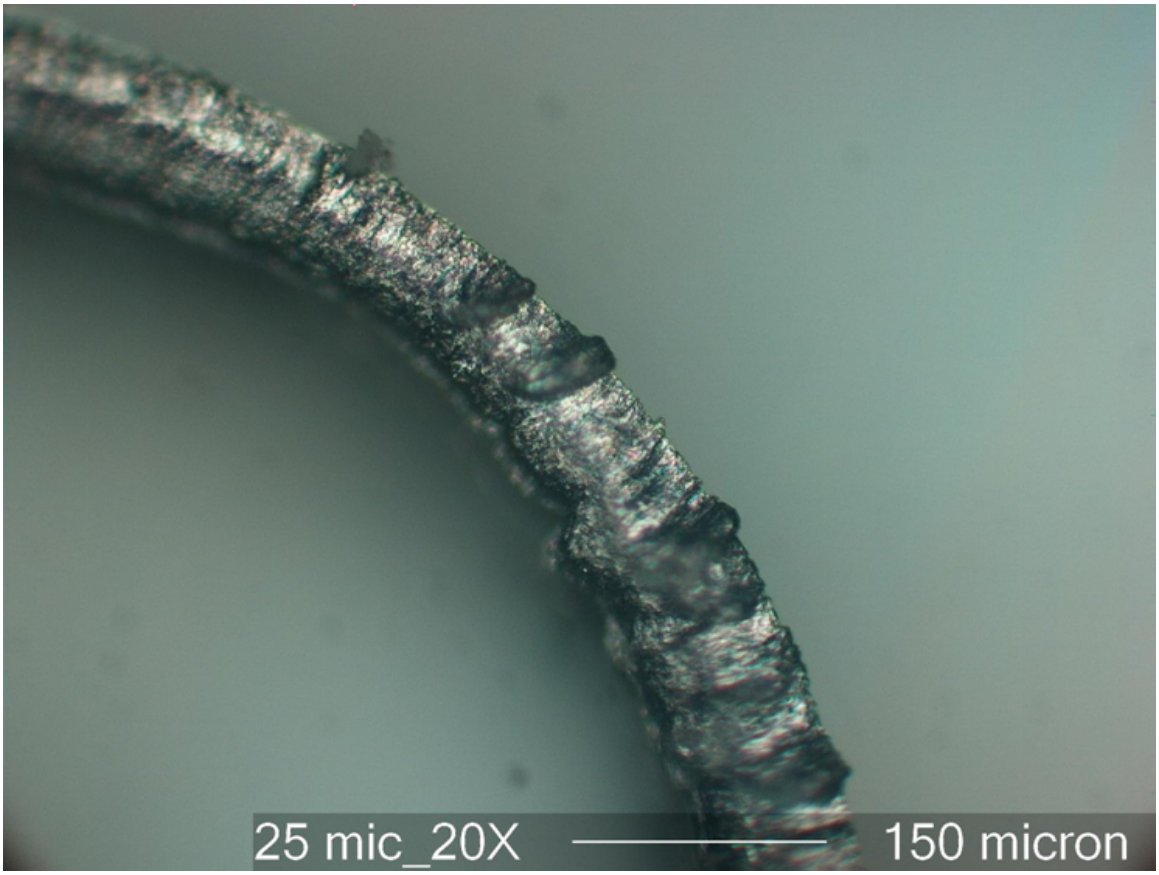

Figure 6.6: Optical image of chip

6.1. Fig. 6.6 shows an optical image of the chip produced at 25 μm nominal depth of cut. The chip thickness was determined from this image using pixel based measurement software. Assuming that ϕ does not change significantly with laser heating at a given depth of cut, it is determined from the following equation:

$$\frac{h}{h_c} = \frac{sin\phi}{cos\left(\phi - \alpha_{avg}\right)} \tag{6.2}$$

where h_c is the deformed chip thickness and α_{avg} is the average rake angle defined as [115]:

$$\alpha_{avg} = tan^{-1}\left(\frac{\left(h/r_n - 1\right)tan\alpha_0 - sec\alpha_0 + sin\theta}{h/r_n - 1 + cos\theta}\right) \tag{6.3}$$

where α_0 is the nominal rake angle.

The material flow directions in both the chip and workpiece deformation zones are shown by the dashed lines in Fig. 6.4. The net strain in the chip and workpiece are calculated as follows [105]:

$$\gamma_{chip} = \frac{\sqrt{2}sin\theta_{PD}}{sin\left(\pi/4 + \theta_{PD}\right)} + \frac{cos\left(\alpha_{avg} + \theta_{PD}\right)}{cos\left(\alpha_{avg} - \phi\right)sin\left(\phi + \theta_{PD}\right)} \tag{6.4}$$

$$\gamma_{work} = \frac{\sqrt{2}sin\theta_{PD}}{sin\left(\pi/4 + \theta_{PD}\right)} + \frac{sin\left(\theta_{PD} + \theta/2\right)}{sin\left(\theta_{PD} + \theta/2\right)sin\left(\theta_{PB} + \theta_{PD}\right)} + \frac{sin\theta/2}{sin\psi sin\left(\psi + \theta/2\right)} \tag{6.5}$$

where θ_{PD} and θ_{PB} are acute angles made by the lines PD and PB, respectively, with the horizontal. The effective strain in the workpiece is then calculated as:

$$\gamma_{eff} = \frac{v_{chip}\gamma_{chip} + v_{work}\gamma_{work}}{v_{chip} + v_{work}} \tag{6.6}$$

The shear strain rate in the chip, workpiece, and the effective strain rate are calculated as follows [105]:

$$\dot{\gamma}_{chip} = 2V\frac{\gamma_{chip}}{\sqrt{2}sin\left(\pi/4 + \theta_{PD}\right)\bar{PD}} \tag{6.7}$$

$$\dot{\gamma}_{work} = 2V\frac{\gamma_{work}}{\sqrt{2}sin\left(\pi/4 + \theta_{PD}\right)\bar{PD} + \frac{sin(\psi+\theta/2)}{sin\psi}\bar{PC}} \tag{6.8}$$

$$\dot{\gamma}_{eff} = \frac{v_{chip}\dot{\gamma}_{chip} + v_{work}\dot{\gamma}_{work}}{v_{chip} + v_{work}} \tag{6.9}$$

The effective shear strain γ_{eff} and effective shear strain rate $\dot{\gamma}_{eff}$ under plane strain conditions are related to the state variables, strain ϵ and strain rate $\dot{\epsilon}$, by the following equations [116]:

$$\epsilon = \frac{\gamma_{eff}}{\sqrt{3}} \tag{6.10}$$

$$\dot{\epsilon} = \frac{\dot{\gamma}_{eff}}{\sqrt{3}} \tag{6.11}$$

6.1.3 Constitutive Material Model

A Johnson-Cook type multiplicative material flow stress model for H-13 steel proposed by Yan et al. [106] is used in this work. In principle, this constitutive model can be extended to account for grain size, grain boundary effects and crystal misorientation based on the work of Hansen et al. [117], Hughes et al. [118] and Li et al. [119]. However, in the current work these effects are ignored and the flow stress is considered to be a function of the strain, strain rate, temperature and material hardness (HRC) only. The general form of the flow stress model of Yan et al. is as follows:

$$\sigma\left(\epsilon, \dot{\epsilon}, T, HRC\right) = \left(A + B\epsilon^n + Cln\left(\epsilon + \epsilon_0\right) + D\right)\left(1 + Eln\left(\frac{\dot{\epsilon}}{\dot{\epsilon}_0}\right)\right)\left(1 - (T^*)^m\right) \tag{6.12}$$

where, σ is the flow stress, ϵ is the plastic strain, ϵ_0 is a reference strain that is taken to be 10^{-3}, $\dot{\epsilon}$ is the strain rate, T is the temperature, $\dot{\epsilon}_0$ is a reference strain rate typically taken to be $1s^{-1}$, T_m is the melting temperature of the material, T_r is a reference temperature taken to be 25℃, and A, B, C, D, E, m and n are material constants. Their values for H-13 steel are as follows: $A = 908.54$ MPa, $B = 321.39$

MPa, $n = 0.278$, $E = 0.028$, $m = 1.18$. Note that C and D depend on the material hardness and yield stress and their values for the material hardness used in this study (42±2 HRC) are 5.92 MPa and 221.8 MPa, respectively.

The von Mises flow criterion is then used to relate the shear flow stress, S, to the uniaxial flow stress, σ , obtained from Eq. 6.12.

$$S = \frac{\sigma}{\sqrt{3}} \tag{6.13}$$

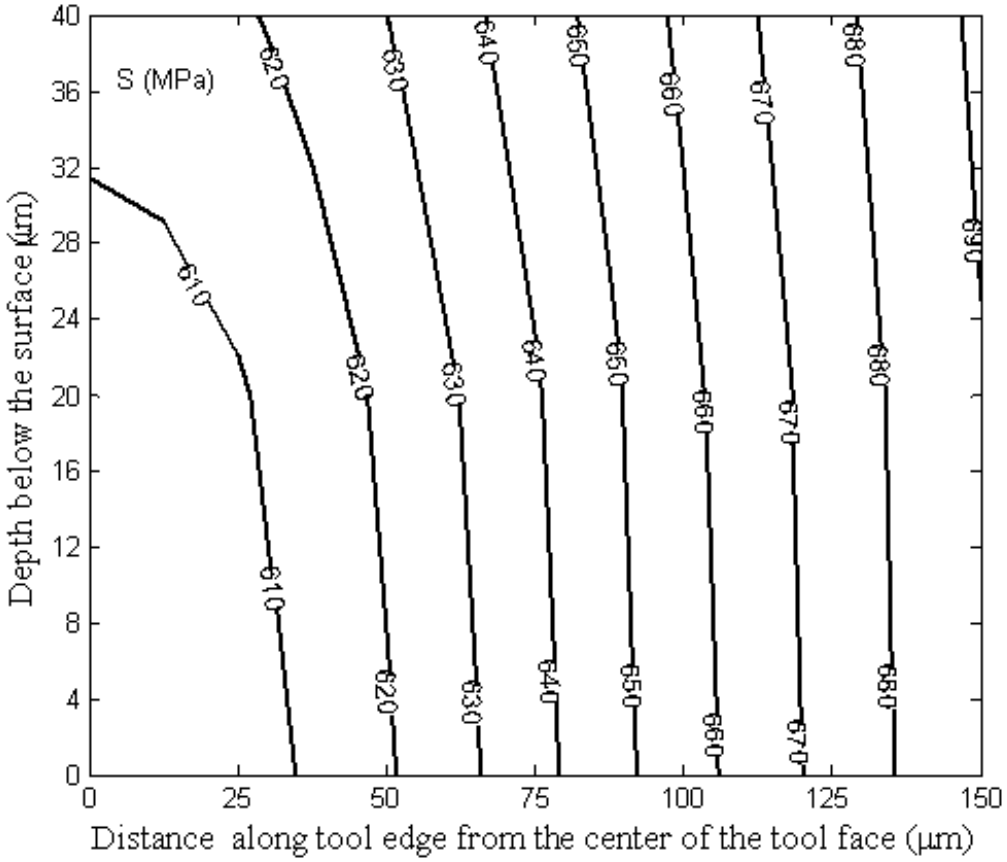

Figure 6.7: Shear stress distribution in the material removal half plane

Fig. 6.7 shows the calculated shear stress distribution in the material removal half-plane for 10 W laser power and 10 mm/min cutting speed. Note that the effect of plastic heat dissipation is ignored in calculating the shear stress since it is small

relative to laser heating. It can be seen that the flow stress is distributed in bands. The shear stress at ambient conditions is 848 MPa. Thus, a maximum reduction of 28% in the shear stress is observed under the given conditions. Note that an increase in the laser power will cause greater reduction in the shear stress (up to 66% for 35 W laser power). This shear stress distribution is used in the cutting force model to predict the cutting and thrust forces.

6.1.4 Force Model

The force model is derived from equilibrium of forces acting along the slip-lines AB and BC in Fig. 6.4. The cutting and thrust forces per unit width are given by [105]:

$$f_c = \{(h-p)\,cot\phi + h + r_n sin\theta - (k-1)\,\delta\}\,S \tag{6.14}$$

$$f_t = \{(h-p)\,cot\phi - h + r_n sin\theta + (k-1)\,\delta cot\psi\}\,S \tag{6.15}$$

Since the shear flow stress, S, is not uniformly distributed in the material removal plane (due to the non-uniform distribution of temperature), the total force in the cutting and thrust directions can be approximated as follows:

$$F_c = \{(h-p)\,cot\phi + h + r_n sin\theta - (k-1)\,\delta\}\sum_{1}^{n}\bar{S}\,(i)\,w\,(i) \tag{6.16}$$

$$F_t = \{(h-p)\,cot\phi - h + r_n sin\theta + (k-1)\,\delta cot\psi\}\sum_{1}^{n}\bar{S}\,(i)\,w\,(i) \tag{6.17}$$

Note that the banded distribution of shear stress in the material removal plane is accounted for by summing the product of the average shear stress in the i^{th} band, $\bar{S}\,(i)$, and the corresponding band width, $w(i)$, where i varies from 1 to n and n is the number of bands; k is the normal stress factor, which is determined by solving Eq. 6.14 and Eq. 6.15 simultaneously for known (measured) forces. An average value of k $(= 0.9)$ is used in the simulations presented in this chapter.

6.1.5 Machine Elastic Deflection

The machine has a finite stiffness and therefore deflects under the influence of the forces. This deflection in turn affects the actual depth of cut, which in turn affects the forces. Consequently, the equilibrium depth of cut and the corresponding cutting and thrust forces depend on the stiffness characteristics of the machine-tool system. The equilibrium static stiffness in the depth of cut (X) direction is obtained from the load-displacement characteristic for the stacked stages determined using the experimental procedure described in Chapter 4. Note that the stiffness determined is limited to the stages and does not take into account the compliance of the tool holder and tool post. The equilibrium static stiffness of the machine tool stage was determined to be 2.85 N/μm in the depth of cut direction.

Fig. 6.8 shows a flow chart summarizing the algorithm used to compute the equilibrium depth of cut and forces. The inputs are the nominal depth of cut and equilibrium stiffness (k_{equil}) and the outputs are the equilibrium depth of cut and the cutting and thrust forces. It is assumed that the deflection in the direction of the depth of cut is solely due to the thrust force. The value of the incremental change in the depth of cut,ϵ , in Fig. 6.8 is 0.01 μm. The algorithm terminates when the ratio of the thrust force and deflection reaches the equilibrium stiffness (within a tolerance).

There are a few parameters in the force model that have some uncertainty associated with them. Consequently, in order to test the robustness of the model, the sensitivity of the force model to parameters ψ, θ and k has been analyzed for the 25 μm depth of cut case. It is seen that a variation of $\pm 10^\circ$ in ψ and $\pm 5^\circ$ in θ results in worst-case variations of 8% and 2%, respectively, in the cutting and thrust forces. The cutting force, F_c, is found to be relatively insensitive to variation in k; specifically, less than 5% change is observed if the value of k is changed from 0.8 to 1.2. The thrust force, F_t, is somewhat more sensitive to k and a change of 15% is observed for similar variation in k.

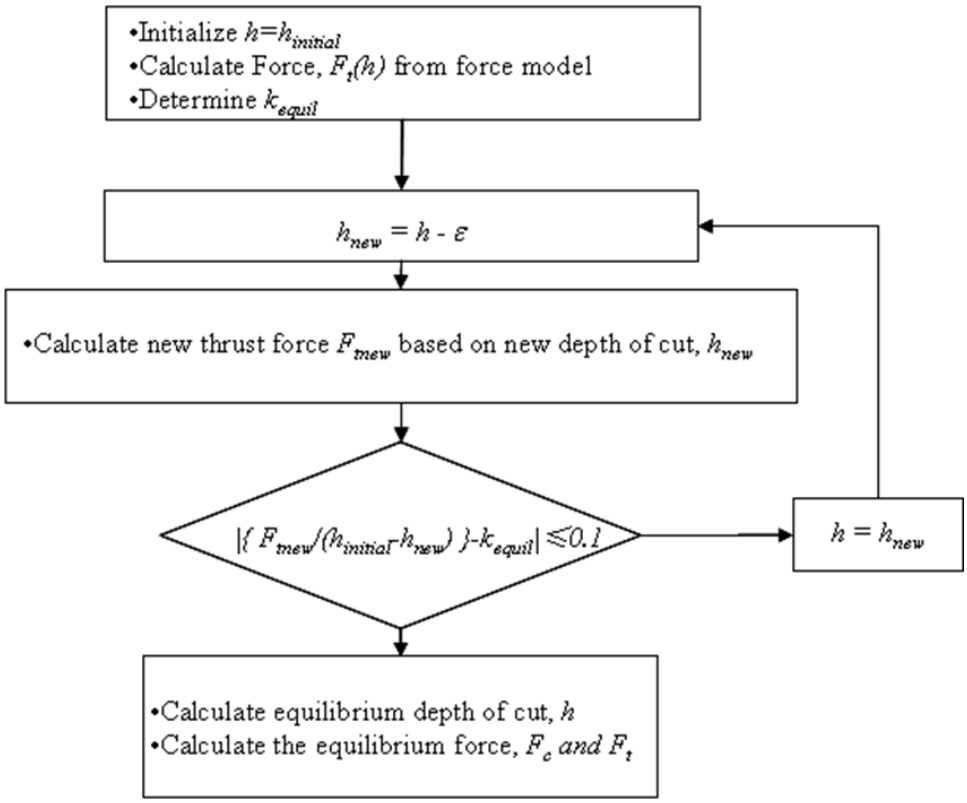

Figure 6.8: Flow chart for determining the equilibrium depth of cut and the equilibrium cutting and thrust forces

6.2 Micro-grooving Experiment

A combination of existing cutting force data from Chapter 4 and a new set of experiments at higher laser power are used to validate the cutting force model. The experimental conditions and their levels are listed in Table 6.2. Note that the tests corresponding to 35 W laser power are new while tests at 0-10 W are taken from Chapter 4. The tool edge is located at a distance of 100 μm or 200 μm from the center of the laser spot. A total of 50 test combinations with three replications per test condition are carried out. The complete data is given in the Appendix. The measured responses are the cutting and thrust forces and the resulting groove depth, which is equivalent to the actual depth of cut in the presence of elastic deflection. The groove depth is measured using a scanning white light interferometer-based surface profiler (Zygo NewView 200).

Table 6.2: Experimental Conditions

Depth of Cut (μm)	Tool Width (μm)	Cutting Speed (mm/min)	Laser Location (μm)	Laser Power (W)
10	300	10	100	0
15		50	200	5
20		100		10
25				35

6.3 Model Validation and Evaluation

The force model developed here is used to analyze the effects of depth of cut, laser power, and cutting speed on the cutting and thrust forces and the actual depth of cut due to machine elastic deflection. The predicted values are compared with experimental results.

6.3.1 Effect of Depth of Cut

Fig. 6.9 and Fig. 6.10 compare the measured and predicted cutting and thrust forces with and without machine elastic deflection at different depths of cut for the 10 mm/min cutting speed case and without laser heating. The error bars indicate the range of the measured data.

The force data shown in Fig. 6.9 and Fig. 6.10 are plotted as a function of the nominal depth of cut, which ranges from 10 μm to 25 μm. The force model captures the effect of depth of cut. It can be seen that both the cutting and thrust forces tend to be slightly over-predicted when computed without accounting for machine elastic deflection. The errors in the cutting force prediction without elastic deflection are less than 12% but the thrust force prediction errors are as high as 28%. On the other hand, the minimum and maximum errors in the cutting force prediction with elastic deflection are 9.7% and 16%, respectively, while the thrust force prediction errors range between 0.78% and 17%, respectively. It can be seen from Fig. 6.10 that there is significant improvement in thrust force prediction when the stage elastic deflection is included. This is because the deflection in the depth of cut direction has the greatest effect on the thrust force. Possible sources of prediction error include uncertainty in the values of the parameters ψ, θ and k, and possible inaccuracies in the material flow stress model obtained from literature.

As mentioned earlier, the actual depth of cut can be different from the nominal depth of cut because of tool-machine deflection due to the machining forces. Fig. 6.10 shows a comparison of the predicted equilibrium depth of cut including the effect of elastic deflection and the measured groove depth for a cutting speed of 10 mm/min and no laser heating. It can be seen that the model is in reasonable agreement with the measurements in most cases, except for the 20 μm nominal depth of cut case. Excluding this case, model prediction errors for all other cases range from 7% to 15%. Note that the model takes into account only stage deflection while other

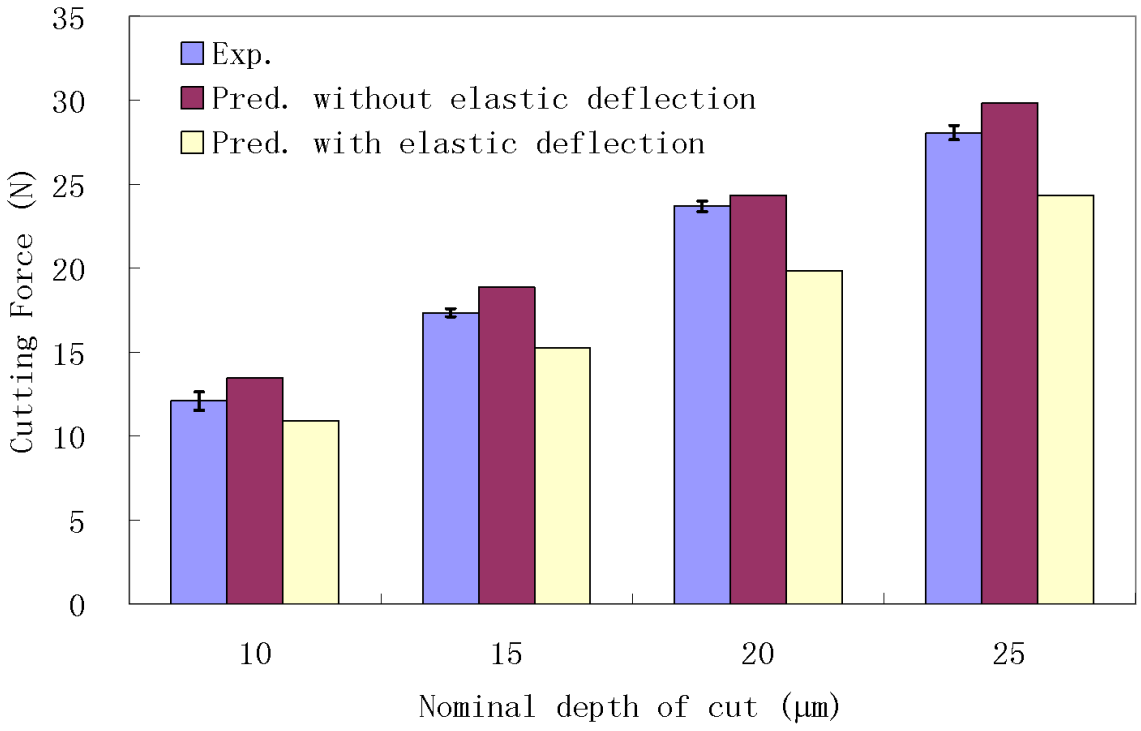

Figure 6.9: Experimental and predicted cutting forces for 10 mm/min cutting speed and no laser heating

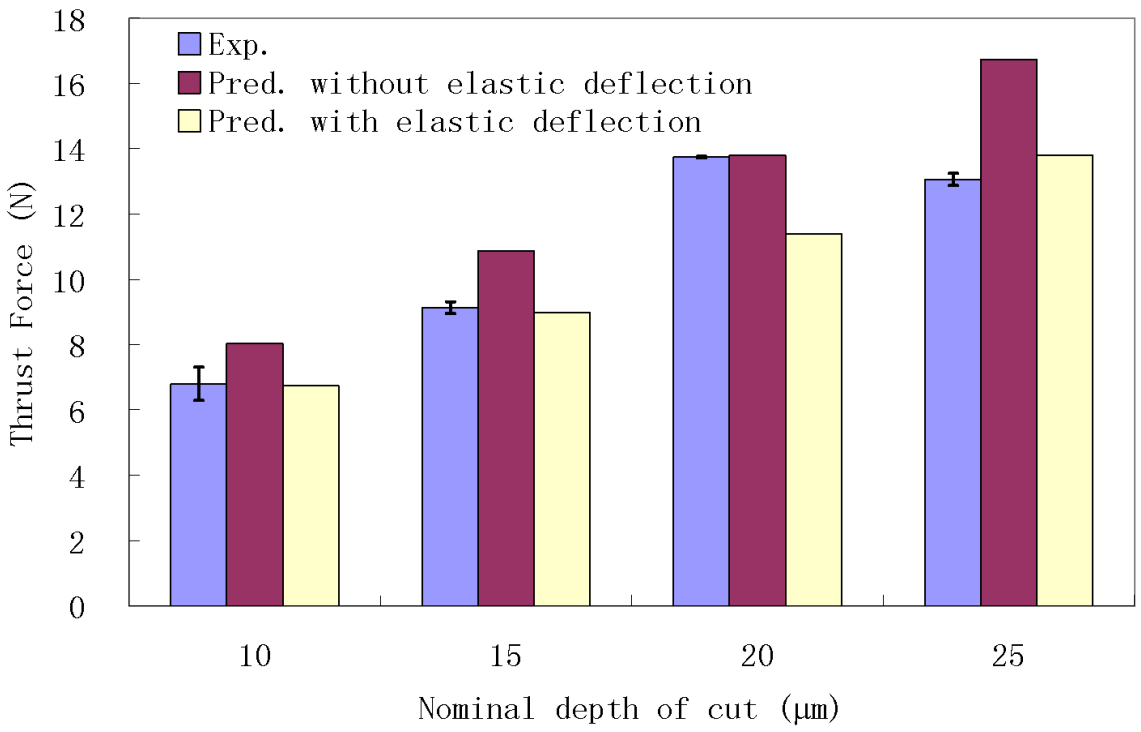

Figure 6.10: Experimental and predicted cutting forces for 10 mm/min cutting speed and no laser heating

sources of compliance such as the tool holder and tool post have not been accounted for, which may explain the model over-prediction in the depth of cut. Another reason can be inaccuracies in the material model. If the strength of material is increased by 10%, the cutting force prediction error is reduced from 10% to 2%, the depth of cut prediction error is reduced from 8% to 4% but the thrust force errors go up from 1% to 8%.

6.3.2 Effect of Laser Power

The laser power is an important parameter as it determines thermal softening and consequently reduction in the cutting and thrust forces. Fig. 6.12 shows the experimental and predicted cutting and thrust forces for 25 μm nominal depth of cut and 10 mm/min cutting speed and 0 W and 35 W laser powers.

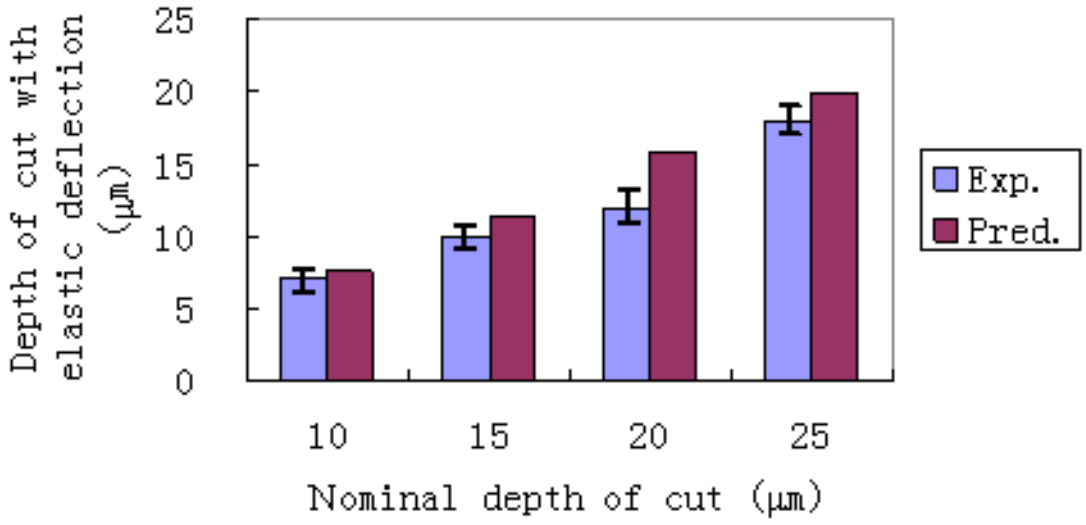

Figure 6.11: Measured and predicted depths of cut

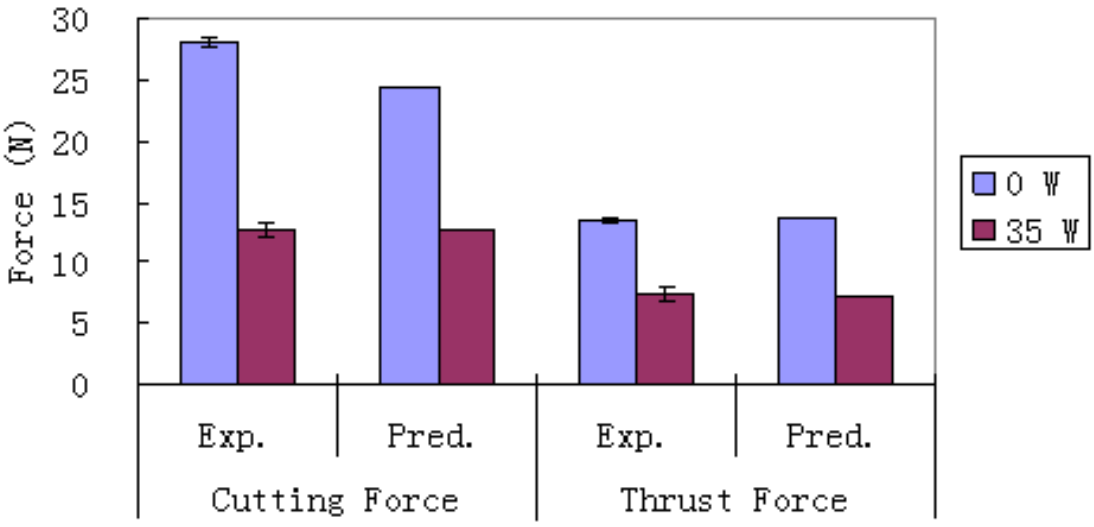

Figure 6.12: Measured and predicted cutting and thrust forces at 0 W and 35 W laser powers

It can be seen from the figure that there is approximately 48% reduction in the predicted cutting and thrust forces with laser heating compared to no laser heating. The corresponding experimental values for the cutting and thrust force reductions

are 55% and 46%, respectively.

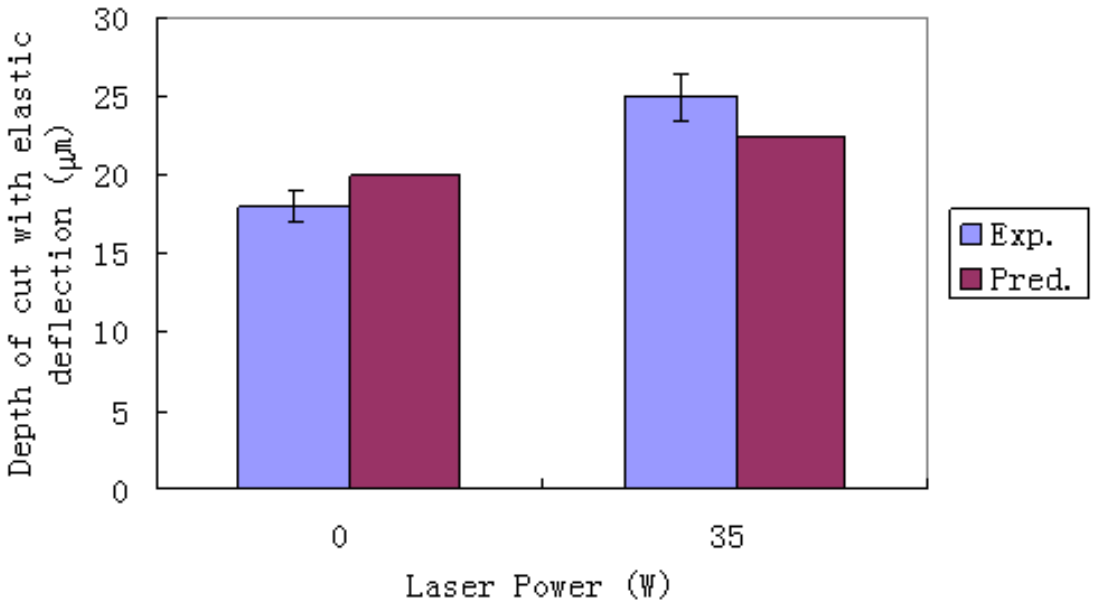

Figure 6.13: Measured and predicted depths of cut at 0 W and 35 W laser powers

Fig. 6.13 shows the measured and predicted depths of cut for 25 μm nominal depth of cut and 10 mm/min cutting speed with and without laser heating. It can be seen that the model captures the effect of laser power on the depth of cut. As observed in Fig. 6.11 and Fig. 6.13, the model tends to over-predict the depth of cut by about 10% without laser heating and under-predict it by the same amount with laser heating. This under-prediction of the depth of cut with laser heating is attributed to tool thermal expansion due to the heat conducted into the tool as described in Chapter 4. The tool thermal expansion can be as high as 3.5 μm for 35 W laser power and is not accounted for in Fig. 6.13. A detailed analysis of the tool thermal expansion effect is described in Chapter 4. The reason for the over-prediction of the depth of cut without laser heating has been given in the previous section.

It is interesting to note that the effect of laser power on the cutting force component is not significant at low (5-10 W) laser powers as seen in Chapter 4. A sample

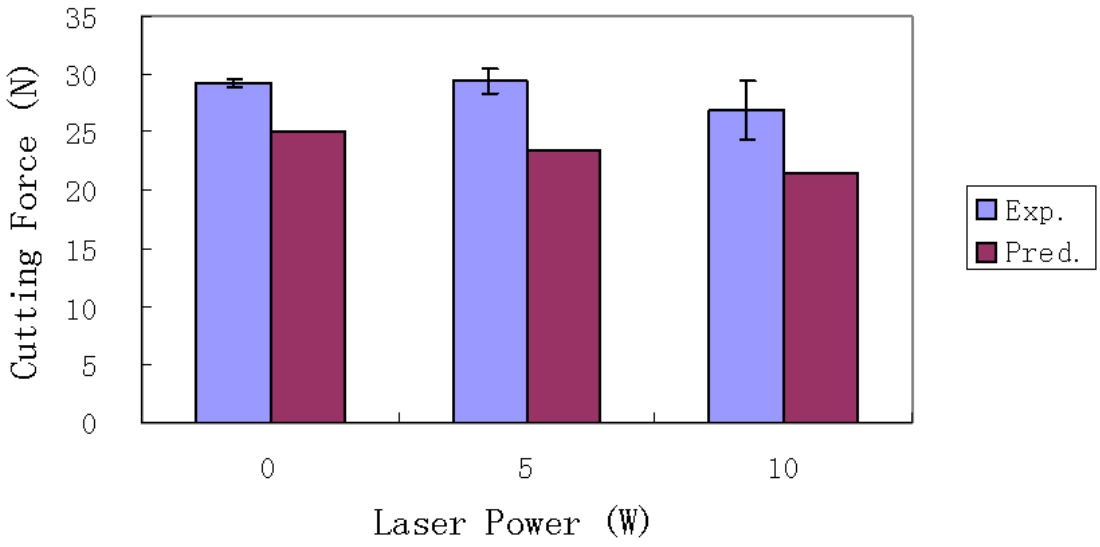

Figure 6.14: Cutting forces at 25 μm nominal depth of cut, 50 mm/min cutting speed and 0, 5 and 10 W laser powers

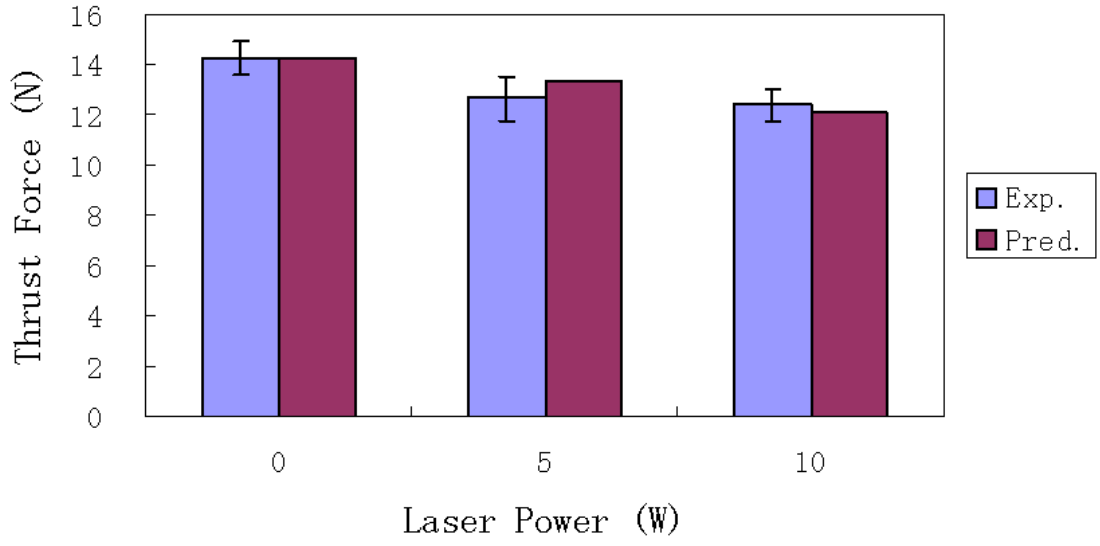

Figure 6.15: Thrust forces at 25 μm nominal depth of cut, 50 mm/min cutting speed and 0, 5 and 10 W laser powers

result is shown in Fig. 6.14 and Fig. 6.15 for the following conditions: 25 μm nominal depth of cut, 50 mm/min cutting speed and 0, 5 and 10 W laser powers. However, if

the laser power is increased further, a significant reduction in cutting force is achieved as seen earlier in Fig. 6.12. This is attributed to the increased thermal softening arising from the higher temperatures produced in the material removal plane at higher laser powers. For instance, the temperature in the material removal plane for the 35 W laser power case range from 682°C to 1042°C, whereas they range from 295°C to 438°C for the 10 W laser power case shown in Fig. 6.14 and Fig. 6.15. Consequently, the reduction in the force components may not always be significant at lower laser powers.

6.3.3 Effect of Cutting Speed

The effect of cutting speed on the forces is significant because with increase in speed the time available for heat conduction into the workpiece decreases. Consequently, it is expected that the cutting force will increase with increase in cutting speed. Fig. 6.16 shows the measured and predicted forces at 25 μm nominal depth of cut and 35 W laser power without taking into account tool thermal expansion.

It can be seen that there is an average increase of 43% in the measured cutting force when the cutting speed is increased from 10 mm/min to 100 mm/min. The predicted cutting force also shows an increase, albeit to a smaller extent (25%). The model also tends to under-predict the cutting and thrust forces at 100 mm/min although the observed trends are generally captured by the model. There is good agreement between the measured and predicted forces at the slower cutting speed with errors less than 1%. If the effect of tool thermal expansion (can be as high as 3.5 μm for 35 W laser power) is included, the prediction errors at 100 mm/min cutting speed are reduced from 15% to 4% for the cutting force and from 28% to 19% for the thrust force. As mentioned earlier, possible sources of error in the model include uncertainty in the values of the model parameters ψ, θ and k, inaccuracies in the material flow stress model and other modeling assumptions. In spite of these error sources, the

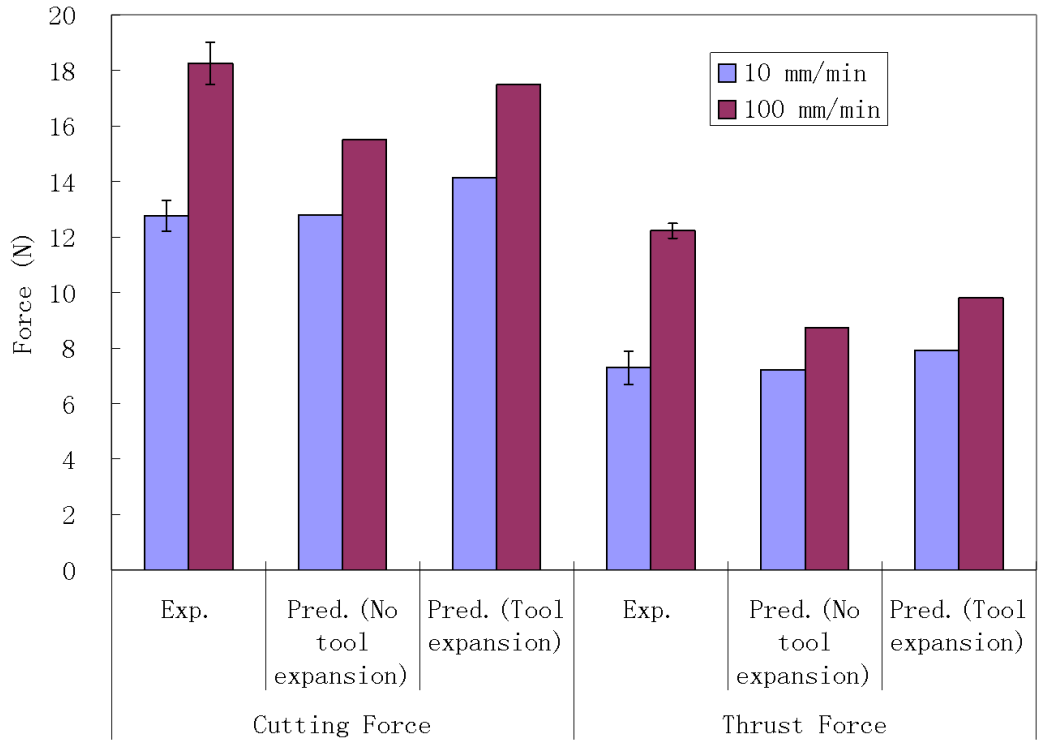

Figure 6.16: Measured and predicted cutting and thrust forces at 10 mm/min and 100 mm/min cutting speeds, 35 W laser power and 25 μm nominal depth of cut

model is found to predict with reasonable accuracy over a wide range of conditions.

6.4 Summary

This chapter presented a force model for the LAMM based micro-grooving process. The force model can capture the effects of thermal softening, edge radius of the tool and compliance of the machine stages. Inspite of the assumptions, the current model predicts forces and feature size with reasonable accuracy. The following specific conclusions can be drawn from the current work:

- The slip-line field based force model for the laser-assisted micro-grooving process captures the observed trends accurately. The model prediction errors are in most cases (46 out of 50) less than 20% with the highest errors (38% for cutting

force) and (58% for thrust force) seen in the 10 μm depth of cut tests, which are characterized by small force magnitudes.

- The model predicts the actual depth of cut to within 4 to 10% of the measured values in all cases but one where the error is 30%.

- The model can predict the shear stress distribution resulting from thermal softening in the material removal plane. A 66% reduction in the shear flow stress is observed for 35 W laser power.

- The model captures the effect of thermal softening as a result of increase in laser power and up to 48% reduction in the cutting and thrust forces is observed at 35 W laser power.

- The model captures the observed trends for the effect of cutting speed. An increase in the speed leads to an increase in the cutting and thrust forces.

The force model can be used to develop an engineering-statistical model in which the engineering models are improved via statistical techniques. This improved model is used to optimize the process to select laser and cutting parameters to achieve desired feature size without a heat affected zone at minimum cutting forces. The engineering-statistical model and optimization approach is presented in Chapter 7.

CHAPTER VII

OPTIMIZATION OF THE PROCESS VARIABLES

This chapter is aimed at developing a framework for optimizing the LAMM process. It builds on the work presented in the previous chapters. A thermal model of a circular Gaussian moving laser heat source was developed and correlated with experimentally determined heat affected zone (HAZ) in Chapter 5. The main motivation for thermal modeling of the process is to determine the temperature distribution in the hard workpiece material as well as size of the heat affected zone (HAZ) as a function of the laser variables. This capability will be useful in optimizing the process to minimize workpiece thermal damage. In addition, a force modeling methodology was developed and presented in Chapter 6, which consists of the thermal model of laser heating, a slip-line field based geometric model of plastic deformation arising from chip formation, a material model of the material flow strength, and a force model derived from the slip-line field model, which also accounts for the influence of machine/tool elastic deflection. The outputs of the complete model are the cutting and thrust forces and the actual (equilibrium) depth of cut. In order to use the LAMM process effectively there are two major issues that need to be addressed. They are the dimensional error in the machined feature due to elastic deflection of the machine-tool system and the residual heat affected zone in the machined surface, respectively. The work described in this chapter is aimed at developing a methodology to select process variables to address these issues. Specifically, the goal is to find the optimal cutting and laser parameters for machining the desired feature size without any residual HAZ

at while minimizing the micro-cutting forces.

The thermal and force/deflection models presented Chapters 5and 6 have prediction errors when compared with the experimental values. These errors can be attributed to the assumptions underlying the model and uncertainty in the values of certain parameters used in the force model. The constitutive material model and the thermal model serve as inputs to the force model and consequently errors associated with these models will also have an effect on the overall accuracy of prediction. In order to account for these errors in the engineering models (e.g. Thermal model, force model, etc.), a modeling approach called engineering-statistical modeling approach [112] that improves the prediction accuracy of engineering models based on statistical techniques can be used. The engineering models typically have simplifying assumptions leading to prediction errors. On the other hand, statistical models yield accurate predictions only at points close to the observed experimental data. The engineering-statistical modeling approach combines the advantages of the engineering and statistical models and thus minimizes their individual drawbacks [112]. The engineering-statistical models for cutting and thrust forces and actual depth of cut are developed in this chapter. To reduce the computational time associated with the finite element-based thermal model presented in Chapter 5, metamodels are fit to the temperature predictions from the finite element model. Finally, because of the conflicting nature of the optimization objectives presented later in the chapter, a Pareto-frontier approach is used to find the optimum condition that meets the criteria mentioned above from a range of input variables. The following sections deal with the engineering models, experimental work, optimization and validation.

7.1 Engineering Models

The engineering models used in the current work consist of the thermal model of laser heating and the detailed force model for prediction of the cutting/thrust and

the depth of cut.

7.1.1 Thermal Model and Heat Affected Zone

Recall that the thermal model developed in Chapter 5 takes into account the effects of laser parameters such as laser power, spot size, scan speed and distance of the tool edge from the center of the laser spot. The output of the thermal model is the temperature, T, at each point in the material. The model has been validated through actual temperature measurements. Note that temperature dependent thermophysical properties are used in the model. It should be noted that the temperature rise due to laser heating is substantially higher than the plastic energy dissipation associated with chip formation due to shearing. Consequently, the contribution of shearing to the temperature rise can be neglected.

As described in Chapter 5, the mechanism of laser hardening depends on the temperature. Experiments show that the maximum depth of the HAZ depends on the laser power and laser scanning speed, which influences the resulting temperature distribution in the material. The HAZ is characterized by changes in the microstructure and mechanical properties. As shown in Chapter 5, microhardness tests can quantify the extent of the HAZ. The temperature corresponding to the transition hardness is close to the Ac_1 temperature (840℃) for H-13 steel. This correspondence of the critical temperature to the transition hardness (and consequently the depth of the HAZ) can be explained by the mechanism of laser hardening [97, 113]. The significance of the correlation lies in the fact that it is possible to control/minimize the size of the HAZ in LAMM by appropriately adjusting the laser parameters (power, scan speed, etc.). Specifically, the HAZ can be minimized by choosing the laser parameters such that the critical temperature at the intended depth of cut in micro-grooving is less than the Ac_1 temperature for the steel.

If the material is viewed from the direction shown in Fig. 7.1, the shaded area

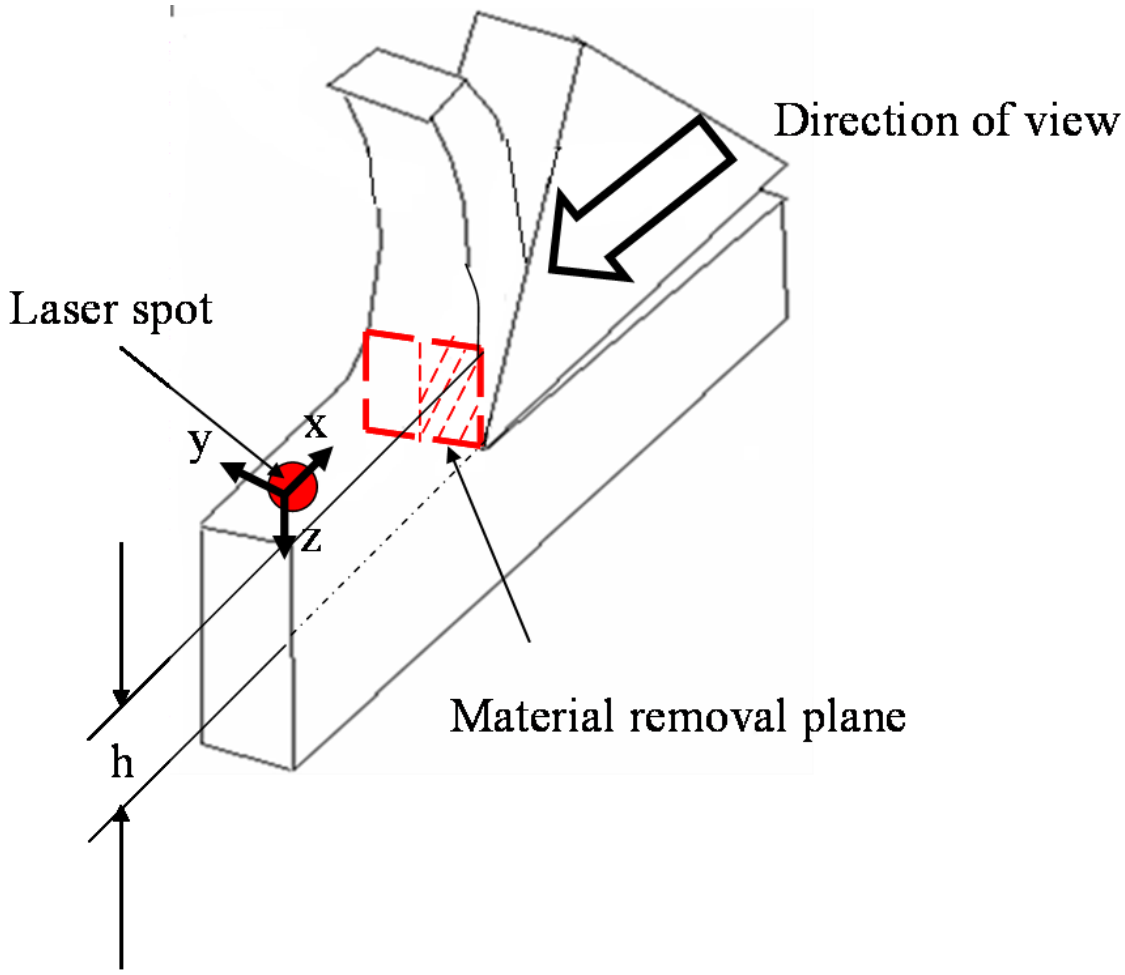

Figure 7.1: Location of material removal plane

ABCD (see Fig. 7.2) is the material removal plane. CD is the edge of tool-workpiece interface located at the intended depth of cut. The temperature distribution is symmetric about the center of the laser irradiated spot and therefore temperatures at C and D are equal and their value is denoted by T_1. The temperature T_2 in Fig. 7.2 is the temperature that occurs directly under the laser spot at the depth of cut, h. If T_2 exceeds Ac_1 then there will be residual HAZ in the machined surface after the tool has passed. The optimal parameters of the laser-assisted micro-grooving process should ensure that T_2 does not exceed Ac_1 but at the same time T_1 should be maximized to achieve maximum possible softening.

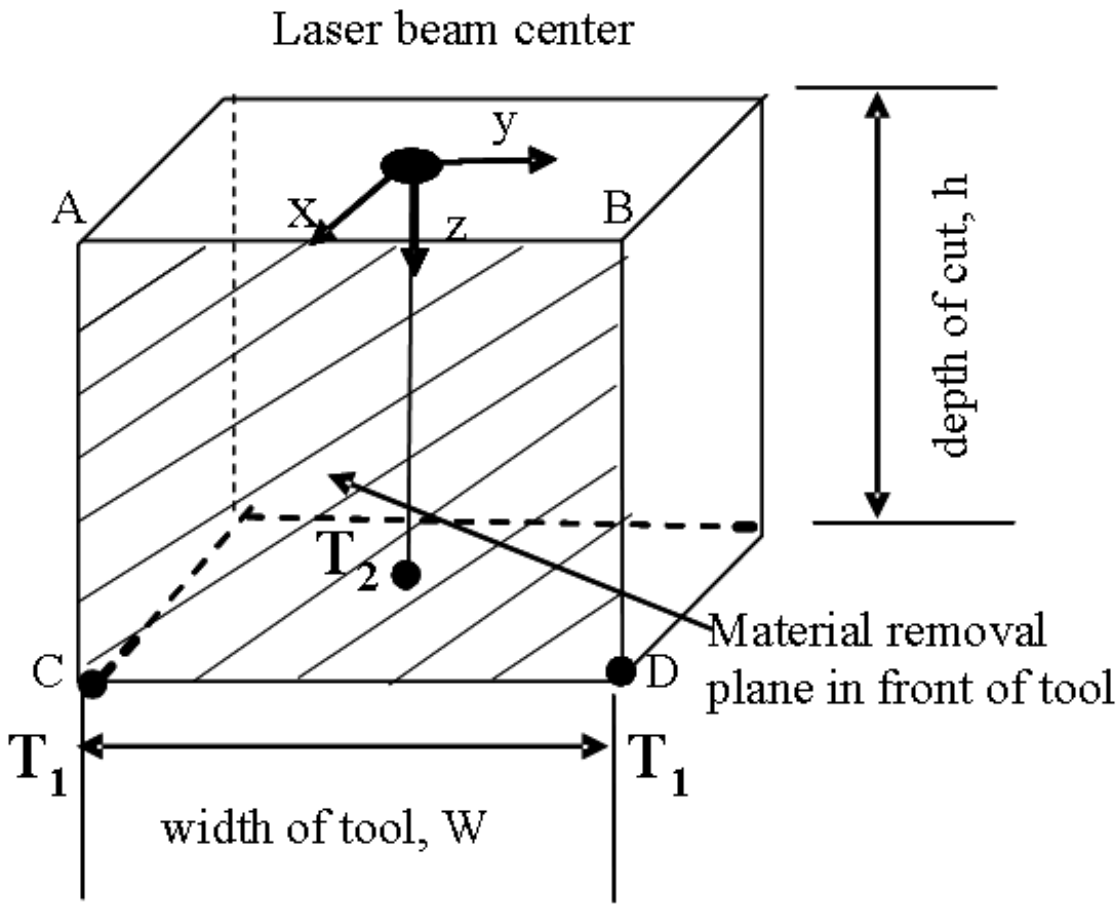

Figure 7.2: Location of relevant temperature points in the vicinity of tool

7.1.2 Force Model

As noted earlier, knowledge of machining forces in micro-cutting processes is necessary to determine the impact of cutting conditions on machine/tool/part deflections, dimensional accuracy of the micro feature, and on premature tool breakage. The overall methodology for prediction of the forces in laser assisted micro-grooving is described in Chapter 6. The key elements of the methodology consist of the thermal model of laser heating (discussed in the previous section and Chapter 5), a material model of the material flow strength [114], a slip-line field based geometric model of plastic deformation arising from chip formation [105], a force model derived from the slip-line field model [105], and a model for taking into account the influence of

machine/tool elastic deflection on the forces and depth of cut (see Chapter 6). The outputs of the complete model are the cutting and thrust forces and the actual (equilibrium) depth of cut. Accounting for the variation in the shear flow stress in the material removal plane, the total cutting and thrust forces can be approximated as follows:

$$F_c = \{(h-p)\,cot\phi + h + r_n sin\theta - (k-1)\,\delta\} \sum_{1}^{n} \bar{S}\,(i)\,w\,(i) \tag{7.1}$$

$$F_t = \{(h-p)\,cot\phi - h + r_n sin\theta + (k-1)\,\delta cot\psi\} \sum_{1}^{n} \bar{S}\,(i)\,w\,(i) \tag{7.2}$$

The development of Eq. 7.1 and Eq. 7.2 is described in detail in Chapter 6. The stacked stages of the miniature machine tool used in the micro-grooving setup developed in this thesis have a finite stiffness and therefore tend to deflect elastically under the influence of the forces. This deflection alters the depth of cut, which in turn affects the forces. The equilibrium static stiffness of the stacked stages in the depth of cut (X) direction is obtained from load-displacement tests as described in Chapter 4. The algorithm used to determine the equilibrium depth of cut, h and forces (F_c and F_t) with machine elastic deflection is described in Fig. 6.8 of Chapter 6 The inputs are the nominal depth of cut and the equilibrium static stiffness (k_{equil}) of the stacked machine tool stages in the depth of cut direction and the outputs are the equilibrium depth of cut and the cutting and thrust forces (F_c and F_t).

7.2 Experimental Work

To evaluate the fidelity of the force model, the predictions are compared with actual micro-grooving experiments carried out with a 300 μm wide grooving tool. The workpiece material used in these experiments is heat treated H-13 steel with hardness of 42±2 on the Rockwell C scale. A full factorial design of experiment was used to investigate the effects of laser and cutting parameters on the cutting forces and the

groove depth. The parameters and their values used in the experiment are shown in Table 7.1. The experimental design yielded a total of 48 test combinations and three replications per test were conducted. The measured responses are the cutting and thrust forces and the resulting groove depth. The groove depth was measured using a scanning white light interferometer-based surface profiler (Zygo NewView 200).

Table 7.1: Experimental Conditions

Depth of Cut (μm)	Tool Width (μm)	Cutting Speed (mm/min)	Laser Location (μm)	Laser Power (W)
10	300	10	100	0
15		50	200	5
20		100		10
25				

The measured forces averaged over the three replicates are plotted against the predicted forces and are shown in Fig. 7.3. The predictions will be exact if the points plot on the solid line. It can be seen that the engineering models are doing a reasonably good job in predicting the forces. However, there are some systematic errors: the cutting forces are under predicted and the thrust forces are slightly over predicted. This will be corrected by developing an engineering-statistical model.

7.3 Metamodels

The engineering models are computationally intensive, especially the finite element models, which can take many hours for simulating each test condition. Therefore, using them directly for optimizing the process variables can be computationally very expensive. Consequently, metamodels that approximates the complex engineering models are developed in the following sections to reduce computational time.

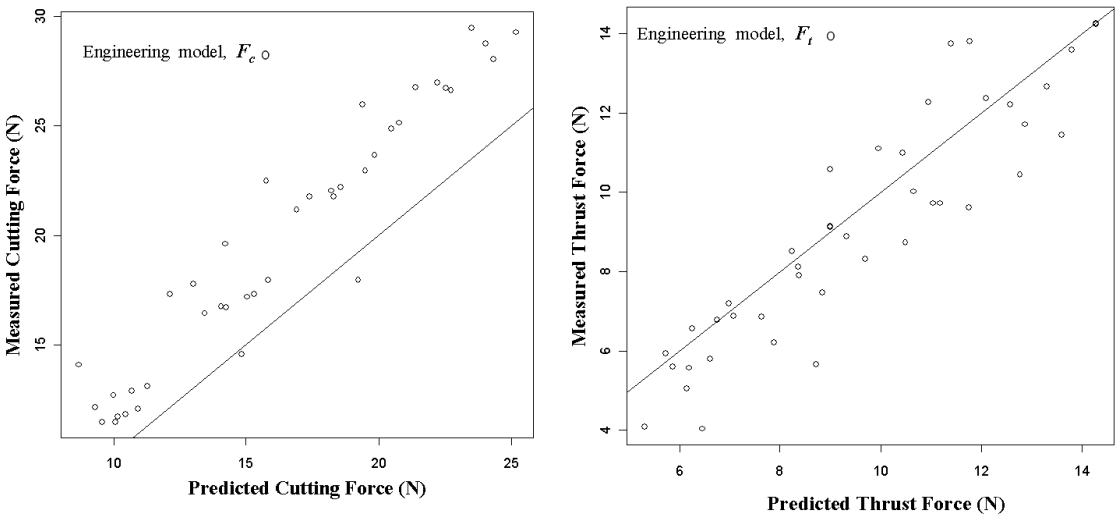

Figure 7.3: Plot of measured forces vs. predicted forces

7.3.1 Cutting/Thrust Force

The cutting and thrust forces are functions of the process variables. Fig. 7.4 shows the notations of the variables used in the model. The nominal (set) depth of cut is

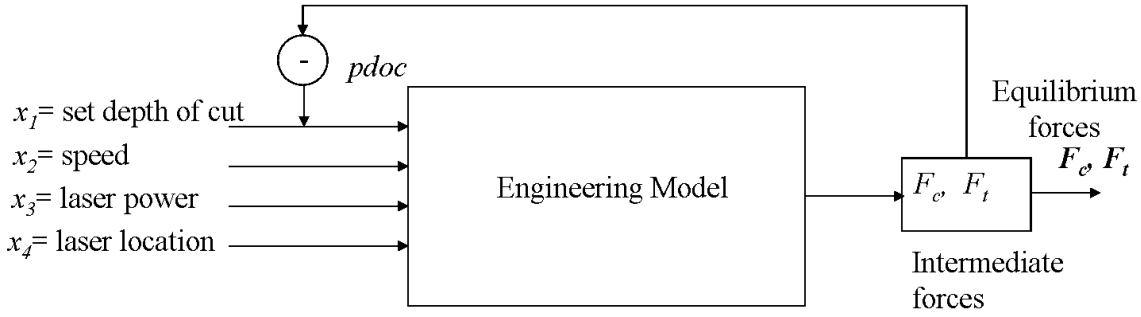

Figure 7.4: Process variables in metamodeling

altered due to machine deflection and therefore the input to the force model is the predicted depth of cut (*pdoc*) based on the algorithm shown in Fig. 6.8 of Chapter 6. The model development for the cutting force, F_c will be described first. The model can be written as:

$$F_c = f_c\left(pdoc, x_2, x_3, x_4\right) \tag{7.3}$$

Laser power (x_3) and laser location from the tool edge (x_4) have opposing influence on the thermal softening. A higher laser power induces increased thermal softening in the material removal plane whereas an increase in the distance between the laser and the tool will reduce thermal softening. Consequently, in the absence of laser heating ($x_3 = 0$) the laser beam location with respect to the tool edge (x_4) has no effect. Similarly, if the laser is located very far ($x_4 = \infty$) then the laser power will not induce any softening. Thus, a reduced model that captures this is given by:

$$F_c = f_c\left(pdoc, x_2, x_3 e^{-\lambda x_4}\right) \tag{7.4}$$

where λ is a positive constant. Now a model to approximate Eq. 7.4 can be postulated. Note that the cutting force should be 0 when $pdoc$=0. Moreover, the speed and laser power enter into the engineering model via the shear flow stress. Therefore, the following metamodel is considered:

$$F_c = pdoc^{\gamma}\beta_0\left(1 + \beta_1 x_2\right)\left(1 + \beta_2 x_3 e^{-\lambda x_4}\right) \tag{7.5}$$

where γ, β_0, β_1, β_2 and λ are unknown parameters in the model. Nonlinear regression is used for estimating the parameters and the metamodel is given by:

$$\hat{F}_c = pdoc^{0.845}1.871\left(1 + 0.0018 x_2\right)\left(1 - 0.0284 x_3 e^{-0.0032 x_4}\right) \tag{7.6}$$

The prediction obtained from the metamodel $\left(\hat{F}_c\right)$ is plotted against the prediction from the engineering model (F_c) in Fig. 7.5. It can be seen that they are in good agreement. The R^2 for the metamodel is 99.64%. The coefficient $\lambda = 0.0032$ indicates that moving the laser spot from the tool edge by 100 μm is equivalent to reducing the laser power by about $(1 - e^{-0.32}) \times 100 = 27\%$.

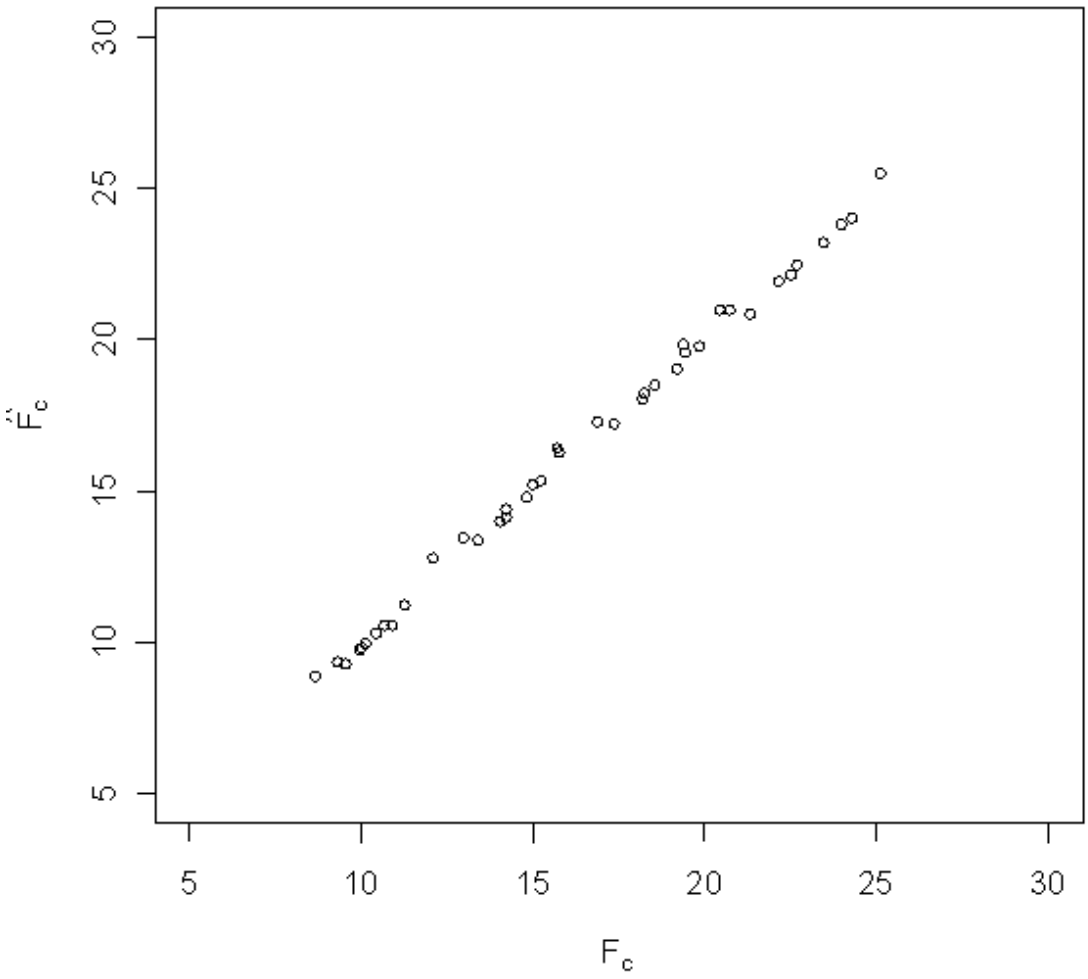

Figure 7.5: Metamodel vs. engineering model

Similarly, the metamodel for thrust force can be developed and is given by:

$$\hat{F}_t = pdoc^{0.758} 1.369 \left(1 + 0.0018 x_2\right) \left(1 - 0.0284 x_3 e^{-0.0032 x_4}\right) \tag{7.7}$$

The R^2 for this model is 99.43%. It is quite interesting to note that many of the coefficients in the two metamodels match, which reassures their validity.

A more popular way to develop metamodels is to use kriging as given by Sacks et al.

[115]. This is because the deterministic models are being approximated and therefore, interpolating models are more suitable for approximation. Although, kriging can give an interpolating metamodel, it is difficult to interpret and it may not agree with engineering intuition. On the other hand, the metamodel developed here using nonlinear regression has more engineering meaning. Moreover, the errors from the model are so small that these models will perform as good as any interpolating model.

7.3.2 Temperatures at T_1 and T_2

A metamodel is fit to the finite element temperature predictions at the extremities of the tool-workpiece interface, T_1, and the temperature below the laser spot at the intended depth of cut, T_2. Again, using nonlinear regression the following equations are obtained:

$$T_1 = 41.36 + 41.44x_3e^{-0.0018x_4} - 0.207x_2x_3e^{-0.0018x_4} \tag{7.8}$$

$$T_2 = 25 + 371.07x_3^{0.635} - 4.59pdocx_3^{0.635} - 0.939x_2x_3^{0.635} \tag{7.9}$$

The R^2 for the two models are 99.85% and 99.37%, respectively.

7.4 Engineering-Statistical Models

As discussed before, the engineering-statistical modeling method employs statistical techniques to improve the accuracy of predictions obtained from the engineering model and consequently it is expected that the predictions from this new model will be closer to the reality. Joseph and Melkote [112] proposed a Bayesian approach to develop engineering-statistical models. Here a frequentist version of their approach is used, mainly for simplicity. The two approaches are expected to produce similar results, because a large sample of observations for fitting the models is available. The engineering-statistical models presented below employ constant adjustment model

[112] to improve the predictions from engineering metamodels (see Eqs. 7.6 and 7.7). The engineering-statistical models are given by:

$$\hat{y_c} = \hat{F_c}\left(1.15 + 0.017x_3e^{-0.0032x_4}\right) \tag{7.10}$$

$$\hat{y_t} = \hat{F_t}\left(1.01 - 0.014x_3e^{-0.0032x_4}\right) \tag{7.11}$$

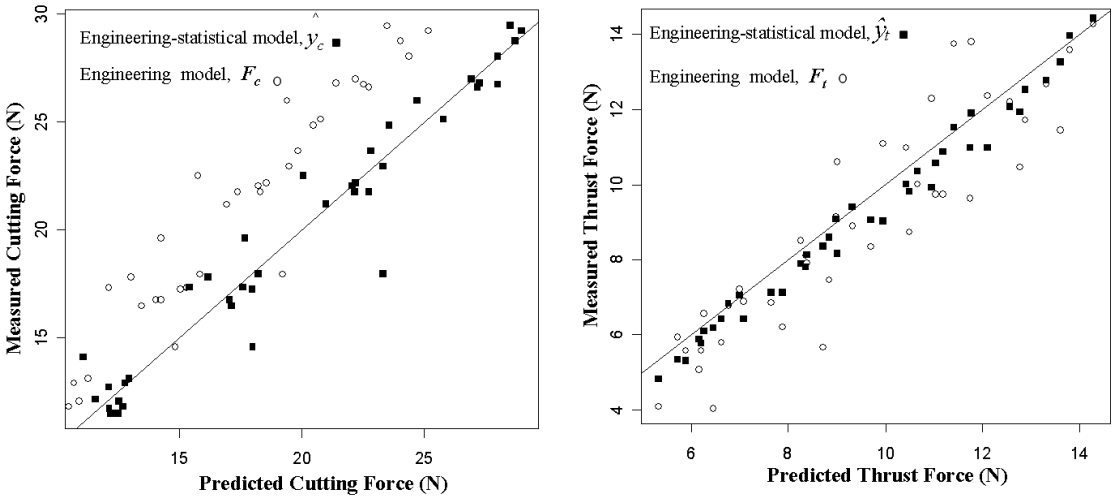

Figure 7.6: Plot of predicted vs. measured cutting and thrust forces

Fig. 7.6 shows the improvement in prediction due to the engineering-statistical model. The circles in the plots indicate the cutting and thrust force predictions from the engineering models while the solid squares are the predictions from the engineering-statistical model. It can be clearly seen that the engineering statistical model is much closer to measured values. This shows that the engineering-statistical model is more accurate than the pure engineering model. The improvement in prediction can be quantified using the mean squared error (MSE). For the cutting force engineering-statistical model, the MSE can be computed as:

$$MSE = \frac{1}{48}\sum_{i=1}^{48}\left(y_{ci} - \hat{y_{ci}}\right)^2 = 1.701 \tag{7.12}$$

Whereas the MSE from the engineering model predictions is 14.02. Thus, the prediction errors are reduced by about 88% by using the engineering-statistical model. Similarly, the MSEs for the thrust force predictions after and before the statistical adjutments are 1.36 and 1.57, respectively, which represents about 13% improvement. Thus ,the improvement in predictions using the engineering-statistical approach is much more significant in the case of cutting force compared to the thrust force.

The predicted depth of cut based on the algorithm presented in Fig. 6.8 of Chapter 6 can also be improved by using the engineering-statistical approach. The engineering-statistical model for the actual depth of cut ($adoc$) is given by:

$$adoc = pdoc\left(0.848 + 0.034x_3e^{-0.0032x_4}\right) \tag{7.13}$$

7.5 Optimization

The engineering-statistical models developed in the previous section are used for optimization. The objective is to select optimal settings for the parameters for a prescribed feature size without any residual HAZ while minimizing the cutting and thrust forces. Mathematically, it can be stated as,

Minimize: $\hat{y_c}$, $\hat{y_t}$ and T_2

Maximize: T_1

The above optimization will be carried out for a given depth of cut using the following process variables:

- Cutting speed (x_2): range = 10 mm/min - 50 mm/min
- Laser power (x_3): range = 0 W - 10 W
- Laser location from the tool edge (x_4): range = 100 μm - 200 μm

A test case is demonstrated for a desired feature size of 10 μm. Substituting 10 μm as the actual depth of cut, $adoc$, in Eq. 7.13, the predicted depth of cut can be calculated as,

$$pdoc = \frac{10}{(0.848 + 0.034 x_3 e^{-0.0032 x_4})} \tag{7.14}$$

Now the cutting force ($\hat{y_c}$), thrust force ($\hat{y_t}$), and the temperatures (T_1 and T_2) can be calculated using Eq. 7.10, Eq. 7.11, Eq. 7.8 and Eq. 7.9, respectively. The calculations are done over a grid of values for the process variables. The objective function is aimed at minimizing the cutting/thrust forces and temperature T_2 as well as maximizing the temperature T_1 in the material removal plane to ensure softening. It is expected that a higher temperature in the material removal plane will result in lower cutting and thrust forces. Fig. 7.7 shows the plot of $\hat{y_t}$ vs. T_1. It can be see that the lower the $\hat{y_t}$ the higher the T_1 value. This indicates that if $\hat{y_t}$ is minimized T_1 will be maximized. Similar results are observed for $\hat{y_c}$ as well. Thus, if we choose minimum $\hat{y_c}$ and $\hat{y_t}$ subject to a value of T_2 which avoids HAZ, it will guarantee maximum T_1 as well for those conditions.

Fig. 7.8 and Fig. 7.9 show the temperature T_2 as a function of the thrust force, $\hat{y_t}$, and cutting force, $\hat{y_c}$, respectively. The data points which indicate the lowest force are to the leftmost side of the plot and they form the Pareto frontier for the given system. A point in the Pareto frontier should be chosen depending on the specific requirements of that system. In order to get the lowest force and avoid transformation in H-13 steel, the point lying on the Pareto frontier right below the Ac_1 (horizontal line in Fig. 7.8 and Fig. 7.9) is selected. The optimal point for 10 μm intended depth of cut has the same solution for both cutting and thrust forces and corresponds to the following values:

- Depth of Cut (x_1) = 13.28 μm
- Cutting speed (x_2) = 10 mm/min
- Laser power (x_3): range = 4 W
- Laser location from the tool edge (x_4) = 100 μm

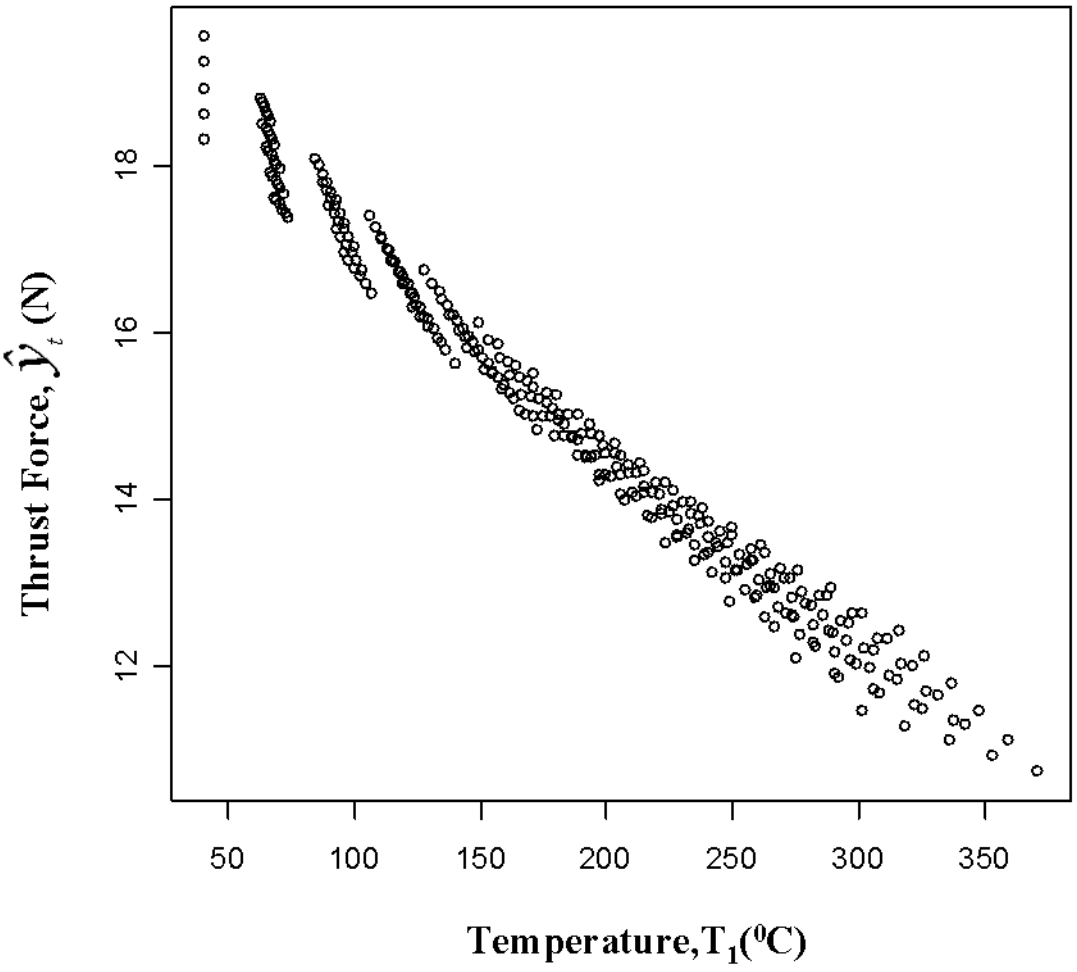

Figure 7.7: Plot of T_1 vs. $\hat{y}_t$

If the optimal solutions for cutting and thrust forces are not the same, the solution corresponding to the minimum thrust force will be considered because the thrust force directly affects the deflection in the micro-grooving operation. The optimal solution thus obtained needs to be validated experimentally for the microstructure/hardness and the measured feature size, which is presented in the following section.

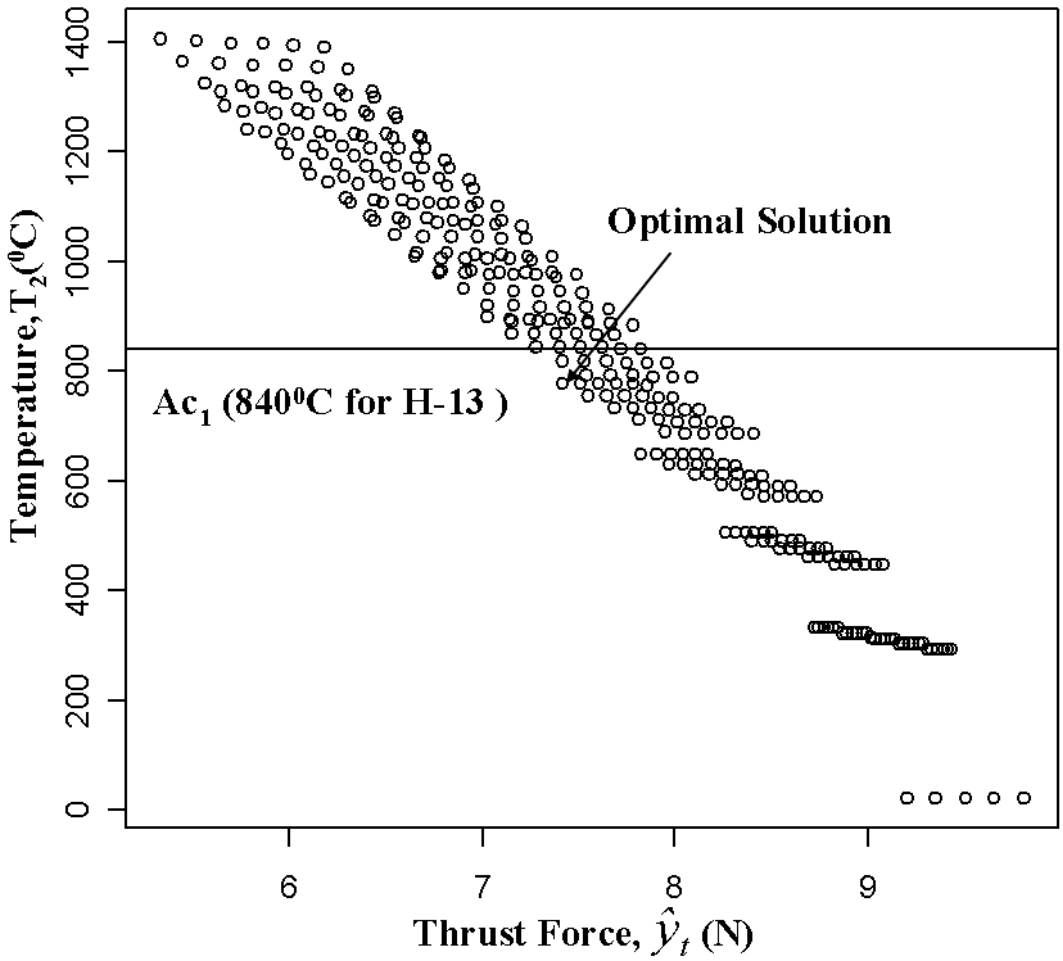

Figure 7.8: Plot of thrust force, $\hat{y}_t$, and temperature, T_2

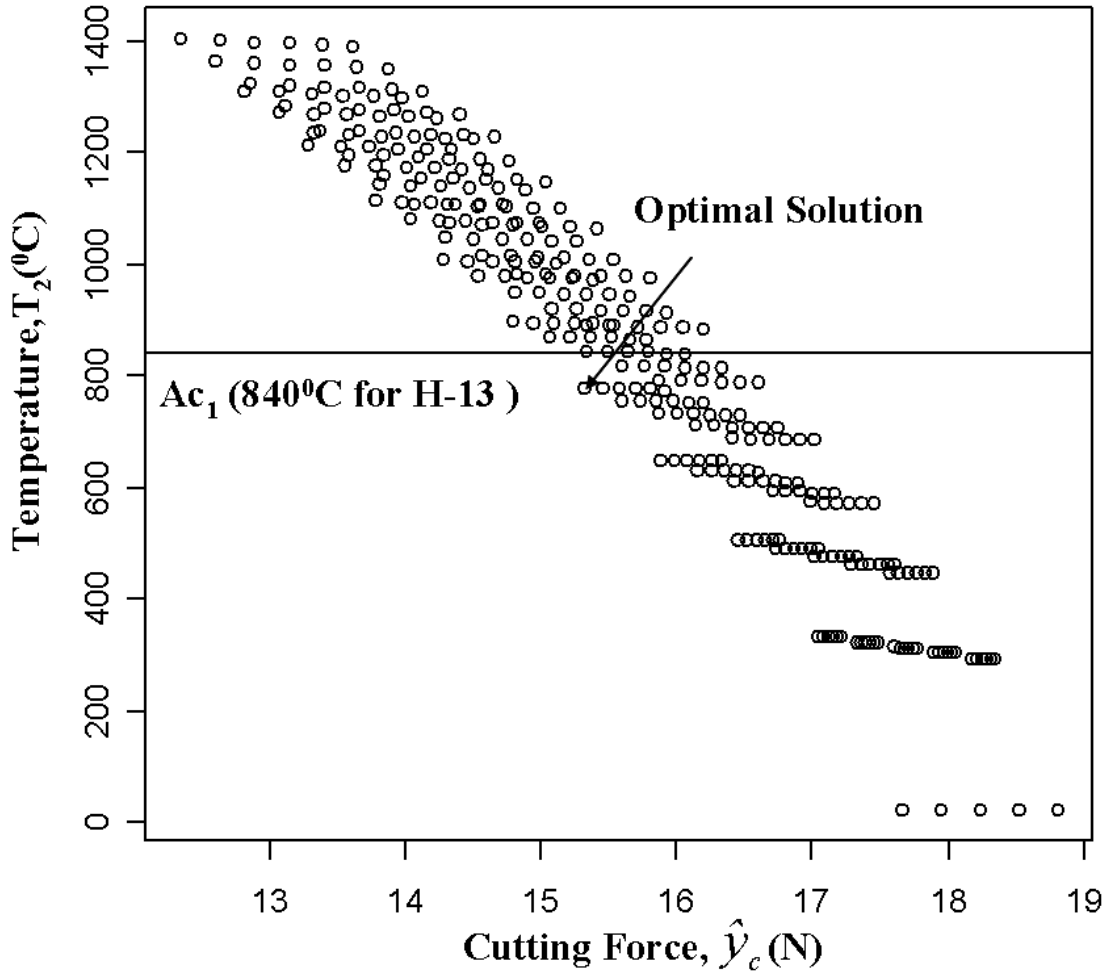

Figure 7.9: Plot of cutting force, $\hat{y}_c$, and temperature, T_2

7.6 Experimental Validation

Two desired feature sizes (10 μm and 25 μm) were considered for validation. In addition to the validation with respect to the measured feature size, microstructure/hardness and cutting/thrust forces required to create a desired feature size are evaluated (via the model and experiments) with optimal laser and cutting parameters and without laser (for the same cutting parameters) to quantify the effect of thermal softening. The optimal solution for the 25 μm feature size is:

- Depth of Cut (x_1) = 28.82 μm

- Cutting speed (x_2) = 50 mm/min
- Laser power (x_3): range = 8 W
- Laser location from the tool edge (x_4) = 100 μm

7.6.1 Feature Size Measurement

Fig. 7.10 (a) and (b) show the profiles of the cut grooves produced at the optimal cutting conditions for the 10 μm and 25 μm desired feature sizes, respectively. The upper trace in each graph of Fig. 7.10 shows the groove profile created by the clean up pass used to remove the laser burn marks generated during laser positioning and alignment. This profile represents the initial condition and is marked "'before machining"'. The lower trace represents the machined groove depth (the actual depth of cut is the difference between the two traces) and is labeled "'after machining"' in the graphs. It can be seen that the measured groove depths are in good agreement with the desired feature size.

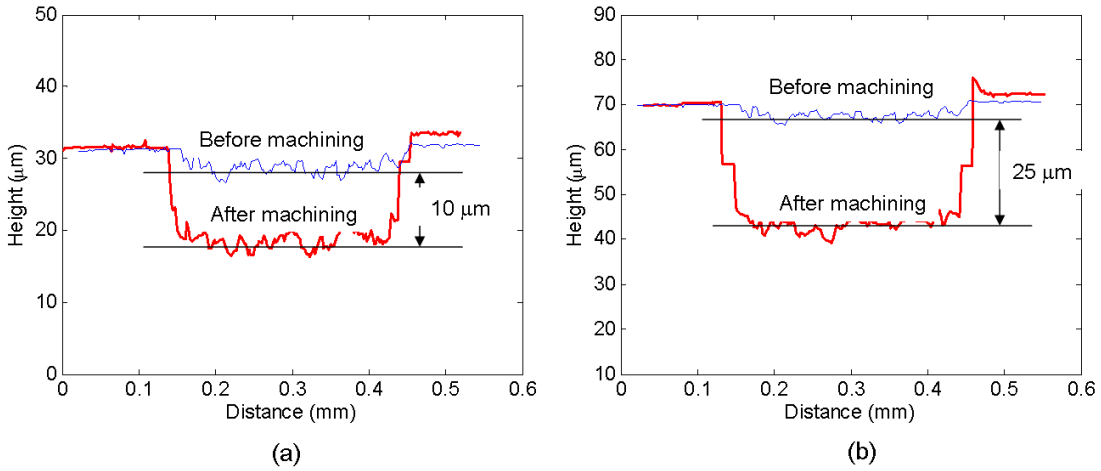

Figure 7.10: Measured groove dimensions: (a) 10 μm feature size; (b) 25 μm feature size

7.6.2 Cutting/Thrust Force Validation

Fig. 7.11 and Fig. 7.12 show the comparison of the experimental and predicted cutting and thrust forces, respectively, for feature sizes of 10 μm and 25 μm,

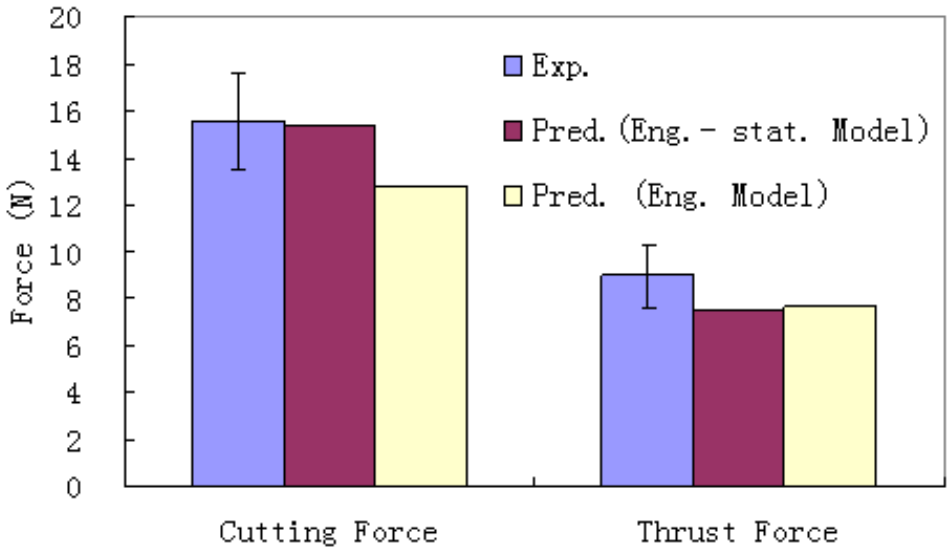

Figure 7.11: Experimental and predicted forces for 10 μm feature size

The cutting force prediction errors are less that 1% but the thrust force errors are slightly higher at 16% for 10 μm desired feature size. It is clear that there is a significant improvement in the prediction errors with the engineering-statistical model for the cutting force. The cuuting and thrust force prediction errors for the engineering model alone at 10 μm nominal depth of cut, 10 mm/min cutting speed and 4 W laser power are 18% and 15%, respectively. Similarly, the cutting force prediction errors with the engineering-statistical model are better than the engineering model for the 25 μm desired feature size. The prediction errors with the engineering-statistical model is less that 3% for the cutting force but the thrust force errors are slightly higher at 18% for the 25 μm desired feature size.

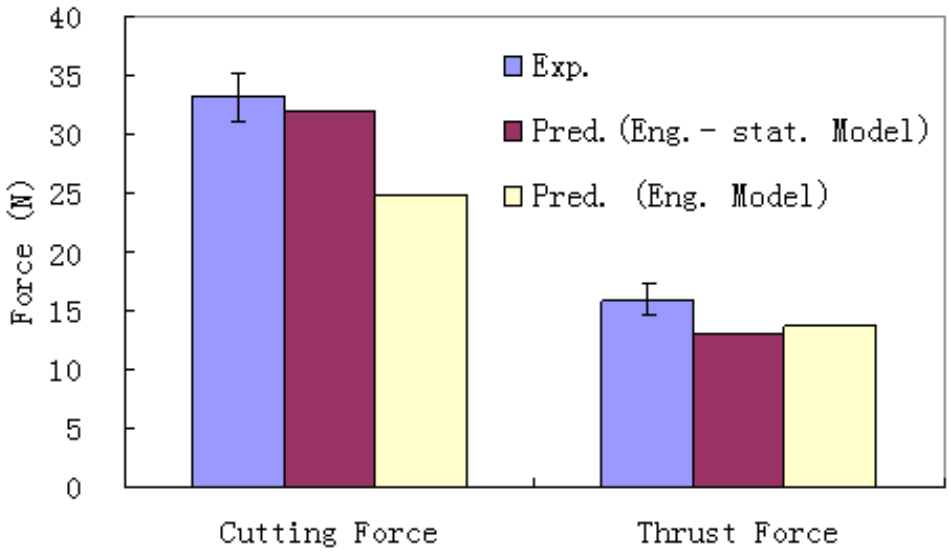

Figure 7.12: Experimental and predicted forces for 25 μm feature size

7.6.3 Microstructure/Hardness Evaluation

The cross-section of the machined surface was analyzed for increase in hardness and/or microstructural changes related to residual HAZ. Fig. 7.13 shows the microstructure of the machined groove cross-section and the area close to the base of the groove where the hardness is measured.

Any change in micro-hardness near the base of the groove indicates that the microstructure in that area has changed. Micro hardness tests were conducted in the area shown in Fig. 7.13 near the base of the groove and the hardness values were close to the bulk hardness of 42$\pm$2 HRC as shown in Fig. 7.14. These results demonstrate that there are no microstructural changes below the machined surface for both the 10 μm and 25 μm feature size.

7.6.4 Effect of Laser Heating on Forces

In order to investigate the effect of thermal softening and, consequently, reduction in cutting forces, the cutting forces obtained for optimal conditions to yield a desired

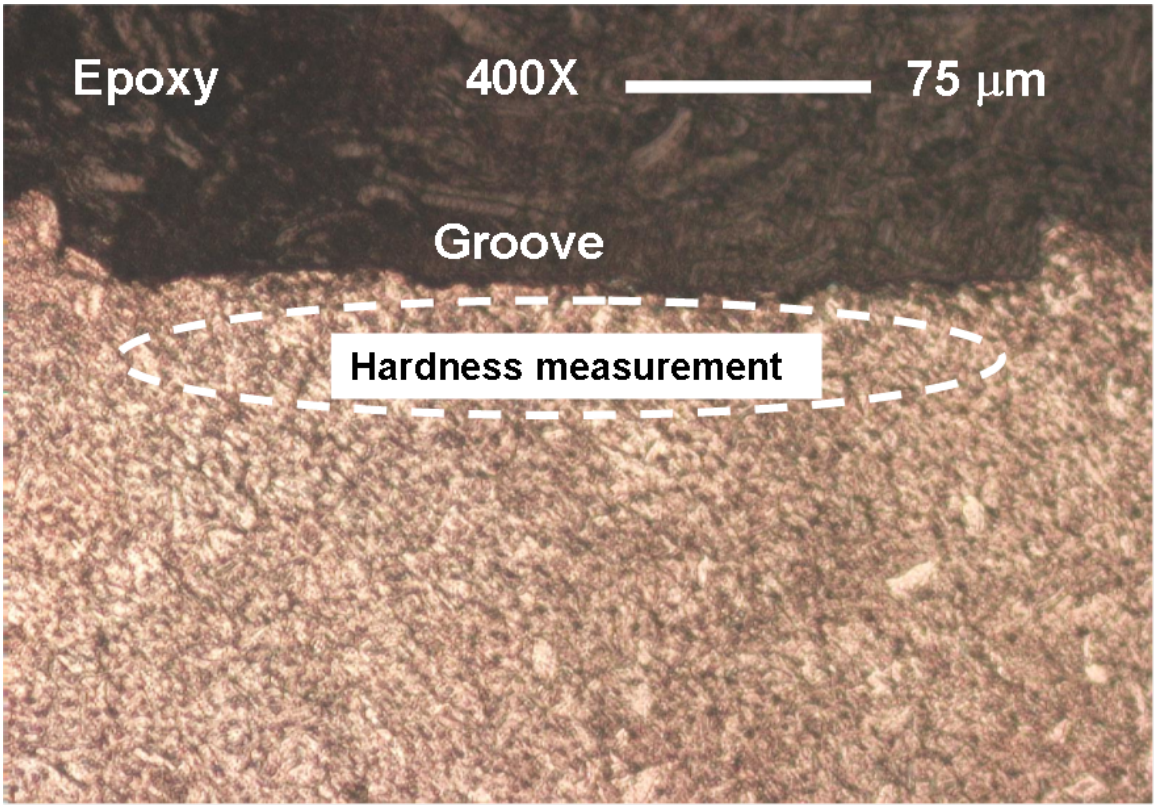

Figure 7.13: Microstructure of the cross-section of test cut with 300 μm grooving tool at 8 W laser power and 50 mm/min cutting speed, 100 μm laser-tool distance and 25 μm feature size

feature size of 25 μm are compared with cutting forces for the same feature size without laser heating and same cutting parameters. It is of interest to see if appreciable change is observed as a result of laser heating while avoiding the heat affected zone in the machined surface. The model predicts that in the absence of laser heating a nominal depth of cut of 36 μm will be required to obtain a desired feature size of 25 μm at 50 mm/min cutting speed. The dimensions of the groove are shown in Fig. 7.15 which shows that the desired depth of cut is predicted accurately by the model.

Fig. 7.16 shows the cutting and thrust forces with and without laser. The experimental reduction cutting and thrust forces are 22% and 29% respectively. The model predicts a drop of 22% in both cutting and thrust forces. This shows that thermal appreciable thermal softening can be achieved without inducing a heat affected zone

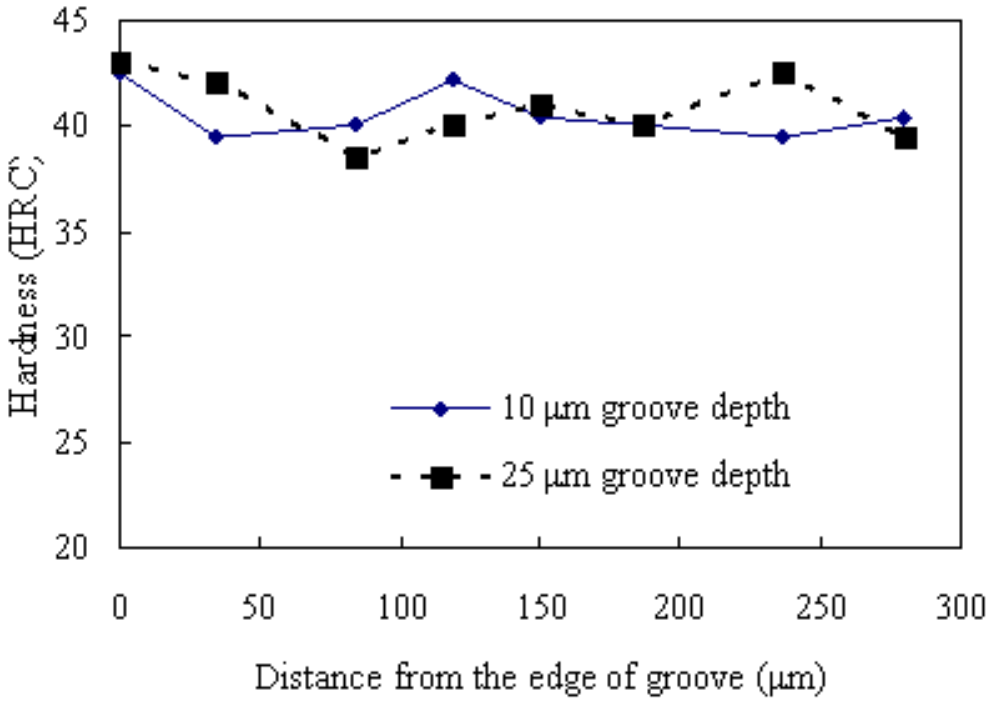

Figure 7.14: Hardness measurement

in the machined surface.

7.7 Summary

This chapter presented an optimization technique for the LAMM based micro-grooving process. The optimization approach is shown to yield a desired feature size without inducing a heat affected zone in the residual machined surface. The current work is built on the engineering models for temperature distribution and cutting force prediction presented previously in Chapter 5 and Chapter 6. Engineering-statistical models have been successfully developed to improve these predictions. The following specific conclusions can be drawn from the work presented in this chapter:

- An engineering-statistical model developed to fit the engineering model as an explicit function of the input process variables with significant improvement in

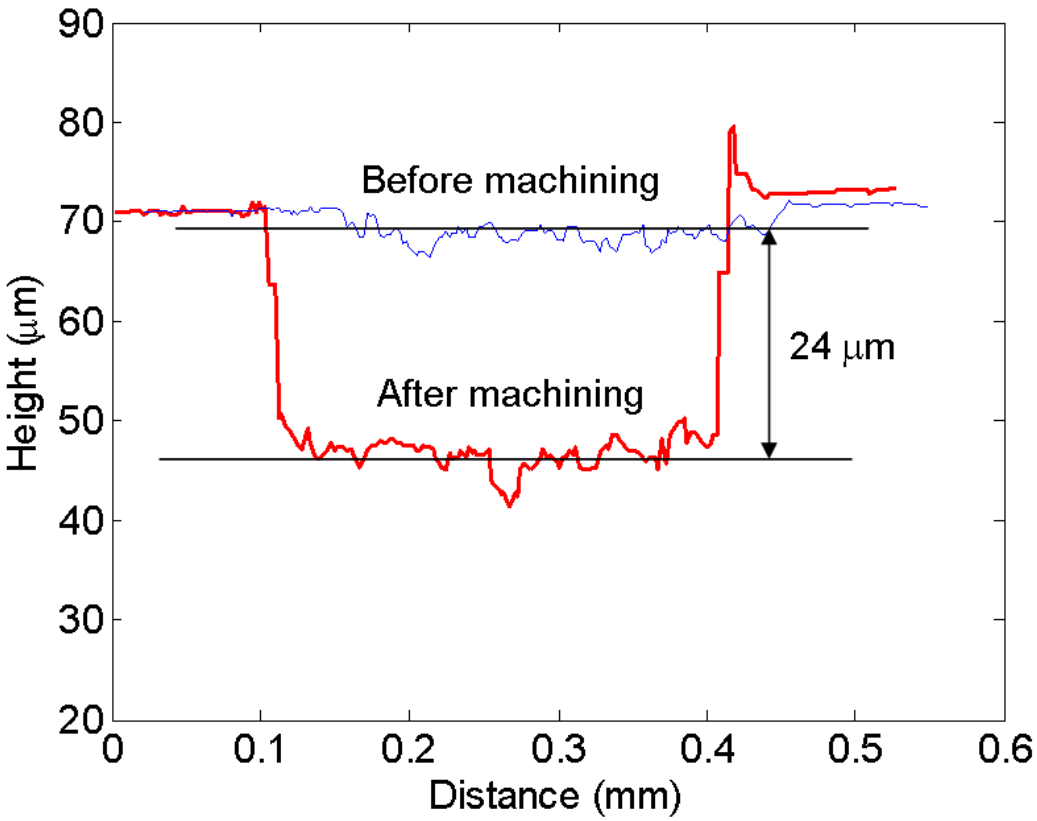

Figure 7.15: Measured groove dimensions for 25 μm desired feature size without laser heating

the predictions. The mean square error in the cutting force prediction is reduced from 14.7 of the engineering model to 1.79 for the engineering-statistical model.

- The measured cutting forces and thrust forces are within 3% and 18% of the predicted values using engineering-statistical models, respectively, for the optimal conditions.

- The measured feature size is predicted accurately by the engineering-statistical model of the actual depth of cut.

- There is a significant force reduction ($\sim$ 22%) with laser heating compared to without laser heating for generating the same feature size keeping all other

cutting parameters constant.

Figure 7.16: Measured and predicted cutting and thrust forces at 0 W and 8 W laser powers and 50 mm/min cutting speed for a desired feature size of 25 μm

CHAPTER VIII

CONCLUSIONS AND RECOMMENDATIONS

This chapter summarizes the conclusions of this thesis and suggests related areas for further exploration.

8.1 Main Conclusions

The main conclusions of this thesis work are as follows:

8.1.1 Experimental Characterization of the LAMM Process

The study revealed that machine stiffness and thermal expansion of the tool can affect the actual depth of cut in the LAMM-based micro-grooving process. The following specific conclusions can be drawn from the experimental study:

- Thermal softening can be induced by laser heating and up to 56% and 46% reduction in the cutting and thrust forces, respectively, are observed with 35 W laser heating when microcutting H-13 steel (42 HRC).
- Decrease in the cutting force with laser heating is not always observed because of an increase in the actual depth of cut due to smaller stage deflection (as a result of lower thrust forces) and thermal expansion of the tool at low laser powers ($\leq$ 10 W).
- Laser induced thermal softening improves the accuracy of the groove depth by reducing the stage deflection (due to lower thrust force).
- Laser power appears to significantly affect the surface roughness in the LAMM process; an increase of up to 36% is observed in the current study.

8.1.2 Characterization and Prediction of the Heat Affected Zone

The HAZ produced by laser heating in the LAMM based micro-grooving process has been characterized via metallography and micro-hardness tests. A thermal model has been developed to predict the extent of HAZ. The following conclusions summarize the work:

- The size of the HAZ depends on the laser scanning speed and laser power. The maximum width and depth of the HAZ decrease by 32% and 62%, respectively, when the scan speed is increased from 10 mm/min to 100 mm/min at a laser power of 10 W.
- A transient 3-D finite element model for a moving Gaussian circular beam has been developed to analyze the temperatures within the HAZ. The model predicts the temperature to within 15% of the measured temperatures.
- A critical temperature range (840∼890℃) corresponding to the depth of the HAZ produced in H-13 steel (42 HRC) at different scan speeds was identified. If the temperature in the material removal region is below the critical range then there will be no residual HAZ in the material after micro cutting.
- The thermal model can aid in selection of laser parameters to avoid residual HAZ in the machined surface.

8.1.3 Force Modeling in Laser-Assisted Micro-grooving

A slip-line field based force model has been developed which captures the effects of thermal softening, edge radius of the tool and compliance of the machine stages. This model predicts the cutting and thrust forces and feature size with reasonable accuracy. The following conclusions summarize the work:

- The force model for the laser-assisted micro-grooving process captures the observed trends accurately. The model prediction errors are less than 20% in most

cases.

- The model predicts the actual depth of cut to within 4 to 10% of the measured values.

- The model can predict the shear stress distribution resulting from thermal softening in the material removal plane. A 66% reduction in the shear flow stress of H-13 steel (42 HRC) is observed for 35 W laser power.

- The model captures the effect of thermal softening as a result of increase in laser power and up to 48% reduction in the cutting and thrust forces is observed for H-13 steel (42 HRC) at 35 W laser power.

- The model captures the observed trends for the effect of cutting speed.

8.1.4 Process Optimization

A robust process optimization methodology has been developed for the laser-assisted micro-grooving process to obtain a desired feature size without inducing a heat affected zone in the residual machined surface. The following specific conclusions can be drawn:

- An engineering-statistical model developed to fit the engineering model as explicit function of the input process variables shows significant improvement in prediction over the engineering model.

- The measured cutting forces and thrust forces H-13 steel (42 HRC) are within 3% and 18% of the predicted values, respectively, for the optimal conditions.

- The measured feature size is predicted accurately by the engineering-statistical model of the actual depth of cut.

8.2 Further Investigations

Related areas for further research include the following:

- Investigation of tool wear and tool life in LAMM processes is important as high temperatures are known to accelerate the tool wear and consequently devising strategies to reduce tool wear will enhance the process capability.

- The current LAMM setup can generate simple 2-D features. Adaptation of the LAMM idea to micro-milling can help create complex 3-D sculpted surface in hard-to-machine materials. Other hybrid processes such as laser-assisted micro-turning can also be explored.

- The current work is focused on H-13 tool steel. Studies on other hard-to-machine metallic and non-metallic materials such as titanium and nickel-based alloys, sintered ceramics, and ceramic matrix composites can be conducted.

- The LAMM setup can be designed to serve as platform for post machining operations, such as, surface hardening, surface activation to improve biocompatiblity and creating surface textures to enhance tribological performance.

APPENDIX A

SUPPORTING DATA

Table A.1: Experimental data for full factorial design of experiments

Depth of Cut (Level)	Laser Location (Level)	Tool Width (Level)	Cutting Speed (Level)	Laser Power (Level)	Cutting Force $\mu \pm \sigma$ (N)	Thrust Force $\mu \pm \sigma$ (N)	Surface Roughness $\mu \pm \sigma$ (μm)
0	0	0	0	0	12.08 ± 0.54	6.80 ± 0.51	0.69 ± 0.067
0	0	0	0	1	12.73 ± 0.61	5.07 ± 0.13	0.78 ± 0.024
0	0	0	0	2	14.13 ± 0.38	4.10 ± 0.28	1.07 ± 0.096
0	0	0	1	0	13.12 ± 0.55	7.21 ± 0.70	0.66 ± 0.121
0	0	0	1	1	11.84 ± 0.23	4.06 ± 0.58	0.56 ± 0.103
0	0	0	1	2	19.20 ± 1.15	7.27 ± 0.95	0.85 ± 0.032
0	0	1	0	0	15.44 ± 1.15	10.91 ± 1.04	0.66 ± 0.152
0	0	1	0	1	20.66 ± 0.84	11.31 ± 0.31	0.92 ± 0.003
0	0	1	0	2	20.92 ± 2.46	9.46 ± 0.41	0.81 ± 0.048
0	0	1	1	0	16.76 ± 0.67	10.55 ± 0.43	0.72 ± 0.121
0	0	1	1	1	17.67 ± 0.11	8.67 ± 0.29	0.88 ± 0.123

Continued on next page

Table A.1 – continued from previous page

Depth of Cut (Level)	Laser Location (Level)	Tool Width (Level)	Cutting Speed (Level)	Laser Power (Level)	Cutting Force $\mu \pm \sigma$ (N)	Thrust Force $\mu \pm \sigma$ (N)	Surface Roughness $\mu \pm \sigma$ (μm)
0	0	1	1	2	18.86 ± 0.59	8.29 ± 0.43	0.90 ± 0.089
0	1	0	0	0	12.08 ± 0.54	6.80 ± 0.51	0.69 ± 0.067
0	1	0	0	1	11.75 ± 2.22	6.58 ± 0.97	0.85 ± 0.099
0	1	0	0	2	12.16 ± 1.27	5.93 ± 0.12	1.06 ± 0.160
0	1	0	1	0	13.12 ± 0.55	7.21 ± 0.70	0.66 ± 0.121
0	1	0	1	1	12.93 ± 2.18	5.82 ± 0.55	1.18 ± 0.172
0	1	0	1	2	11.51 ± 0.23	5.60 ± 0.29	0.95 ± 0.111
0	1	1	0	0	15.44 ± 1.15	10.91 ± 1.04	0.66 ± 0.152
0	1	1	0	1	19.54 ± 1.01	10.25 ± 0.49	0.75 ± 0.061
0	1	1	0	2	21.72 ± 0.62	10.76 ± 0.19	0.98 ± 0.076
0	1	1	1	0	16.76 ± 0.67	10.55 ± 0.43	0.72 ± 0.121
0	1	1	1	1	16.89 ± 0.28	9.04 ± 0.11	0.76 ± 0.114
0	1	1	1	2	20.68 ± 1.68	10.67 ± 0.81	0.80 ± 0.118

Continued on next page

Table A.1 – continued from previous page

Depth of Cut (Level)	Laser Location (Level)	Tool Width (Level)	Cutting Speed (Level)	Laser Power (Level)	Cutting Force $\mu \pm \sigma$ (N)	Thrust Force $\mu \pm \sigma$ (N)	Surface Roughness $\mu \pm \sigma$ (μm)
1	0	0	0	0	17.34 ± 0.24	9.14 ± 0.18	0.70 ± 0.071
1	0	0	0	1	20.13 ± 0.17	8.51 ± 0.34	0.71 ± 0.076
1	0	0	0	2	17.33 ± 0.74	6.90 ± 0.75	0.87 ± 0.115
1	0	0	1	0	17.97 ± 1.97	8.90 ± 1.28	0.69 ± 0.020
1	0	0	1	1	14.59 ± 0.05	5.68 ± 0.39	0.75 ± 0.072
1	0	0	1	2	16.47 ± 0.71	6.22 ± 0.35	0.74 ± 0.006
1	0	1	0	0	22.72 ± 0.62	13.25 ± 0.35	0.70 ± 0.013
1	0	1	0	1	29.99 ± 0.69	12.63 ± 0.34	1.11 ± 0.158
1	0	1	0	2	25.79 ± 2.65	10.76 ± 0.51	1.14 ± 0.307
1	0	1	1	0	24.13 ± 0.79	13.67 ± 0.75	0.74 ± 0.039
1	0	1	1	1	22.53 ± 0.07	9.17 ± 0.32	0.97 ± 0.060
1	0	1	1	2	28.30 ± 0.57	11.53 ± 0.42	1.09 ± 0.049
1	1	0	0	0	17.34 ± 0.24	9.14 ± 0.18	0.70 ± 0.071

Continued on next page

Table A.1 – continued from previous page

Depth of Cut (Level)	Laser Location (Level)	Tool Width (Level)	Cutting Speed (Level)	Laser Power (Level)	Cutting Force $\mu \pm \sigma$ (N)	Thrust Force $\mu \pm \sigma$ (N)	Surface Roughness $\mu \pm \sigma$ (μm)
1	1	0	0	1	16.76 ± 1.63	7.92 ± 0.80	1.03 ± 0.085
1	1	0	0	2	17.81 ± 1.81	6.87 ± 0.08	1.14 ± 0.104
1	1	0	1	0	17.97 ± 1.97	8.90 ± 1.28	0.69 ± 0.020
1	1	0	1	1	17.23 ± 1.43	7.47 ± 0.48	1.12 ± 0.135
1	1	0	1	2	19.64 ± 1.85	8.13 ± 0.66	1.19 ± 0.082
1	1	1	0	0	22.72 ± 0.62	13.25 ± 0.35	0.70 ± 0.013
1	1	1	0	1	25.60 ± 2.11	14.37 ± 0.95	0.75 ± 0.070
1	1	1	0	2	27.74 ± 0.36	13.99 ± 0.57	1.04 ± 0.077
1	1	1	1	0	24.13 ± 0.79	13.67 ± 0.75	0.74 ± 0.039
1	1	1	1	1	27.57 ± 2.82	13.47 ± 0.89	0.80 ± 0.172
1	1	1	1	2	25.87 ± 1.99	12.53 ± 1.49	1.07 ± 0.124
2	0	0	0	0	23.68 ± 0.32	13.75 ± 0.03	0.65 ± 0.099
2	0	0	0	1	22.08 ± 1.63	11.00 ± 0.40	0.75 ± 0.037

Continued on next page

Table A.1 – continued from previous page

Depth of Cut (Level)	Laser Location (Level)	Tool Width (Level)	Cutting Speed (Level)	Laser Power (Level)	Cutting Force $\mu \pm \sigma$ (N)	Thrust Force $\mu \pm \sigma$ (N)	Surface Roughness $\mu \pm \sigma$ (μm)
2	0	0	0	2	22.52 ± 1.85	10.60 ± 0.20	0.95 ± 0.094
2	0	0	1	0	24.88 ± 1.01	13.81 ± 1.83	0.72 ± 0.134
2	0	0	1	1	17.99 ± 0.41	8.46 ± 0.28	0.80 ± 0.031
2	0	0	1	2	22.27 ± 0.46	11.10 ± 0.01	1.04 ± 0.116
2	0	1	0	0	30.74 ± 0.46	14.22 ± 2.38	0.65 ± 0.084
2	0	1	0	1	32.36 ± 2.08	15.96 ± 0.82	0.98 ± 0.197
2	0	1	0	2	33.11 ± 0.55	16.57 ± 0.22	1.15 ± 0.281
2	0	1	1	0	35.33 ± 1.41	18.33 ± 0.17	0.77 ± 0.094
2	0	1	1	1	32.96 ± 1.27	14.62 ± 0.43	0.81 ± 0.062
2	0	1	1	2	29.06 ± 0.80	12.18 ± 0.50	1.15 ± 0.104
2	1	0	0	0	23.68 ± 0.32	13.75 ± 0.03	0.65 ± 0.099
2	1	0	0	1	22.22 ± 1.45	10.03 ± 0.24	0.84 ± 0.065
2	1	0	0	2	21.19 ± 0.83	8.35 ± 0.22	0.99 ± 0.077

Continued on next page

Table A.1 – continued from previous page

Depth of Cut (Level)	Laser Location (Level)	Tool Width (Level)	Cutting Speed (Level)	Laser Power (Level)	Cutting Force $\mu \pm \sigma$ (N)	Thrust Force $\mu \pm \sigma$ (N)	Surface Roughness $\mu \pm \sigma$ (μm)
2	1	0	1	0	24.88 ± 1.01	13.81 ± 1.83	0.72 ± 0.134
2	1	0	1	1	22.96 ± 0.10	9.74 ± 0.26	0.89 ± 0.042
2	1	0	1	2	21.80 ± 1.08	8.74 ± 0.35	1.00 ± 0.094
2	1	1	0	0	30.74 ± 0.46	14.22 ± 2.38	0.65 ± 0.084
2	1	1	0	1	29.75 ± 0.57	16.07 ± 0.29	0.77 ± 0.035
2	1	1	0	2	33.38 ± 1.77	15.77 ± 0.77	0.96 ± 0.051
2	1	1	1	0	35.33 ± 1.41	18.33 ± 0.17	0.77 ± 0.094
2	1	1	1	1	30.53 ± 2.91	14.01 ± 1.41	0.73 ± 0.098
2	1	1	1	2	33.21 ± 2.43	15.14 ± 1.13	1.06 ± 0.052
3	0	0	0	0	28.06 ± 0.43	13.60 ± 0.18	0.80 ± 0.026
3	0	0	0	1	29.75 ± 0.37	12.22 ± 0.72	0.76 ± 0.047
3	0	0	0	2	31.79 ± 1.72	12.29 ± 0.34	1.11 ± 0.076
3	0	0	1	0	29.28 ± 0.37	14.26 ± 0.64	0.89 ± 0.014

Continued on next page

Table A.1 – continued from previous page

Depth of Cut (Level)	Laser Location (Level)	Tool Width (Level)	Cutting Speed (Level)	Laser Power (Level)	Cutting Force $\mu \pm \sigma$ (N)	Thrust Force $\mu \pm \sigma$ (N)	Surface Roughness $\mu \pm \sigma$ (μm)
3	0	0	1	1	29.48 ± 1.09	12.66 ± 0.88	0.91 ± 0.121
3	0	0	1	2	26.81 ± 2.53	12.38 ± 0.62	0.82 ± 0.159
3	0	1	0	0	40.52 ± 0.00	20.07 ± 0.00	0.69 ± 0.030
3	0	1	0	1	39.95 ± 0.85	20.86 ± 1.04	0.90 ± 0.059
3	0	1	0	2	42.26 ± 0.98	18.00 ± 0.69	0.83 ± 0.097
3	0	1	1	0	38.96 ± 0.45	19.74 ± 0.11	0.85 ± 0.077
3	0	1	1	1	40.37 ± 1.07	16.89 ± 0.16	1.07 ± 0.094
3	0	1	1	2	36.64 ± 0.00	16.75 ± 1.16	1.21 ± 0.278
3	1	0	0	0	28.06 ± 0.43	13.60 ± 0.18	0.80 ± 0.026
3	1	0	0	1	26.63 ± 0.53	11.71 ± 0.68	0.96 ± 0.120
3	1	0	0	2	25.17 ± 1.00	9.63 ± 0.76	0.75 ± 0.087
3	1	0	1	0	29.28 ± 0.37	14.26 ± 0.64	0.89 ± 0.014
3	1	0	1	1	28.77 ± 0.50	11.46 ± 0.37	1.03 ± 0.015

Continued on next page

Table A.1 – continued from previous page

Depth of Cut (Level)	Laser Location (Level)	Tool Width (Level)	Cutting Speed (Level)	Laser Power (Level)	Cutting Force $\mu \pm \sigma$ (N)	Thrust Force $\mu \pm \sigma$ (N)	Surface Roughness $\mu \pm \sigma$ (μm)
3	1	0	1	2	26.76 ± 2.38	10.46 ± 1.20	0.93 ± 0.021
3	1	1	0	0	40.52 ± 0.00	20.07 ± 0.00	0.69 ± 0.030
3	1	1	0	1	39.81 ± 0.85	20.27 ± 0.34	0.87 ± 0.103
3	1	1	0	2	41.16 ± 0.67	18.10 ± 0.29	0.91 ± 0.096
3	1	1	1	0	38.96 ± 0.45	19.74 ± 0.11	0.85 ± 0.077
3	1	1	1	1	41.42 ± 0.69	20.09 ± 0.85	0.83 ± 0.065
3	1	1	1	2	40.34 ± 0.87	18.77 ± 0.18	0.85 ± 0.099

Table A.2: Data used for force modeling and optimization

x_1	x_2	x_3	x_4	y_c	f_c	y_t	f_t	Measured DOC	Predicted DOC	T_1	T_2
10	10	0	100	12.08	10.90	6.80	6.75	7	7.49	41.89	25.00
10	10	5	100	12.73	9.98	5.07	6.15		7.84	200.50	868.84
10	10	10	100	14.13	8.68	4.10	5.32	10	8.13	379.50	1554.30
10	50	0	100	13.12	11.25	7.21	6.98		7.40	42.61	25.00
10	50	5	100	11.84	10.45	4.06	6.45		7.73	175.50	802.26
10	50	10	100	11.51	9.54	5.60	5.87		7.94	300.00	1302.10
15	10	0	100	17.34	15.27	9.14	8.99	10	11.59	41.09	25.00
15	10	5	100	16.76	14.04	8.51	8.24		12.11	200.00	847.36
15	10	10	100	17.33	12.10	6.90	7.08	14	12.51	379.00	1393.30
15	50	0	100	17.97	15.81	8.90	9.31		11.49	41.87	25.00
15	50	5	100	14.59	14.82	5.68	8.71		11.94	175.20	781.61
15	50	10	100	16.47	13.42	6.22	7.86		12.24	299.00	1167.50

Continued on next page

Table A.2 – continued from previous page

x_1	x_2	x_3	x_4	y_c	f_c	y_t	f_t	Measured DOC	Predicted DOC	T_1	T_2
20	10	0	100	23.68	19.84	13.75	11.40	12	15.79	40.68	25.00
20	10	5	100	22.08	18.19	11.00	10.43		16.33	199.86	815.05
20	10	10	100	22.52	15.73	10.60	9.00	19	16.84	378.68	1232.20
20	50	0	100	24.88	20.47	13.81	11.77		15.59	41.36	25.00
20	50	5	100	17.99	19.22	9.74	11.03		16.12	174.91	750.57
20	50	10	100	21.80	17.36	11.10	9.95		16.50	299.50	1032.90
25	10	0	100	28.06	24.34	13.60	13.79	18	19.89	40.42	25.00
25	10	5	100	27.00	22.20	12.22	12.56		20.59	198.00	782.00
25	10	10	100	26.00	19.37	12.29	10.95	22	21.15	377.00	1154.80
25	50	0	100	29.28	25.16	14.26	14.27		19.69	41.09	25.00
25	50	5	100	29.48	23.50	12.66	13.31		20.33	174.00	719.54
25	50	10	100	26.81	21.38	12.38	12.10		20.75	297.00	968.48
10	10	0	200	12.08	10.90	6.80	6.75		7.49	41.89	25.00
10	10	5	200	11.75	10.13	6.58	6.26		7.59	176.20	868.84

Continued on next page

Table A.2 – continued from previous page

x_1	x_2	x_3	x_4	y_c	f_c	y_t	f_t	Measured DOC	Predicted DOC	T_1	T_2
10	10	10	200	12.16	9.30	5.93	5.72		7.89	325.80	1554.30
10	50	0	200	13.12	11.25	7.21	6.98		7.39	42.61	25.00
10	50	5	200	12.93	10.67	5.82	6.61		7.49	152.50	802.26
10	50	10	200	11.51	10.03	5.60	6.19		7.69	254.30	1302.10
15	10	0	200	17.34	15.27	9.14	8.99		11.59	41.09	25.00
15	10	5	200	16.76	14.25	7.92	8.37		11.89	176.10	847.36
15	10	10	200	17.81	13.01	6.87	7.63		12.09	325.50	1393.30
15	50	0	200	17.97	15.81	8.90	9.31		11.49	41.87	25.00
15	50	5	200	17.23	15.03	7.47	8.84		11.69	152.40	781.61
15	50	10	200	19.64	14.21	8.13	8.35		11.89	254.20	1167.50
20	10	0	200	23.68	19.84	13.75	11.40		15.79	40.68	25.00
20	10	5	200	22.22	18.55	10.03	10.65		15.99	175.99	815.05
20	10	10	200	21.19	16.89	8.35	9.68		16.40	325.28	1232.20
20	50	0	200	24.88	20.47	13.81	11.77		15.59	41.36	25.00

Continued on next page

Table A.2 – continued from previous page

x_1	x_2	x_3	x_4	y_c	f_c	y_t	f_t	Measured DOC	Predicted DOC	T_1	T_2
20	50	5	200	22.96	19.48	9.74	11.18		15.89	152.20	750.57
20	50	10	200	21.80	18.29	8.74	10.49		16.09	254.00	1032.90
25	10	0	200	28.06	24.34	13.60	13.79		19.89	40.42	25.00
25	10	5	200	26.63	22.71	11.71	12.86		20.19	175.50	782.00
25	10	10	200	25.17	20.76	9.63	11.74		20.60	324.00	1154.80
25	50	0	200	29.28	25.16	14.26	14.27		19.69	41.09	25.00
25	50	5	200	28.77	24.02	11.46	13.61		19.99	151.80	719.54
25	50	10	200	26.76	22.54	10.46	12.76		20.29	253.00	968.48
25	10	35	100	12.76	12.79	7.29	7.21		22.39		
25	100	35	100	18.27	15.50	12.23	8.75		21.89		

Table A.3: Data used in thermal modeling

Laser Power (W))	Cutting Speed (mm/min)	Absorptivity	Temp. B.C. ℃
10	10	0.6	150
10	50	0.52	100
10	100	0.48	50
5	10	0.44	95
5	50	0.42	75
5	100	0.6	55

REFERENCES

[1] T. Masuzawa and H.K. Tonshoff. Three-dimensional micromachining by machine tools. *Annals of the CIRP*, 46(2):348–358, 1960.

[2] Microgear. http://www.lambdaphysik.com, 2004.

[3] Micromold. http://www.miniaturetool.com, 2004.

[4] U. Wallrabe, P. Ruther, T. Schaller, and W. K. Schomburg. Microsystems in medicine. *The International Journal of Artificial Organs*, 21(3):137–146, 1998.

[5] H. Tanaka, S. Shimada, N. Ikawa, and M. Yoshinaga. Wear mechanism of diamond cutting tool in machining of steel. *Key Engineering Materials*, 196: 69–78, 2001.

[6] J. Servin, T. Bauer, and C. Fallnich. Femtosecond lasers as novel tool in dental surgery. *Applied Surface Science*, 197:737–740, 2002.

[7] D. Gomez, I. Goenaga, I. Lizuain, and M. Ozaita. Femtosecond laser ablation for microfluidics. *Optical Engineering*, 44(5):1105–1113, 2005.

[8] W. König and A. K. Zaboklicki. Laser-assisted hot machining of ceramics and composite materials. *International Conference on Machining of Advanced Materials*, 847:455–463, 1999.

[9] F. E. Pfefferkorn, Y. C. Shin, and F. P. Incropera. Laser assisted machining of magnesia-partially-stabilized zirconia. *Journal of Manufacturing Science and Engineering*, 126:42–51, 2004.

[10] R. Singh and S. N. Melkote. Experimental characterization of laser assisted mechanical micromachining (lamm) process. *Proceedings of 2005 ASME International Mechanical Engineering Congress and Exposition, Orlando, FL*, 81350: 1–8, 2005.

[11] R. Singh and S. N. Melkote. Preliminary investigation of laser assisted mechanical micromachining. *Proceedings of the JSME/ASME International Conference on Materials and Processing, Seattle, WA*, 203:1–6, 2005.

[12] W. M. Steen. *Laser Materials Processing*. Springer-Verlag, London, 1998.

[13] G. Chryssolouris. *Laser Materials Processing*. Springer-Verlag, New York, 1991.

[14] B. Burg, E. Lamotte, L. Foulloy, and B. Zavidovique. A smart laser cutter. *Proceedings of the SPIE - High Power Lasers and Their Industrial Applications*, 650:209–217, 1985.

[15] G. Chryssolouris, J. Bredt, and S. Kordas. A new machine tool concept based on lasers. *Proceedings 14th NAMRC*, 14:244–251, 1986.

[16] G. Chryssolouris, J. Bredt, S. Kordas, and E. Wilson. Theoretical aspects of a laser machine tool. *Journal of Engineering for Industry*, 110(1):65–70, 1988.

[17] W. Dabby and U.-C. Paek. High-intensity laser-induced vaporization and explosion of solid material. *IEEE Journal of Quantum Electronics*, 8(2):106–111, 1972.

[18] D. C. Hamilton and I. R. Pashby. Hole drilling studies with a variable pulse length co2 laser. *Optics and Laser Technology*, pages 183–188, August 1979.

[19] U. C. Pack and F. P. Gagliano. Thermal analysis of laser drilling processes. *IEEE Journal of Quantum Electronics*, 8(2):112–119, 1972.

[20] M. Von Allmen. Laser drilling velocity in metals. *J. Applied Physics*, 47(12): 5460–5463, 1976.

[21] R. E. Wagner. Laser drilling mechanics. *J. Applied Physics*, 47(10):4631–4637, 1974.

[22] W. Shultz, G. Simon, H. M. Urbassek, and I. Decker. On laser fusion cutting of metals. *J. Phys. D: Applied Physics*, 20:481–488, 1987.

[23] K. A. Bunting and G. Cornfield. Toward a general theory of cutting: A relationship between the incident power density and cut speed. *Journal of Heat Transfer*, 97:116–122, 1975.

[24] M. F. Modest and H. Abakians. Evaporative cutting of a semi-infinite body with a moving cw laser. *Journal of Heat Transfer*, 108:602–607, 1986.

[25] G. Chryssolouris and W. C. Choi. Theoretical aspects of laser grooving. *Proceedings of 14th Conference on Production Research and Technology*, pages 323–331, 1987.

[26] G. Chryssolouris, W. C. Choi, S. B. Kyi, and P. Sheng. Investigation of the effects of a gas jet on laser grooving. *Proceedings of the XVI NAMRC*, 16: 217–222, 1987.

[27] G. Comini, S. D. Guidice, R.W. Lewis, and O.C. Zienkiewics. Finite element solution of non-linear heat conduction problems with special reference to phase change. *International Journal of Numerical Methods in Engineering*, 8:613–624, 1974.

[28] Decker, J. Rue, and V. Atzert. Physical models and technological aspects of laser gas cutting. *Proceedings of SPIE*, 455:81–88, 1983.

[29] W. Zhang, Y. Lawrence Yao, and I. C. Noyan. Microscale laser shock peeing of thin films, part 1: Experiment, modeling and simulation. *Journal of Manufacturing Science and Engineering*, 126(1):10–17, 2004.

[30] W. Cheng, Y. Zhang, Lawrence Yao, and I. C. Noyan. Microscale laser shock peeing of thin films, part 2: High spatial resolution material characterization. *Journal of Manufacturing Science and Engineering*, 126(1):18–24, 2004.

[31] M. C. Gower. Excimer laser micromachining: A 15 year perspective. *Laser Applications in Microelectronic and Optoelectronic Manufacturing IV, SPIE*, 3618:251–261, 1999.

[32] J. Zhang, K. Sugioka, and K. Midorikawa. Laser-induced plasma-assisted ablation of fused quartz using the fourth harmonic of a nd+:yag laser. *Applied Physics A*, 67:545–549, 1998.

[33] J. Zhang, K. Sugioka, and K. Midorikawa. High-speed machining of glass materials by laser-induced plasma-assisted ablation using a 532-nm laser. *Applied Physics A*, 67:499–501, 1998.

[34] J. Zhang, K. Sugioka, and K. Midorikawa. Study of micro-processing of glass materials by laser-induced plasma-assisted ablation. *Laser Applications in Microelectronic and Optoelectronic manufacturing V, SPIE*, 3933:332–337, 2000.

[35] Klocke and Zaboklicki. Laser-assisted turning of ceramics. *Machining of Ceramics and Composites*, pages 551–574, 1999.

[36] S. Lei and Y. C. Shin. Experimental investigation of thermo-mechanical characteristics in laser-assisted machining of silicon nitride ceramics. *Journal of Manufacturing Science and Engineering*, 123:639–646, 2001.

[37] J. C. Rozzi, F. E. Pfefferkorn, and Y. C. Shin. Experimental evaluation of the laser assisted machining of silicon nitride ceramics. *Journal of Manufacturing Science and Engineering*, 123:639–646, 2001.

[38] S. Lei, Y. C. Shin, , and F. P. Incropera. Deformation mechanisms and constitutive modeling for silicon nitride undergoing laser-assisted machining. *International Journal of Machine Tools and Manufacture*, 40:2213–2233, 2000.

[39] Y. Tian and Y. C. Shin. Multiscale finite element modeling of silicon nitride ceramics undergoing laser-assisted machining. *ASME Journal of Manufacturing Science and Engineering*, 127:287–295, 2007.

[40] P. A. Rebro, Y. C. Shin, and F. P. Incropera. Laser-assisted machining of reaction sintered mullite ceramics. *Journal of Manufacturing Science and Engineering*, 124:875–885, 2002.

[41] J. C. Rozzi, F. P. Incropera, and Y. C. Shin. Transient, 3-d heat transfer model for the laser assisted machining of silicon nitride: I. comparison of predictions with measured surface temperature histories. *International Journal of Heat and Mass Transfer*, 43:389–396, 2000.

[42] J. C. Rozzi, F. P. Incropera, and Y. C. Shin. Transient, 3-d heat transfer model for the laser assisted machining of silicon nitride: Assessment of parametric effects. *International Journal of Heat and Mass Transfer*, 43:1425–1437, 2000.

[43] L. N. López de Lacalle, J. A. Sanchez, A. Lamikiz, and A. Celaya. Plasma assisted milling of heat-resistant superalloys. *Journal of Manufacturing Science and Engineering*, 126:274–285, 2004.

[44] A. Kaldos and H. J. Pieper. Laser machining in die making - a modern rapid tooling process. *Journal of Materials Processing Technology*, 155-156:1815–1820, 2004.

[45] S. Skvarenina and Y. C. Shin. Laser assisted machining of compacted graphite iron. *International Journal of Machine tools and Manufacture*, 46(1):7–17, 2006.

[46] M. Anderson, R. Patwa, and Y. C. Shin. Laser assisted machining of inconel 718 with an economic analysis. *International Journal of Machine tools and Manufacture*, 46(14):1879–1891, 2006.

[47] P. Dumitrescu, P.Koshy, J. Stenekes, and Elbestawi. High-power diode laser assisted hard turning of aisi d2 tool steel. *International Journal of Machine tools and Manufacture*, 46(15):2009–2016, 2006.

[48] M. C. Gower. Industrial applications of pulsed lasers to materials processing. *High Power Laser Ablation, SPIE*, 3343(1):171–182, 1998.

[49] N. Rizvi, D. Milne, P. Rumsby, and M. C. Gower. Laser micromachining-new developments and applications. *Laser Applications in Microelectronic and Optoelectronic manufacturing V, SPIE*, 3933:261–271, 2000.

[50] C. J. Hayden, J. C. T. Eijkel, and C. Dalton. An alternative method of fabricating sub-micron resolution masks using excimer laser ablation. *J. Micromech. Microeng.*, 14:826–831, 2004.

[51] D. Hellrung, Li-YaYeh, F. Depiereux, A. Gillner, and R. Poprawe. High- accuracy micromachining of ceramics by frequency-tripled nd:yag- lasers. *Laser Applications in Microelectronic and Optoelectronic manufacturing IV, SPIE*, 3618:348–356, 1999.

[52] H. Yang and C-T. Pan. Excimer laser-induced formation of metallic microstructures by electroless copper plating. *J. Micromech. Microeng.*, 12:157–161, 2002.

[53] H. Exner, B. Keiper, and P. Meja. Microstructuring of materials by pulsed laser focusing and projection technique. *Laser Applications in Microelectronic and Optoelectronic Manufacturing IV, SPIE*, 3618:340–347, 1999.

[54] W. Pfleging, W. Bernauer, T. Hanemann, and M. Torge. Rapid fabrication of microcomponents - uv-laser assisted prototyping, laser micro-machining of mold inserts and replication via photomolding. *Microsystem Technologies*, 9: 67–74, 2002.

[55] W. Pfleging, W. Bernauer, T. Hanemann, and M. Torge. Laser micromachining of mold inserts for replication techniques- state of art and applications. *Laser Applications in Microelectronic and Optoelectronic Manufacturing VI, SPIE*, 4274:331–345, 2001.

[56] S. M. Metev and V. P. Veiko. *Laser Assisted Microtechnology, pages 76-79.* Springer-Verlag, Germany, 1998.

[57] P. Stanley, K. Venkatakrishnan, and L. Lim. Influence of femtosecond laser parameters on the fabrication of photomask by direct ablation. *Lasers Eng.*, 131:13–23, 2003.

[58] R. Fedosejevs, M. Argument, A. Sardarli, S. E. Kirkwood, R. Holenstein, and Y. Y. Tsui. Laser micromachining for microfluidic, microelectronic and mems applications. *Proc. Int. Conf. on Laser MEMS, NANO and Smart Systems, July 20-23, Banff, Alberta, Canada*, pages 53–56, 2003.

[59] P. R. Herman, K. P. Chen, P. Corkum, A. Naumov, S. Ngi, and J. Zhang. Advanced lasers for photonic device microfabrication. *RIKEN Rev.*, 32:31–35, 2001.

[60] C. Momma, U. Knop, and S. Nolte. Laser cutting of slotted tube coronary stents - state-of-the-art and future developments. *Progr. Biomed. Res.*, 41: 39–44, 1999.

[61] V. Hertel. Surface and bulk ultrashort pulsed laser processing of transparent materials. *Proc. SPIE*, 4088:17–24, 2000.

[62] M.R. Kasaai, V. Kacham, F. Théberge, and S.L. Chin. The interaction of femtosecond and nanosecond laser pulses with the surface of glass. *J. Non-Cryst. Solids*, 319:129–135, 2003.

[63] F. Théberge and S.L. Chin. Enhanced ablation of silica by the superposition of femtosecond and nanosecond laser pulses. *Appl. Phys. A*, 80:1505–1510, 2005.

[64] G. Dumitru, V. Romano, H. P. Weber, M. Sentis, J. Hermann, S. Bruneau, W. Marine, H. Haefke, and Y. Gerbig. Metallographical analysis of steel and hard metal substrates after deep-drilling with femtosecond laser pulses. *Applied Surface Science*, 208:181–188, 2003.

[65] G. Dumitru, B. Luscher, M. Krack, S. Bruneau, J. Hermann, and Y. Gerbig. Laser processing of hardmetals: Physical basics and applications. *International Journal of Refractory Metals and Hard Materials*, 23(4-6):278–286, 2005.

[66] M. Henry, P. M. Harrison, I. Henderson, and M. F. Brownell. Laser milling: a practical industrial solution for machining a wide variety of materials. *Proceedings of the SPIE - The International Society for Optical Engineering*, 5662(1): 627–632, 2004.

[67] X. Liu, M. B.G. Jun, R. E. Devor, and S. G. Kapoor. Cutting mechanisms and their influence on dynamic forces, vibrations and stability in micro end milling. *Proceedings of ASME IMECE, Anaheim, CA*, 62416:1–10, 2004.

[68] C. R. Friedrich and M. J. Vasile. Development of the micromilling process for high-aspect-ratio microstructures. *Journal of Microelectromechanical Systems*, 5(1):33–38, 1996.

[69] C. Friedrich, P. Coane, J. Goettert, and N. Gopinathin. Direct fabrication of deep x-ray lithography masks by micromechanical milling. *Precision Engineering*, 22:164–173, 1998.

[70] Th. Schaller, M. Heckele, and R. Ruprecht. Mechanical micromachining for mold insert fabrication and replication. *American Society of Precision Engineering, Spring Topical Meeting*, pages 3–8, 1999.

[71] Th. Schaller, L. Bohn, J. Mayer, and K. Schubert. Microstructure grooves with a width of less than 50 μm cut with ground hard metal micro end mills. *Precision Engineering*, 23:229–235, 1999.

[72] D. P. Adams, M. J. Vasile, G. Benavides, and A. N. Campbell. Micromilling of metal alloys with focused ion beam-fabricated tools. *Precision Engineering*, 25:107–113, 2001.

[73] M. Takacsa, B. Vero, and I. Meszaros. Micromilling of metallic materials. *Journal of Materials Processing Technology*, 138:152–155, 2003.

[74] M. Rahman, A. Senthil Kumar, and J. R. S. Prakash. Micromilling of pure copper. *Journal of Materials Processing Technology*, 116:39–43, 2001.

[75] Y. Huang and S. Y. Liang. Force modeling in shallow cuts with large negative rake angle and large nose radius tools - application to hard turning. *International Journal of Advanced Manufacturing Technology*, 22(9-10):626–632, 2003.

[76] M. P. Volger, R. E. DeVor, and S. G. Kapoor. Microstructure-level force prediction model for micromilling of multi-phase materials. *Journal of Manufacturing Science and Engineering*, 125:202–209, 2003.

[77] S. Joshi and S. N. Melkote. An explanation for the size-effect in machining using strain gradient plasticity. *Trans. of the ASME, J. of Manufacturing Sci. and Engineering*, 126(4):679–684, 2004.

[78] K. Liu and S. N. Melkote. Material strengthening mechanisms and their contribution to size effect in micro-cutting. *Journal of Manufacturing Science and Engineering*, 128:730–738, 2006.

[79] D. Cox, G. Newby, H.W. Park, and S.Y. Liang. Performance evaluation of a miniaturized machining center for precision manufacturing. *Proceedings of IMECE, Anaheim, CA, USA*, pages 1–6, 2004.

[80] R. N. Roth and P. L. B. Oxley. Slip-line field analysis for orthogonal machining based upon experimental flow fields. *Journal of Mech. Engr. Science*, 14(2): 85–97, 1972.

[81] N. Fang, I. S. Jawahir, and P. L. B. Oxley. Universal slip-line model with non-unique solutions for machining with curled chip formation and a restricted contact tool. *International Journal of Mechanical Sciences*, 43(2):557–580, 2001.

[82] D. J. Waldorf, R. E. DeVor, and S. G. Kapoor. An evaluation of ploughing models for orthogonal machining. *Journal of Manufacturing Science and Engineering*, 121:550–558, 1999.

[83] S. Venkatachalam and S. Y. Liang. Effects of ploughing forces and friction coefficient in microscale machining. *Journal of Manufacturing Science and Engineering*, 129:274–280, 2007.

[84] D. Haslam and C. Rubenstein. Surface and sub-surface work-hardening produced by the planing operation. *Annals of the CIRP*, 18:369–381, 1970.

[85] C. Rubenstein, W. S. Lau, and P. K. Venuvinod. Flow of workpiece material in the vicinity of the cutting edge. *International Journal MTDR*, 25(1):91–97, 1985.

[86] J. C. Jaeger. Moving sources of heat and temperature at sliding contacts. *Proc. of Royal Soc. Of N.S.W*, 76:203–224, 1942.

[87] C. L. Tsai and C. A. Hou. Theoretical analysis of weld pool behavior in the pulsed current gtaw processs. *Journal of Heat Transfer*, 110:160–165, 1988.

[88] A. Kar and J. Mazumder. Three-dimensional transient thermal analysis for laser chemical vapor deposition on uniformly moving finite slabs. *J. Appl. Physics*, 65:2923–2933, 1989.

[89] Manca, B. Morrone, and V. Naso. Quasi-steady-state three-dimensional temperature distribution induced by a moving circular gaussian heat source in a finite depth solid. *International Journal of Heat and Mass Transfer*, 38(7): 1305–1315, 1995.

[90] Z.B. Hou and R. Komanduri. General solutions for stationary/moving plane heat source problems in manufacturing and tribology. *International Journal of Heat and Mass Transfer*, 43:1679–1698, 2000.

[91] R. Komanduri and Z.B. Hou. Thermal analysis of laser surface transformation hardening - optimization of process parameters. *International Journal of Machine Tools and Manufacture*, 44:991–1008, 2004.

[92] D. Y. Tzou. *Macro- to Microscale Heat Transfer: The Lagging Behavior*. Taylor and Francis, Washington DC, 2007.

[93] M. N. Ozisik and D. Y. Tzou. On the wave theory in heat-conduction. *Journal of Heat Transfer, Transactions of the ASME*, 116(3):526–535, 1994.

[94] R. Singh and S. N. Melkote. Experimental of laser assisted mechanical micromachining. *International Journal of Machine Tool and Manufacture*, 47: 1139–1150, 2007.

[95] Y. Jeon and F. Pfefferkorn. Effect of laser preheating the workpiece on micro-end milling of metals. *Proceedings of IMECE, Orlando, Florida, USA*, pages 1–10, 2005.

[96] Hiroshi, J. Suzuki, H. Kawakami, and E. Hiroshi. Selection of parameters on laser cutting of mild steel plates taking account of some manufacturing purposes. *Proceedings of the SPIE*, 5603:418–425, 2005.

[97] E. Kennedy, G. Byrne, and D.N. Collins. A review of the use of high power diode lasers in surface hardening. *Journal of Materials Processing Technology*, 155-156:1855–1860, 2004.

[98] Y. S. Touloukian and E. H. Buyco. *Macro- to Microscale Heat Transfer: The Lagging Behavior*. Taylor and Francis, Washington DC, 2007.

[99] F. Cverna. *ASM Ready Reference Thermal Properties of Metals*. ASM, Ohio, 2005.

[100] S. Brown and H. Song. Finite element simulation of welding of large structures. *Journal of Engineering for Industry*, 114(11):441–451, 1992.

[101] M. R. Frewin and D. A. Scott. Finite element model of pulsed laser welding. *Welding Journal*, 78(1):15S–22S, 1999.

[102] W. Gogol and B. Staniszewski. Thermophysical properties research in poland. *Proceedings of the Symposium on Thermophysical Properties, Gaithersburg, MD, USA*, pages 55–56, 1977.

[103] S. Kou, D. K. Sun, and Y. P. Le. A fundamental study of laser transformation hardening. *Metallurgical Transactions A*, 14:643–653, 1983.

[104] Sainte-Catherine, M. Jeandin, D. Kechemair, J. P. Ricaud, and L. Sabatier. Study of dynamic absorptivity at 10.6 μm (co_2) and 1.06 μm (nd-yag) wavelengths as a function of temperature. *Journal de Physique IV (Colloque)*, C7: 151–157, 1991.

[105] J. Manjunathaiah and W. J. Endres. A new model and analysis of orthogonal machining with an edge-radiused tool. *Journal of Manufacturing Science and Engineering*, 122:384–390, 2000.

[106] N. Fang and Q. Wuu. A new methodology for modeling material constitutive behavior using an orthogonal machining test. *Transactions of NAMRI/SME XXXII*, pages 95–102, 2004.

[107] H. Adibi-Sadeh, V. Madhavan, and Behnam Bahr. Extension of oxley's analysis of machining to use johnson-cook material model. *Proceedings of ASME IMECE, New York, NY, USA*, 23320:1–10, 2001.

[108] J. M. Challen and P. L. B. Oxley. Slip-line fields for explaining the mechanics of polishing and related processes. *International Journal of Mechanical Sciences*, 26(6-8):403–418, 1984.

[109] D. J. Waldorf, R. E. DeVor, and S. Kapoor. A slip-line field for ploughing during orthogonal cutting. *Journal of Manufacturing Science and Engineering-Transactions of the ASME*, 120(4):693–699, 1998.

[110] P. K. Basuray, B. K. Misra, and G. K. Lal. Transition from ploughing to cutting during machining with blunt tools. *Wear*, 43:341–349, 1977.

[111] R. Komanduri. Some aspects of machining with negative rake angle tools simulating grinding. *Int. J. Mach. Tool Des. Res.*, 11:223–233, 1971.

[112] V. R. Joseph and S. N. Melkote. Statistical adjustments to engineering models. *submitted to Technometrics*, 2007.

[113] R. Singh, M. J. Alberts, and S. N. Melkote. Characterization and prediction of the heat affected zone in a laser-assisted mechanical micromachining (lamm) process. *submitted to International Journal of Machine Tool and Manufacturing*, 2007.

[114] H. Yan, J. Hua, and R. Shivpuri. Flow stress of aisi h13 die steel in hard machining. *Materials and Design*, 28:272–277, 2007.

[115] J. Sacks J, S. B. Schiller, and W. J. Welch. Designs for computer experiments. *Technometrics*, 31(1):41–47, 1989.